ADVANCED MATERIALS
www.advmat.de

Advanced Air Electrodes for Reversible Protonic Ceramic Electrochemical Cells: A Comprehensive Review

Xi Chen, Yeshu Tan, Zheng Li, Tong Liu, Yinghao Song, Shuo Zhai, Na Yu, Zongping Shao, and Meng Ni**

Reversible protonic ceramic electrochemical cells (R-PCECs) have great potential for efficient and clean power generation, energy storage, and sustainable synthesis of high-value chemicals. However, the sluggish and unstable kinetics of the oxygen reduction reaction (ORR) and oxygen evolution reaction (OER) in the air electrode hinder the R-PCEC development. Durable $H^+/e^-/O^{2-}$ triple-conducting air electrode materials are promising for enhancing reaction kinetics and improving catalytical stability. This review synthesizes the recent progress in triple-conducting air electrodes, focusing on their working mechanisms, including electrode kinetics, lattice and its defect structure in oxides, and the generation and transport processes of H^+, O^{2-}, and e^-. It also examines the required physicochemical properties and their influencing factors. By synthesizing and critically analyzing the latest theoretical frameworks, advanced materials, and regulation strategies, this review outlines the challenges and prospects shaping the future of R-PCEC technology and air electrode development. Based on these theories and multiple strategies about the bulk triple conducting properties and surface chemical states, this review provides practical guidance for the rational design and development of efficient and stable air electrode materials for R-PCECs and related electrocatalytic materials.

1. Introduction

Heavily relying on fossil fuels as the major energy source causes energy crises, global warming, and environmental pollution.[1,2] To address these challenges, governments worldwide have implemented a series of strategies and interventions.[3] It is increasingly evident that reducing dependence on fossil fuels and limiting carbon dioxide emissions are imperative for advancing sustainable development and achieving carbon neutrality.[4]

Therefore, it is critical to reduce the reliance on fossil fuels and use more renewable energy resources. However, renewable energies such as wind and solar power are fluctuating and intermittent, requiring effective energy storage. Although rechargeable batteries are promising for small-scale energy storage, they are not suitable for large-scale and long-duration energy storage. For comparison, reversible solid oxide cells (R-SOCs) technology can be a promising alternative for large-scale and long-duration energy storage. R-SOC can work as a solid oxide electrolysis cell (SOEC) to use excess renewable power for hydrogen (H_2) production, which can be converted back to electricity when needed using a solid oxide fuel cell (SOFC). R-SOCs have the merits of low material costs, high electrochemical performance, exceptional conversion efficiency, and environmental friendliness.[5] However, the conventional oxygen-ion conducting R-SOCs (R-SOFCs)[6] need to operate at high temperatures (700-900 °C) to enable fast oxygen-ion conduction, which causes degradation and increases maintenance costs. Moreover, high operating temperature also increases thermal management requirements and slows down the startup/shutdown processes. These challenges limit its reliable large-scale and long-term applications. Reversible protonic electrochemical cells (R-PCECs)[7] instead of R-SOCs are more promising due to the low activation energy required for proton conduction compared to oxygen-ion conduction in the electrolyte,[8] ensuring the sufficient ion conduction at reduced working temperatures. Additionally, R-PCECs utilize and produce pure and dry hydrogen directly, which enhances fuel utilization and enables electrochemical compression of hydrogen directly within the cell (without being diluted by vapor), thus reducing system complexity and operational costs.

X. Chen, Y. Tan, Z. Li, T. Liu, Y. Song, S. Zhai, N. Yu, M. Ni
Department of Building and Real Estate
Research Institute for Sustainable Urban Development (RISUD) and Research Institute for Smart Energy (RISE)
The Hong Kong Polytechnic University
Hung Hom, Kowloon, Hong Kong 999077, China
E-mail: naaaa.yu@connect.polyu.hk; meng.ni@polyu.edu.hk
Z. Shao
WA School of Mines: Minerals Energy and Chemical Engineering (WASM-MECE)
Curtin University
Perth, WA 6845, Australia

The ORCID identification number(s) for the author(s) of this article can be found under https://doi.org/10.1002/adma.202418620

DOI: 10.1002/adma.202418620

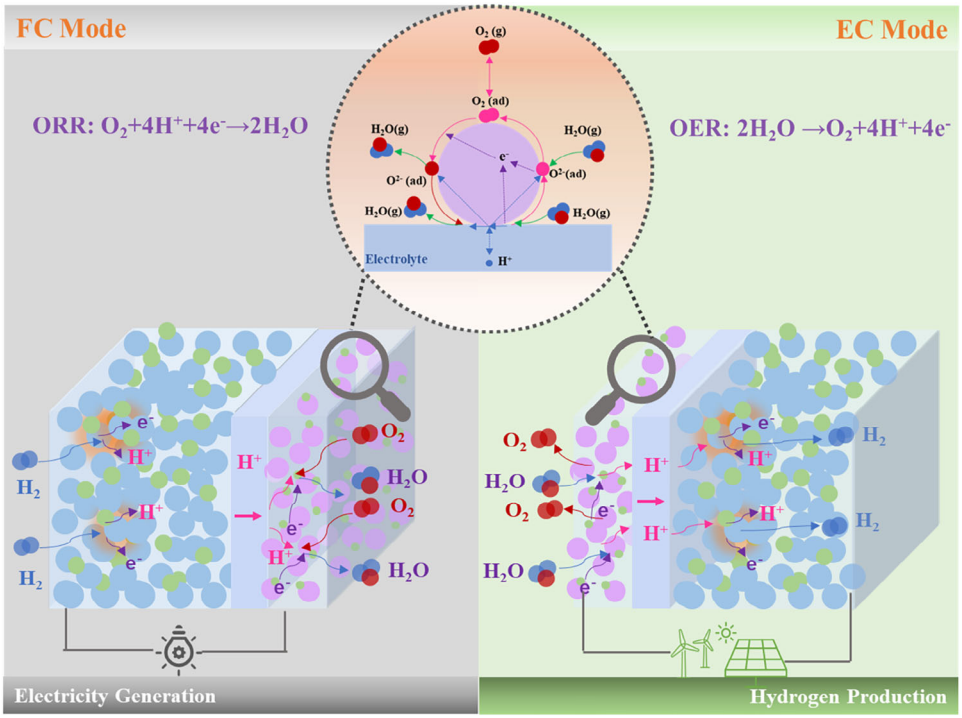

Figure 1. Schematic diagram of R-PCEC in fuel cell and electrolysis operation modes.

Furthermore, they allow the synthesis of various chemicals such as ammonia, carbon monoxide, methane, low-carbon olefins, and aromatics through its electrolysis mode (protonic ceramic electrolysis cell, PCEC).[9] This paves an attractive pathway for large-scale chemical energy storage, enabling the stored chemical energy to be converted into electricity efficiently at any time, thus facilitating efficient energy conversion among different sources.

Unfortunately, the R-PCECs technology still encounters several challenges. A big concern is the reduced kinetics of oxygen reduction reaction (ORR) and oxygen evolution reaction (OER) on the air electrode at reduced operating temperatures. To address this issue, various modification strategies have been developed to enhance the catalytic activity and stability of air electrodes. These strategies include modifications of bulk triple-conducting properties, surface chemical states, phase compositions, and microstructures, supported by experimental evidence and theoretical calculations.

To elucidate the current challenges and progress of air electrodes, this review provides a comprehensive summary of recent studies and offers valuable insights to guide the rational design of high-performance, stable air electrodes for R-PCECs. The review begins by explaining the operational principles of R-PCECs in both electrolysis and fuel cell modes, with a focus on the ORR and OER processes occurring at the air electrode. It then presents a detailed exploration of the conduction mechanisms of $H^+/O^{2-}/e^-$ in perovskite oxides, followed by an in-depth discussion of the fundamental factors that influence the physicochemical properties of air electrode materials. Moreover, this review provides a thorough analysis of various air electrode materials and structures reported in the literature, along with a detailed evaluation of modification strategies for improving catalytic activity, durability, and interfacial properties. The current state of air electrode development for practical applications is discussed, including their actual catalytic and electrochemical performance. The key challenges and promising research directions for future developments are discussed.

2. Working Mechanism and Challenge of R-PCECs

2.1. R-PCECs' Working Mechanism

R-PCECs can flexibly switch between two operational modes for reversible operation. Specifically, in fuel cell (FC) mode, the device efficiently converts the chemical energy of the fuel into electricity. Taking hydrogen (H_2) as an example, it undergoes the hydrogen oxidation reaction (HOR) at the fuel electrode to produce protons (H^+), which are transported through the electrolyte membrane to reach the air electrode for ORR, generating water as the final product (**Figure 1**). In electrolysis cell (EC) mode, the device can utilize electrical energy to produce high-quality chemicals. For instance, for H_2O electrolysis, H_2O is converted into oxygen and protons at the air electrode via OER. Then the generated protons pass through the electrolyte membrane to the fuel electrode side, where they undergo the hydrogen evolution reaction (HER) to produce dry and pure H_2. The detailed reactions are shown in Equations (1–3).

$$\text{Fuel electrode (HOR/HER)}: H_2\,(g) \rightleftharpoons 2H^+ + e^- \quad (1)$$

$$\text{Air electrode (ORR/OER)}: \frac{1}{2}O_2\,(g) + 2H^+ + 2e^- \rightleftharpoons H_2O\,(g) \quad (2)$$

$$\text{Overall}: H_2\,(g) + \frac{1}{2}O_2\,(g) \rightleftharpoons H_2O\,(g) \quad (3)$$

In general, R-PCECs are composed of three key components arranged in a sandwich-like structure: a dense electrolyte between a porous fuel electrode and an air electrode. Each component plays a vital role in cell operation.

The main function of the electrolyte layer is to transport protons while preventing direct contact between fuel and air, requiring high proton conductivity and pore-free structure. It must also have minimal electronic conductivity to avoid current leakage and improve efficiency.

The fuel electrode is responsible for fuel oxidation/reduction, requiring excellent electrochemical catalytic activity, electronic conductivity, proton generation/transport, and gas diffusion capabilities. It also needs mechanical strength, as it supports the entire cell.

Like the fuel electrode, the air electrode also requires a porous structure and excellent electronic conductivity to facilitate the oxygen mass transport and electron migration. However, the air electrode undergoes ORR/OER, good bifunctional catalytic activity for ORR/OER is essential to achieve high performance.[10] Additionally, the stability between components is also important, including the comparable thermal expansion coefficients to avoid large thermal stress at the interface, avoiding adverse thermal chemical and electrochemical reactions between components (e.g., phase separation, cation diffusion), and ensuring sufficient mechanical strength of the assembled cells.

2.2. One Challenge of R-PCECs—Air Electrode

The sluggish ORR/OER kinetics observed at reduced operating temperatures predominantly stem from the higher activation energy barrier associated with oxygen ion transport compared to proton conduction pathways.[8] Additionally, some air electrode materials, which predominantly function as mixed oxygen ion and electron (O^{2-}/e^-) conductors, have exhibited unsatisfactory electrochemical performance. This limitation is largely attributed to the restricted active reaction sites, confined primarily to the electrolyte-electrode interface. To expand the triple-phase boundaries (TPBs) for ORR/OER at the air electrode, the development of proton-conducting materials combined with O^{2-}/e^- conductivity — referred to as triple-conducting oxides (TCOs) — holds considerable potential. It has been a focus for researchers over the past five years. Furthermore, the air electrode must maintain excellent stability in high-steam environments without forming inactive phases during the reversible switching modes. This requires a balance between adequate water uptake for proton generation and resistance to water vapor. Another challenge is the thermal expansion coefficient (TEC) mismatch between the air electrode and electrolyte, which causes cracks at the interface or even delamination of air electrode from the electrolyte, decreasing the cell performance or even causing cell failure. These issues in air electrode performance significantly limit the overall electrochemical performance of R-PCEC technology. Therefore, the development of a durable, high-performance triple-conducting air electrode with enhanced activity and stability is essential to accelerate the commercialization of R-PCECs.

2.2.1. Reactions Mechanism

The rational design of high-performance air electrodes necessitates a fundamental understanding of ORR/OER mechanisms. Here, the specific different ORR pathways in mixed O^{2-}/e^- conductors (MIEC) and triple oxygen ion–proton–electron ($O^{2-}/H^+/e^-$) conductors (TIEC) are summarized[11] (**Figure 2**), and the following detailed elementary sub-steps are displayed in Equations (4–18).

Initial steps:

$$O_2\,(g) \rightarrow O_{2,ad}\,(\text{surface}) \quad (4)$$

$$O_{2,ad}\,(\text{surface}) \rightarrow 2O_{ad}\,(\text{surface}) \quad (5)$$

Surface path (MIEC):

$$O_{ad}\,(\text{surface}) + e^- \rightarrow {O_{ad}}^-\,(\text{surface}) \quad (6)$$

$$\left\{{O_{ad}}^-\,(\text{surface}) \rightarrow {O_{ad}}^-\,(\text{TPB}),\ {O_{ad}}^-\,(\text{TPB}) + e^- \rightarrow O^{2-}\,(\text{TPB})\right\} \quad (7)$$

$$\left\{{O_{ad}}^-\,(\text{surface}) + e^- \rightarrow {O_{ad}}^{2-}\,(\text{surface}),\ {O_{ad}}^{2-}\,(\text{surface}) \rightarrow O^{2-}\,(\text{TPB})\right\} \quad (8)$$

Bulk path (MIEC):

$$O_{ad}\,(\text{surface}) + e^- \rightarrow {O_{ad}}^-\,(\text{bulk}) \quad (9)$$

$${O_{ad}}^-\,(\text{bulk}) + e^- \rightarrow {O_{ad}}^{2-}\,(\text{bulk}) \quad (10)$$

$${O_{ad}}^{2-}\,(\text{bulk}) \rightarrow O^{2-}\,(\text{TPB}) \quad (11)$$

TPB (MIEC):

$$H^+\,(\text{TPB}) + O^{2-}\,(\text{TPB}) \rightarrow OH^-\,(\text{TPB}) \quad (12)$$

Surface path-TPB (TIEC):

$$O_{ad}\,(\text{surface}) + e^- \rightarrow {O_{ad}}^-\,(\text{surface}) \quad (6)$$

$$\{{O_{ad}}^-\,(\text{surface}) \rightarrow {O_{ad}}^-\,(\text{TPB}),\ {O_{ad}}^-\,(\text{TPB}) + e^- \rightarrow O^{2-}\,(\text{TPB}),\ O^{2-}\,(\text{TPB}) + H^+\,(\text{surface}) \rightarrow OH^-\,(\text{TPB})\} \quad (13)$$

$$\left\{{O_{ad}}^-\,(\text{surface}) + e^- \rightarrow {O_{ad}}^{2-}\,(\text{surface}),\ H^+\,(\text{surface}) \rightarrow H^+\,(\text{TPB}), {O_{ad}}^{2-}\,(\text{surface}) + H^+\,(\text{TPB}) \rightarrow OH^-\,(\text{TPB})\right\} \quad (14)$$

Bulk path-TPB (TIEC):

$$O_{ad}\,(\text{surface}) + e^- \rightarrow {O_{ad}}^-\,(\text{bulk}) \quad (9)$$

$${O_{ad}}^-\,(\text{bulk}) + e^- \rightarrow {O_{ad}}^{2-}\,(\text{bulk}) \quad (10)$$

$$H^+\,(\text{interface}) \rightarrow H^+\,(\text{bulk, TPB}) \quad (15)$$

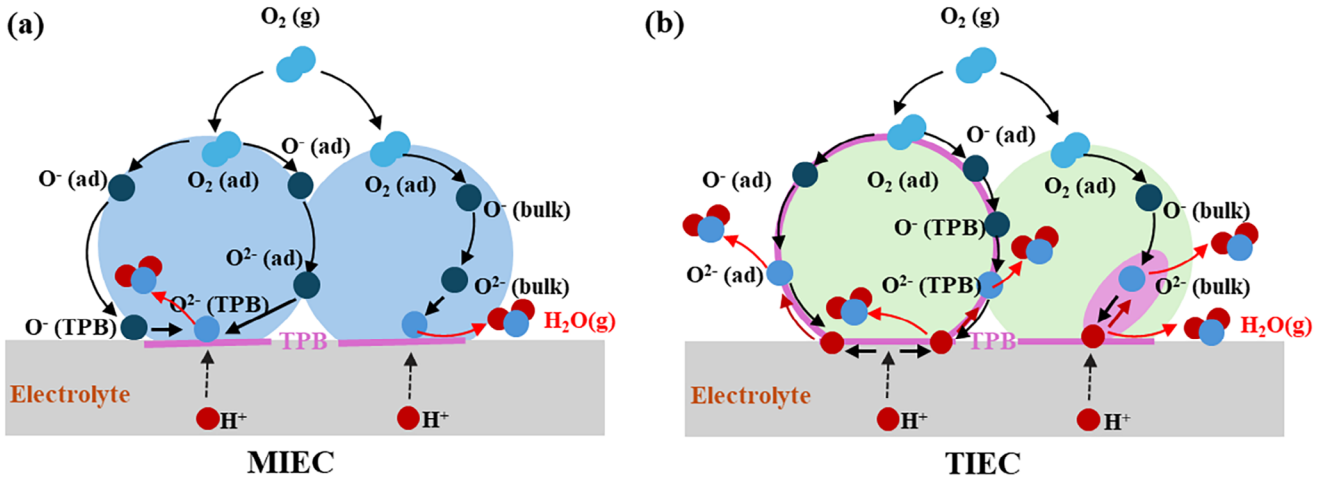

Figure 2. Detailed elementary ORR steps for a) MIEC and b) TIEC applied as R-PCEC's air electrodes.

$$O_{ad}^{2-}\,(\text{bulk}) + H^{+}\,(\text{bulk, TPB}) \rightarrow OH^{-}\,(\text{TPB}) \quad (16)$$

Final steps:

$$H^{+}\,(\text{TPB}) + OH^{-}\,(\text{TPB}) \rightarrow H_2O\,(\text{TPB}) \quad (17)$$

$$H_2O\,(\text{TPB}) \rightarrow H_2O\,(g) \quad (18)$$

For MIEC-type air electrodes, the ORR processes primarily encompass oxygen adsorption and dissociation (Equations (4,5)), the subsequent generation and diffusion of active oxygen ions (Equations (6–11)), and the concurrent generation of water at the TPBs coupled with surface dissociation (Equations (12,17, and 18)). Similarly, the OER processes are the reverse of these elementary sub-steps. These active oxygen ions, once generated, can transport to the active reaction site via both surface (Equations (6–8)) and bulk (Equations (9–11)) pathways. As illustrated in Figure 2a, the TPB of the electrode reaction is confined to the interface between the air electrode and the electrolyte. For comparison, TIEC-type air electrodes introduce additional complexity to the electrochemical reaction due to their augmented proton transport capacity (Figure 2b). Specifically, the active oxygen ions produced in TIEC-type electrodes can take part in electrode reactions with protons, leading to the direct generation of water either at the electrode surface or within the bulk phase. The TPB of TIEC-type air electrodes is expanded to the entire surface of the catalyst, thereby significantly enhancing electrode ORR/OER kinetics. Accordingly, it is imperative to integrate proton conductivity into R-PCEC air electrodes in accordance with the elucidated reaction mechanism.[12]

2.2.2. Proton Conduction Mechanism

As previously mentioned, the proton conductivity exhibited by TIEC air electrodes is pivotal in attaining elevated catalytic activity for ORR/OER. Hence, a thorough comprehension of the proton conduction mechanism is imperative for the rational design of optimal air electrodes for R-PCECs. Fundamentally, protons are incapable of occupying discrete sites within the crystal structure of perovskite oxides; instead, they tend to form bonds with other anions, primarily in the form of hydroxide defects ($OH_O^{\cdot}$).[13] Moreover, high proton conductivity requires consideration of both the generation and migration of these hydroxide defects.

To date, three possible mechanisms for proton uptake in oxides under humidified atmosphere have been proposed,[14] as shown in Equations (19–21) and **Figure 3**.

$$\text{Hydration}: O_O^{\times} + V_O^{\cdot\cdot} + H_2O \rightleftharpoons 2OH_O^{\cdot} \quad (19)$$

$$\text{Hydrogenation}: H_2O + 2O_O^{\times} + 2h^{\cdot} \rightleftharpoons 2OH_O^{\cdot} + \frac{1}{2}O_2 \quad (20)$$

$$\text{New hydration}: Mn\,(III)_{Mn}^{\times} + V_O^{\cdot\cdot} + O_O^{\times} + H_2O \rightleftharpoons Mn\,(IV)_{Mn}^{\cdot} + 2OH_O^{\cdot} \quad (21)$$

The hydration reaction (Equation (19) and Figure 3a) delineates the proton uptake process by which a water molecule decomposes into a proton (H^+) and a separate hydroxide ion (OH^-). Subsequently, the generated H^+ will combine with surrounded lattice oxygen ($O_O^{\times}$) to form the $OH^{\cdot}$ at the corresponding lattice oxide ion site, while the OH^- will occupy the oxygen vacancy ($V_O^{\cdot\cdot}$) site within the lattice oxide. This mechanism emphasizes the crucial role of lattice oxygen and oxygen vacancies in perovskite oxides in proton absorption. The rate of the hydration process, crucial for absorbing vapor from the surrounding environment, profoundly reflects the concentration of protons (expressed as C_H) incorporated into the material.

Another pathway for proton uptake, as described by Equation (20) and depicted in Figure 3b, involves the hydrogenation reaction. In this process, protons are assimilated while releasing oxygen through the interaction between two lattice oxygen atoms and steam, resulting in the depletion of holes within the oxides. This phenomenon is inherently favorable for perovskite oxide air electrodes possessing ample holes. Furthermore, this mechanism suggests that the concentration of lattice oxygen and holes may substantially influence the C_H within the material, whereas the concentration of oxygen vacancies may not play a significant role.

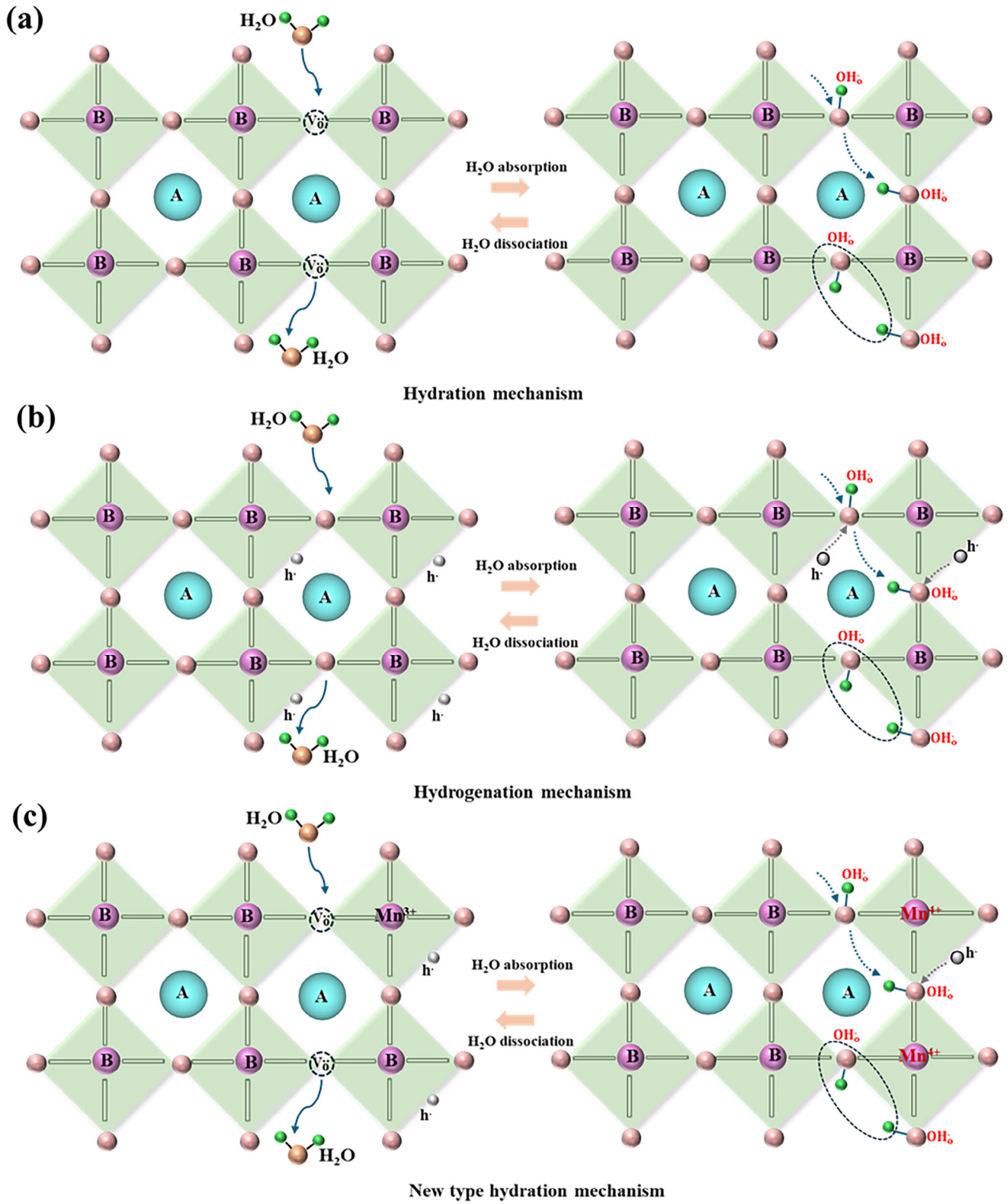

Figure 3. Three mechanisms for proton uptake:[14] a) hydration mechanism; b) hydrogenation mechanism; c) new hydration mechanism.

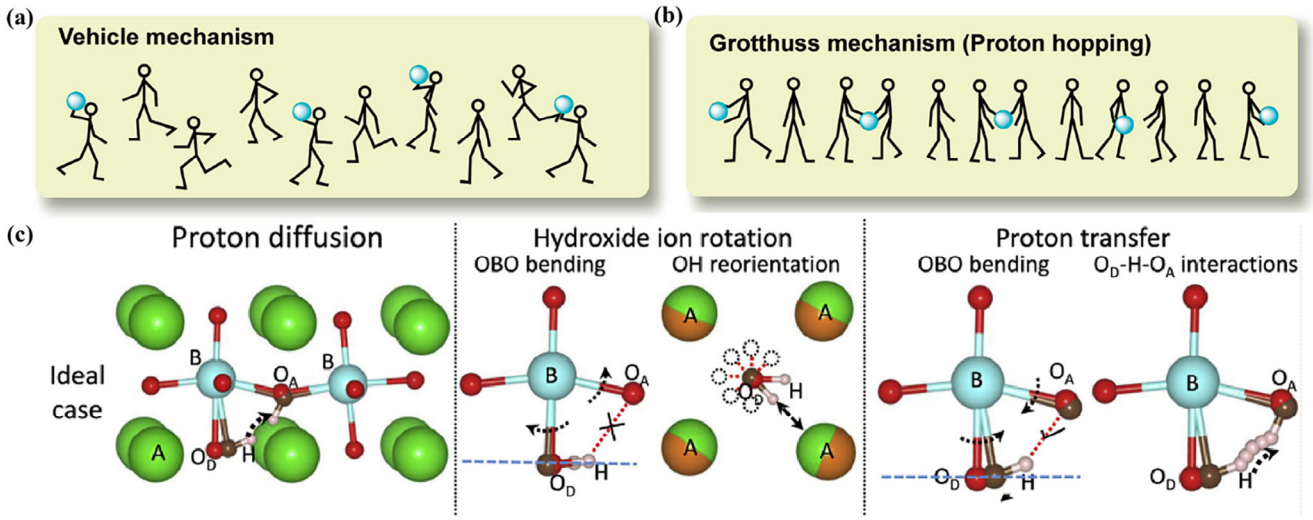

Figure 4. Mechanism for protons conduction: a) Vehicle mechanism and b) Grotthuss mechanism; c) the sub-steps for Grotthuss mechanism. a,b) Reproduced with permission.[15] Copyright 2008, American Chemical Society. c) Reproduced with permission.[16] Copyright 2020, Elsevier.

A recent proposal elucidated a third plausible pathway for proton uptake, which emerged from studies conducted on the air electrode material $La_{0.7}Sr_{0.3}MnO_{2.95}$ (LSM) oxide. As articulated by Equation (21) and Figure 3c, this novel hydration reaction is propelled by the coupling of the attraction between $V_O^{\cdot\cdot}$ and H_2O molecules, alongside carrier exchange involving oxygen holes ($O_O^{\cdot}$) and metal ions. Specifically, the OH^- produced from H_2O decomposition will occupy the $V_O^{\cdot\cdot}$ site, thereby inducing the oxidation of adjacent Mn cations within the LSM oxide lattice. Simultaneously, the $O_O^{\cdot}$ site is substituted by the single H^+ to maintain electrical neutrality. This reaction increases complexity due to the involvement of redox-active metal ions in conjunction with a substantial quantity of both $V_O^{\cdot\cdot}$ and $O_O^{\cdot}$.

In addition to proton generation, the mechanisms governing proton transport are also imperative. Currently, the vehicle and Grotthuss mechanisms, as proposed by Kreuer et al.,[17] are widely accepted to describe the proton migration process in oxides. In the vehicle mechanism (**Figure 4a**), oxygen ions serve as carriers to facilitate proton transport by forming OH^- species (resulting from the bonding between oxygen ions and protons) within the perovskite oxide lattice. This mechanism implies that the migration rate of protons is contingent upon the diffusion rate of oxygen ion carriers. Consequently, proton conduction via this mechanism leads to a relatively high activation energy (Ea, exceeding 0.4 eV) due to the limited mobility of carriers resulting from their larger size.

On the other hand, the Grotthuss mechanism (Figure 4b) entails the migration of protons or proton defects from one oxygen ion to another through the formation and cleavage of O—H chemical bonds, resulting in a lower Ea value (<0.4 eV). Thus, owing to the reduced energy required for proton conduction, the Grotthuss mechanism is generally favored in proton-conducting oxides. This mechanism entails two sub-steps for proton migration (Figure 4c):[18] 1) rotation, where the formed O—H bonds are oriented towards neighboring oxygen ions, and 2) hopping, where the rotated O—H bond is broken, allowing the proton to hop from the parent site to another oxygen ion site via the presence of proton defects. Numerous DFT studies have reported proton migration barriers, revealing that the reorientation of protons around the oxide ion to which they are bound typically exhibits a lower energy barrier than proton transfer to a neighboring oxide ion, both in perovskite electrolytes and electrode oxides. The calculated proton transfer barriers generally fall within the range of 0.25–0.5 eV.[19]

2.2.3. Oxygen Conduction Mechanism

In addition to the commendable proton generation and transport capabilities, the remarkable oxygen ion transport capacity is also important for ORR/OER. Furthermore, owing to the larger dimensions of oxygen ions, their transport barriers are inherently higher compared to those of protons. Thus, a profound comprehension of oxygen ion transport mechanisms is imperative to selectively optimize diffusion pathways, thereby macroscopically accelerating electrode reaction kinetics.

Three oxygen ion transport mechanisms are available for oxides, dependent on the nature of point defects within the systems: the interstitial, interstitialcy, and vacancy mechanisms. In the interstitial mechanism (**Figure 5a**), oxygen ions located at interstitial sites within the oxide lattice undergo thermal activation-induced jumps from one interstitial site to an adjacent one, thus facilitating oxygen ion migration. Consequently, the distance and pathway of interstitial ion jumps directly impact the rate of oxygen ion migration, without the necessity for other lattice defects to take part in this process. Additionally, upon completion of a single jump, there is no permanent displacement of other lattice ions from their equilibrium positions. Conversely, the interstitialcy mechanism (Figure 5b) posits that interstitial ions displace lattice ions from their equilibrium positions, prompting lattice ions to jump to adjacent interstitial sites and thereby facilitating oxygen ion migration within the lattice. Both mechanisms underscore the pivotal role of interstitial oxygen ions, which represent point defects in the lattice.

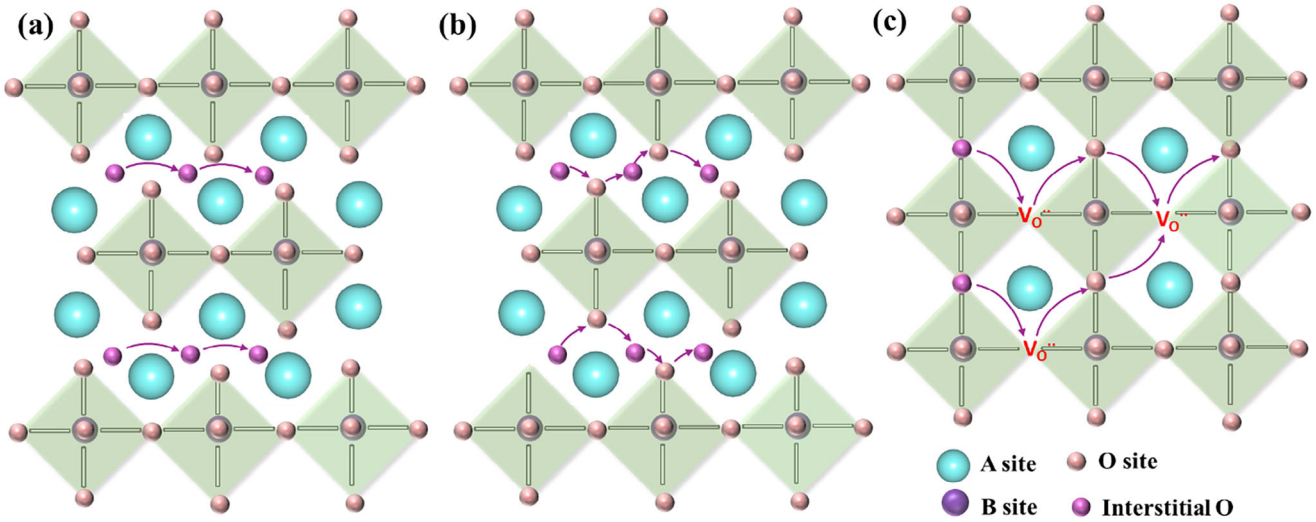

Figure 5. Schematic diagrams of oxygen conduction mechanisms: a) interstitial mechanism and b) interstitialcy mechanism in R–P perovskite; and c) vacancy diffusion mechanism in single perovskite.

On the other hand, in the vacancy mechanism (Figure 5c), oxygen ions transport by jumping to a neighboring oxygen vacancy site within the lattice. Consequently, the existence of vacancies is critical for oxygen diffusion, and their concentration within the lattice profoundly influences kinetics. Furthermore, it has been documented that oxygen ion transport adheres to the vacancy diffusion mechanism in single perovskites due to the close structural arrangement of lattice sites, while interstitial oxygen diffusion mechanism occurs in certain layered perovskites with a Ruddlesden-Popper (R-P) structure due to the surplus oxygen at the rock layer.[20]

2.2.4. Electronic Conduction Mechanism

When incorporating perovskite oxides into air electrode materials, the electronic conductivity becomes a paramount consideration. Presently, the conductivity range of most perovskite air electrode materials spans from 1 to 100 S cm^{-1} at temperatures ranging between 300 and 700 °C, which notably surpasses that of protons and oxygen ions, particularly at lower temperatures. Nonetheless, elevated conductivity can significantly contribute to catalytic enhancement, facilitate reaction kinetics, and mitigate overall ohmic resistance of the R-PCECs. The electronic conductivity in perovskite oxide stems from the polaron hopping mechanism instigated by transition metal ions with variable valence anchored in the B-site. This mechanism entails electron defects moving between B-site cations and oxygen ions, aligning with the Zener double exchange process. Consequently, an enhanced concentration of redox couples (variable valence metal ions in the B-site) theoretically yields increased electrical conductivity, but it also depends on the specific lattice structure. For instance, the emergence of oxygen vacancies or heterointerfaces in multiphase may serve as electron traps, causing a decline in conductivity. The distinct conductivity profiles of various perovskite oxides can be dissected using band theory, which delineates the distribution of electronic states or the density of states (DOS), serving as pivotal descriptors for regulating diverse physical and chemical properties both at the surface and within the bulk.

3. Factors Affecting Air Electrode Performance

Understanding the factors that govern the catalytic performance of air electrodes is of paramount importance. The intrinsic properties of air electrodes, such as oxygen vacancy concentration, lattice and interstitial oxygen content, phase structure, lattice-free volume, chemical disorder, oxygen basicity, ionization potential, and metal-oxygen bonding, are critical determinants of their triple-conductivity and stability. These factors, however, are often interdependent and may exhibit conflicting influences. This section provides an in-depth discussion of recent progress and insights into these intrinsic factors. Additionally, external operational conditions, including temperature, steam, and oxygen partial pressures, as well as the microstructural characteristics of air electrodes, exert a profound influence on electrode reaction kinetics. These effects will be further analyzed and substantiated in the subsequent sections.

3.1. Oxygen Vacancies

The presence of oxygen vacancies ($V_O^{\cdot\cdot}$) enables high oxygen ion mobility since they act as the active sites for oxygen absorption and diffusion of oxygen ions according to the vacancy diffusion mechanism. Therefore, it is generally believed that the higher $V_O^{\cdot\cdot}$ promotes oxygen and proton diffusion.[21] At the same time, the $V_O^{\cdot\cdot}$ concentration in perovskite oxides leads to the electronic, crystal structure, and surface chemistry state change, thus altering the ORR/OER catalytic performance.[22]

Specifically, to maintain the charge neutrality of the perovskite oxide, the formation of $V_O^{\cdot\cdot}$ is also accompanied by the generation of both electron holes and redox couples as additional charge compensators, influencing its electronic structure.[23] Taking the

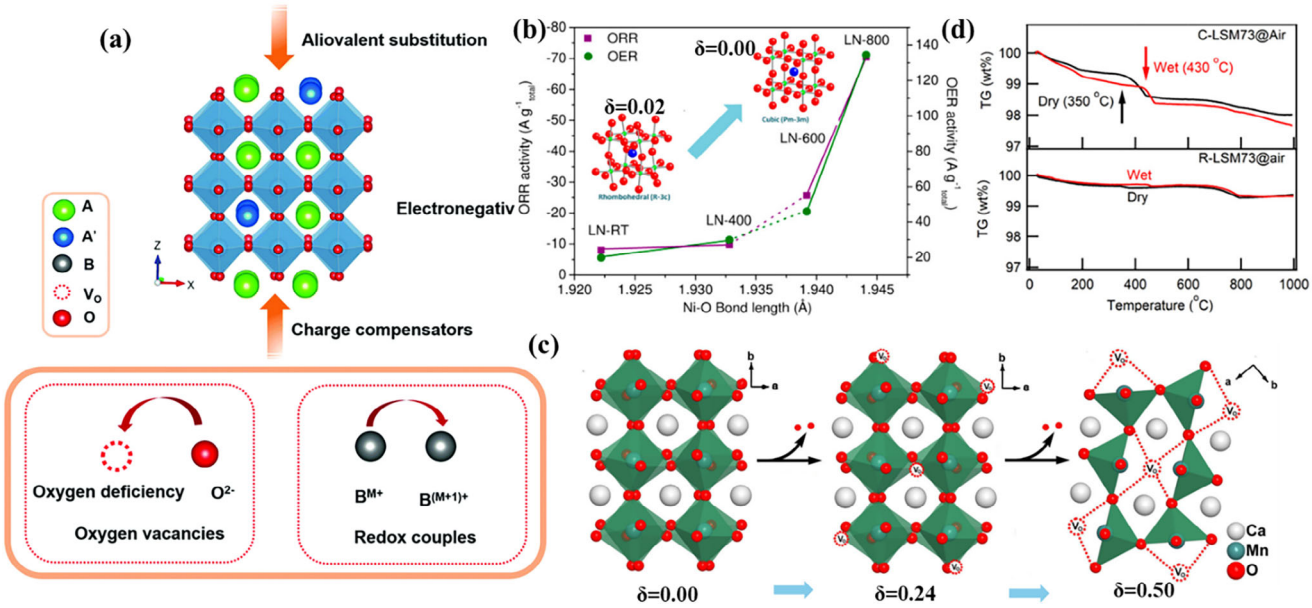

Figure 6. The altered properties associated with oxygen vacancies: a) the formation of redox couples; b) the crystal structure and catalytic performance; c) the crystal structure; d) the C_H values. a) Reproduced with permission.[22] Copyright 2020, Royal Society of Chemistry. b) Reproduced with permission.[31] Copyright 2013, American Chemical Society. c) Reproduced with permission.[32] Copyright 2014, American Chemical Society. d) Reproduced with permission.[14] Copyright 2019, American Chemical Society.

case of aliovalent substitution as an example (**Figure 6a**), the electrons of B site transition metal ions may get rid of the covalent bond and become free electrons, thus leaving behind electron holes and forming the redox couple of $B^{(x+)}/B^{(x+1)+}$. Furthermore, the adjacent electrons can fill the hole with the generation of a new hole in an electric field, leading to electron migration. Thus, the oxides exhibit enhanced electrical conductivity[24] and lower charge transfer resistance, which is necessary between the active sites and oxygen species (such as O_2 and —OOH), resulting in fostered ORR and OER processes.[25] On the other hand, the redox couple is also favorable for charge transfer between the oxygen and B-site cation based on valence bond theory.[26] For example, in Sr-doped $LaCoO_3$, the formation of a redox couple leads to a significant overlap of the Co 3d and O 2p orbitals, thus decreasing the Fermi energy of the Co 3d/O 2p π^* band. This can facilitate the adsorption of oxygen and the subsequent charge transfer between oxygen and metal ions, thus improving the catalytic activity.[27] Similar results were also confirmed by the $La_xCa_{0.4}CoO_3$ and $(La_{1-x}Sr_x)_{0.98}MnO_3$ oxides with $Co^{2+}/Co^{3+}/Co^{4+}$ and Mn^{3+}/Mn^{4+} redox couples.[28] However, it does not mean that the conductivity of the perovskite oxide is proportional to the population of oxygen vacancies. For example, it was found that for perovskites $SrFeO_{3-\delta}$, its electrical conductivity is over 1 S cm^{-1} when $\delta \leq 0.26$, while the electrical conductivity is lower than 10^{-3} S cm^{-1} when δ is over 0.40.[29] This is mainly due to the fact that the $V_O^{\cdot\cdot}$ act as the scattering centers or random traps for electrons.[30]

In addition, the crystal structure and surface chemistry also change with the concentration of $V_O^{\cdot\cdot}$. For example, the crystal structure of $LaNiO_{3-\delta}$ is transited from a rhombohedral structure to a cubic structure (Figure 6b) when the oxygen vacancy content decreases from 0.02 to 0 by quenching at different temperatures,[31] and the lattice of $CaMnO_{3-\delta}$ expands from the *Pnma* space group to *Pbma* with the increasing $V_O^{\cdot\cdot}$.[32] (Figure 6c). The distorted crystal lattice leads to changes in the lengths and angles of the B-O chemical bonds, thus affecting oxygen adsorption and intermediate/product dissociation ability.[33] Meanwhile, the surface chemistry, which include the active sites, surface element composition, and charged surface cations, is altered by the oxygen vacancies, thus influencing the adsorption/desorption of oxygen,[34] as confirmed by the barium cations exuding from bulk to surface in $Ba_{0.5}Sr_{0.5}Co_{0.2}Fe_{0.8}O_{3-\delta}$ and the different charged surface cations in $La_{0.6}Ca_{0.4}CoO_{3-x}$ and Sr-substituted $La_{1-x}Sr_xMnO_3$ oxides.[35]

Furthermore, based on the hydration and Grotthuss mechanisms, $V_O^{\cdot\cdot}$ associated with B-site cations plays a crucial role in proton uptake and conduction. For example, water uptake and protonic conductivity are absent in stoichiometric $A_2(B'B'')O_6$ and $A_3(B'B_2'')O_9$ compounds, and both increase with increasing nonstoichiometry.[36] Additionally, the cubic $La_{0.7}Sr_{0.3}MnO_{2.95}$ (C-LSM73) exhibits a C_H that is 10 times higher than that of the rhombohedral $La_{0.7}Sr_{0.3}MnO_{2.98}$ (R-LSM73) under identical conditions, attributed to the greater abundance of oxygen vacancies in the cubic structure[14,37] (Figure 6d). Similar behavior has been observed in C and R-(La, Sr) (Mn, Ni) $O_{3-\delta}$ and Zr^{4+}-doped $Sr_2Fe_{1.5}Mo_{0.5}O_{6-\delta}$ (SFMZ) perovskite oxides.[37,38] However, it's important to note that $V_O^{\cdot\cdot}$ does not determine proton uptake in oxides, as it may also occur via a hydrogenation mechanism. Moreover, the high $V_O^{\cdot\cdot}$ concentration may hinder the transport of protons, leading to the high proton transport activation energy and low proton conductivity, as confirmed by the Zn substituted $BaCo_{0.4}Fe_{0.4}Zn_{0.1}Y_{0.1}O_{3-\delta}$ air electrode.[39]

3.2. Lattice Oxygen or Interstitial Oxygen

In high-temperature bifunctional (ORR/OER) catalysts, $V_{\ddot{O}}$ is not the only crucial factor for achieving high activity in both ORR and OER. Interstitial O^{2-} and highly active lattice oxygen also play significant roles in enhancing ORR and OER kinetics through interstitial and interstitialcy mechanisms for oxygen ion migration and the hydrogenation mechanism for proton uptake.[40]

For example, Sr^{2+}-doped and undoped $La_2Co_xNi_{1-x}O_4$ samples showed no distinct peaks in electron paramagnetic resonance (EPR) spectra, indicating the absence of $V_{\ddot{O}}$.[41] This absence is primarily due to the higher formation energy of $V_{\ddot{O}}$ (4.33 eV) and the lower energy barriers for interstitial oxygen ion migration (0.58 eV along the [100] direction) compared to traditional LSCF (3.47 eV) and interstitial oxygen migration across the perovskite-like layer (1.85 eV along the [001] direction).[41] Consequently, a high concentration of interstitial O^{2-} ions in the AO layer is more likely to exist and become the dominant pathway for oxygen transport in RP oxides.[42] This is further supported by experiments with low-valence Sr^{2+} doping at La^{3+} sites in $La_2Co_xNi_{1-x}O_4$ samples, which reduced the interstitial O^{2-} by decreasing the B-site valence, leading to lower oxygen conductivity (**Figure 7**a,b).

Additionally, perovskite-like layers with highly active lattice oxygen serve as important active centers for catalytic reactions.[43] In these layers, octahedrons containing active lattice oxygen ions can convert adsorbed O_2 and H_2O into —OOH, —OO, and HO_2^- during ORR, and transform —OH into —OOH, —OO, and ultimately O_2 during OER processes.[44] Many studies have shown that the lattice oxygen could participate in the OER processes directly via a lattice oxygen-mediated mechanism.[45] The catalytic efficiency of lattice oxygen in perovskite-like layers primarily depends on the rapid removal and repositioning of O^{2-} ions at the octahedral corners, which is governed by the bonding energy of B-O chemical bonds. Moreover, longer B-O bond lengths and larger ionic spaces between B-site cations and oxygen ions enhance the mobility of lattice oxygen, further improving catalytic performance.[44] In the meantime, distorting the BO_6 octahedra by modulating the asymmetric bonding in the oxygen octahedron ($(A\text{-})_4O(\text{-}B)_2$) and enhancing Fe^{4+}–O^{2-} interaction are also feasible to activate lattice oxygen (Figure 7c), thus improving the ORR/OER catalytic performance.[46]

In proton uptake and diffusion processes, lattice oxygen plays a key role, particularly in the hydrogenation and Grotthuss mechanisms. Proton absorption at lattice oxygen sites typically requires oxygen to exhibit significant basicity, which will be discussed in detail later. Proton transport via lattice oxygen occurs through either the movement of lattice oxygen or proton hopping between adjacent lattice oxygen atoms. For efficient proton transfer, it is expected that the high bulk or surface mobility of lattice oxygen and shorter O-O bond lengths are essential to facilitate faster proton transport.[47] This indicates that both proton and oxygen ion transport are closely linked to the activity of lattice oxygen under certain conditions. Moreover, there is a strong relationship between the two active ions. For example, oxygen affinity (defined as the energy released when an oxide ion enters a $V_{\ddot{O}}$ near a dopant atom) is a critical parameter for evaluating the proton conductivity of a material[48] (Figure 7d).

3.3. Phase Structure

The phase structures of perovskite oxides are essential for air electrode materials because they predetermine mixed electron and oxygen-proton-ion conductivity, cation segregation (e.g., through elastic energy minimization), and stability.[49] First, for different types of perovskite oxides, oxygen ion migration in single perovskite is mainly conducted by the vacancy diffusion mechanism, while in RP oxides can occur through both oxygen vacancy and/or oxygen interstitial processes which depend upon the oxygen stoichiometry.[50] Moreover, the oxygen and steam are incorporated into crystal lattice by the oxygen vacancy for single perovskite oxide, while that can be incorporated through the rock-salt layer for RP oxides. Specifically, the water molecules are embedded into the sites within the rock-salt layers without dissociation into H^+- and OH^--ions, but hydrated as separated $(H_2O)n$/hydroxyl layer within the lattice.[51] Meanwhile, the flexible and deformable isolated tetrahedral units-based structure in $LaVO_4$ series can also promoteoxygen ion and proton transport.[52] Typically, the hydration will lead to the expansion of interlayer space and is accompanied by the structural rearrangement and the increase of coordination number of A-site cations.[53] These various oxygen-proton diffusion and incorporation paths lead to unevenness proton-oxygen kinetics within the different lattice structures.

Furthermore, the Goldschmidt tolerance factor (τ) is a geometric indicator that predicts perovskite phase stability:[54] 1) $\tau > 1$ favors hexagonal or tetragonal phases; 2) τ close to 1 promotes cubic structures; 3) $\tau < 0.9$ encourages orthorhombic or rhombohedral phases. When τ deviates from 1, structural changes occur, reducing symmetry by bending O–B–O bonds to align with O–A–O bonds, leading to bond angles below 180° and resulting in orthorhombic or monoclinic structures.[55] Perovskites with high symmetry are generally believed to have superior proton and oxygen conductivity.[56] As the structure shifts from cubic to less symmetric forms (orthorhombic, tetragonal, etc.), O–O and M–O bond distances increase, extending the migration path for oxygen ions and protons. This increased hopping distance impairs mobility and increases the activation energy for conduction.[57] Additionally, phase distortions or lower symmetry phases create inequivalent oxygen sites, which can form isolated low-energy traps for protons and oxygen ions, further inhibiting their movement.[56b] Varying hydration enthalpies, which depend on bond distances and local environments, also impact proton absorption and conduction, with lower enthalpies generally supporting better proton conduction.[58]

3.4. Lattice Free Volume

The lattice-free volume (V_f) is defined as the unit cell volume minus the total volume of the constituent ions within the perovskite unit cell, which is tightly related to the ionic radii of the ions in A, B, and O sites.[59] Typically, a larger V_f is more desirable to obtain faster oxygen ion mobility since it offers more free space for oxygen ions migration[13b,60] (**Figure 8**a) and enhances the vacancy diffusion coefficient to reduce the migration-energy barriers according to DFT results[61] (Figure 8c,d). For example, the large Gd^{3+} cations doped $BaFe_{0.975}Gd_{0.025}O_{3-\delta}$ sample displayed lower

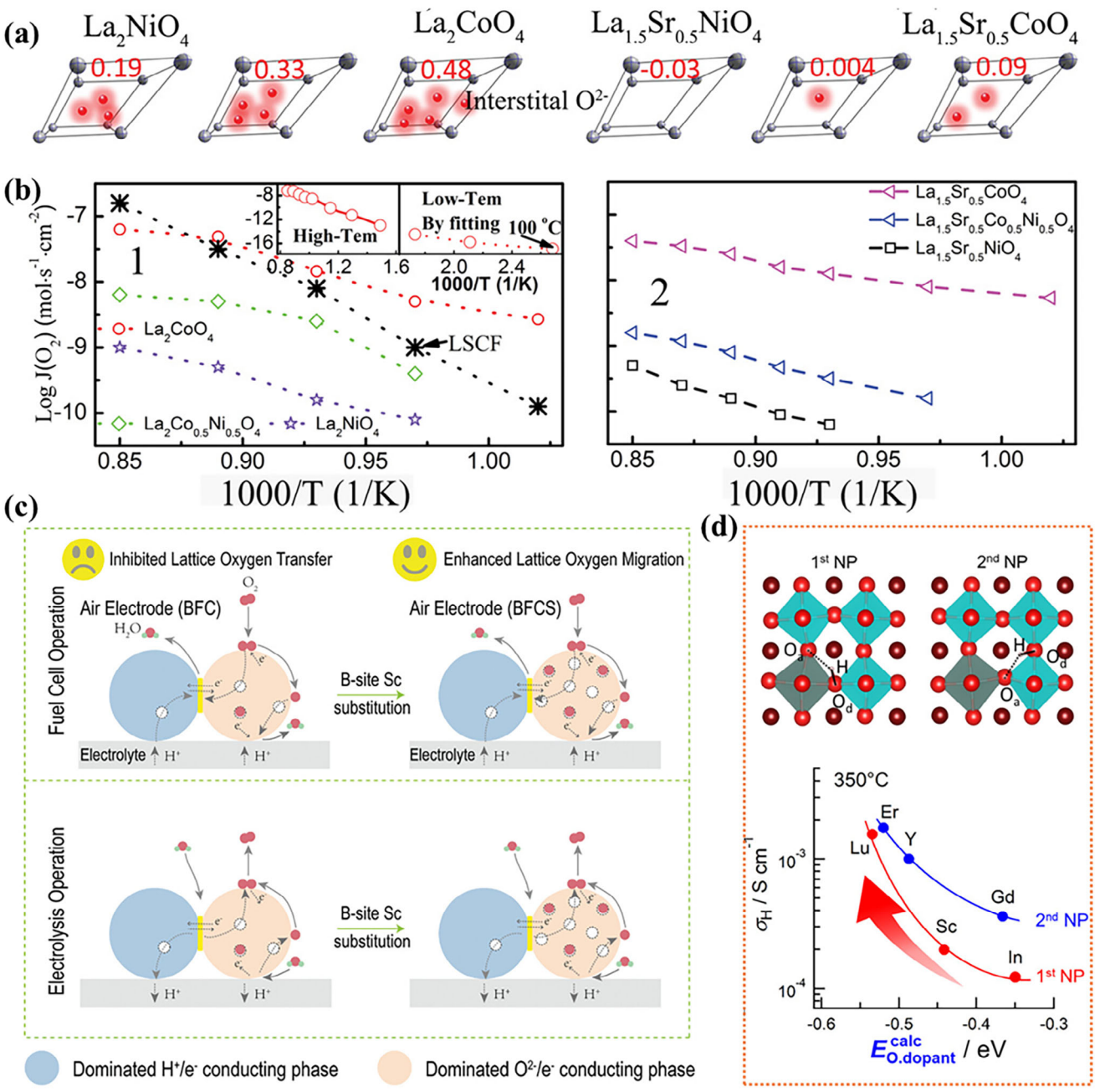

Figure 7. The effect of lattice and interstitial oxygen: a) interstitial O^{2-} concentration in AO layer of $La_xSr_{2-x}Co(Ni)O_4$ and b) corresponding oxygen permeation flux results; c) the accelerated ORR/OER mechanisms; d) the diagrams of local structures around a dopant atom and proton on first and second nearest proton (NP) sites and the different proton conductivity with various oxygen affinity energies. a,b) Reproduced with permission.[41] Copyright 2019, Wiley. c) Reproduced with permission.[46b] Copyright 2024, Wiley. d) Reproduced with permission.[48] Copyright 2024, American Chemical Society.

oxygen migration energy compared to that of pristine $BaFeO_{3-\delta}$ due to the expanded lattice structure (Figure 8b), achieving a higher oxygen permeation flux of 1.37 mL cm^{-2} min^{-1} for a 1 mm thick membrane at 950 °C.[62] A similar trend was observed when the larger Ba^{2+} replaced Sr^{2+} in the $SrCoO_3$-based air electrode. The $Sr_{0.8}Ba_{0.2}Co_{0.8}Sc_{0.1}Nb_{0.05}Ti_{0.05}O_{3-\delta}$ composition exhibited a higher V_f compared to the Ba-free sample. The expansion of the parent lattice created additional free space for oxygen migration, which lowered both the oxygen vacancy formation energy and the oxygen migration barrier.[63] Interestingly, an increase in unit cell volume was sometimes observed even when substituting a smaller ion, such as replacing Sr^{2+} with Pr^{3+} or La^{3+}, which seems counterintuitive.[64] This phenomenon is explained by the formation of electron holes, which transform the (Sr, La)FeO_3 series from an insulator to a p-type semiconductor.[64b] It is worth noting that a negative linear relationship between τ and V_f was

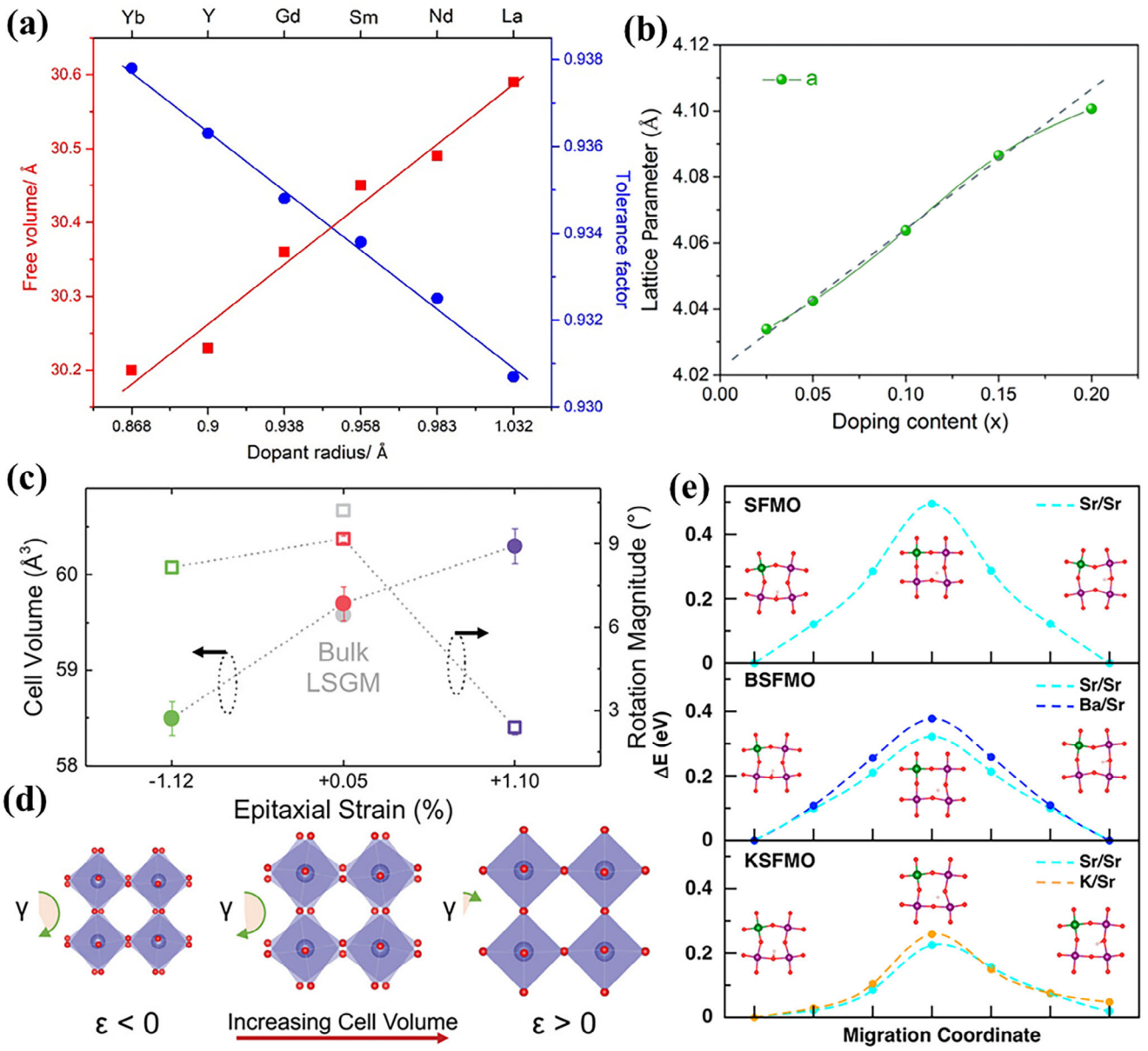

Figure 8. a) Dependence of V_f and τ on dopant ion radius in $BaCe_{0.9}Ln_{0.1}O_{3-\delta}$ oxides; b) lattice parameters of the $BaFe_{1-x}Gd_xO_{3-\delta}$ samples; c) extraction of the unit-cell volume and the effective octahedral rotation magnitude as a function of strain state; and d) Schematic illustration of the increasing cell volume with varying strain; e) the different proton migration features in SFMO derivatives with various V_f. a) Reproduced with permission.[13b] Copyright (2021), Elsevier. b) Reproduced with permission.[62] Copyright 2016, Royal Society of Chemistry. c,d) Reproduced with permission.[61] Copyright 2019, Wiley. e) Reproduced with permission.[19b] Copyright 2016, American Chemical Society.

observed both in the La- and Nd-based single perovskite series.[65] Specifically, the τ becomes smaller when V_f increases, indicating that the deformation from the cubic lattice is more serious which makes the oxygen ions more difficult to jump due to a local strain of the lattice. To balance these two factors, the maximum conductivity is always obtained when the optimum τ value is around 0.96 and the V_f reaches the highest value, which is further confirmed by the oxygen transport phenomena in cubic $CaTiO_3$ and $SrTiO_3$.[66] Moreover, lattice contraction can also be leveraged to enhance oxygen electrode catalytic activity. For instance, doping Ce ions into the $LaCoO_3$ lattice induces contraction, which modulates the charge density at the active Co center. This improves electrical conductivity, reduces the reaction-free energy, and accelerates the rate-determining steps in both ORR and OER kinetics, resulting in improved overall performance.[67]

Another important role of V_f is to provide free space for proton reorientation, as described by the Grotthuss mechanism. A moderately expanded cell, primarily due to the larger ionic radii of metal cations, can theoretically reduce the energy barrier for proton rotation and enhance proton conduction. For example, the larger ionic radii of Ba^{2+} (135 pm) and K^+ (138 pm) compared to Sr^{2+} (118 pm) can significantly reduce the proton

conduction energy barriers, from 0.495 eV for $Sr_2Fe_{1.5}Mo_{0.5}O_{6-\delta}$ to 0.322 eV and 0.225 eV for $Ba_{0.25}Sr_{1.75}Fe_{1.5}Mo_{0.5}O_{6-\delta}$ and $K_{0.25}Sr_{1.75}Fe_{1.5}Mo_{0.5}O_{6-\delta}$, respectively[19b] (Figure 8e). A similar reduction in energy barriers was observed for $Ba_{0.5}Sr_{0.5}Co_{0.8}Fe_{0.2}O_3$ (0.55 eV) and $Ba_{0.4}K_{0.1}Sr_{0.5}Co_{0.8}Fe_{0.2}O_{3-\delta}$ (0.41 eV), attributed to the larger K^+ radius.[68]

In $BaZr_{0.8}Y_{0.2}O_3$, the presence of zero, one, or two Ba ion vacancies at the A-site exhibit distinct proton dynamics.[16,69] While A-site deficiencies increase free space for proton reorientation (favoring small-angle hydroxide ion rotation), they also strengthen the bond between oxygen and adjacent A-site ions, increasing the energy needed for large-angle hydroxide ion rotation, thus inhibiting reorientation. Interestingly, A-site deficiencies in some TCO air electrode materials improve proton uptake and migration, as evidenced by the higher C_H value of $Ba_{0.9}Co_{0.4}Fe_{0.4}Zr_{0.1}Y_{0.1}O_{3-\delta}$ (0.0232 mol unit^{-1}) and the lower proton migration barrier of $Ba_{0.875}FeO_{3-\delta}$ (0.18 eV).[70] These contradictory effects may result from variations in base materials, defect concentrations, and ideal conditions in computational processes. A-site defects in perovskites can impact more than just free volume, influencing oxygen vacancy formation and migration, phase structure, and grain size.[69,71]

3.5. Chemical Disordering

Many studies have focused on aliovalent doping to modify carrier content within materials and enhance their conductivity. However, chemical disorder—specifically the distribution of cations across different sublattices in perovskite oxides—often results in a complex potential energy landscape.[72] This impacts both the thermodynamics and kinetics of the defects responsible for ion transport. For example, cation disorder in $GdBaCo_2O_{5+\delta}$ reduces oxygen diffusion coefficient and promotes diffusion along the c-axis of the material.[73] This is attributed to defect trapping, where oxygen vacancies are trapped between Ba atoms occupying Gd sites, lowering the overall oxygen diffusion coefficient. Similar findings have been reported for other oxides. In $Gd_{0.5}Ba_{0.5}MnO_{3-\delta}$, the oxygen chemical diffusion coefficient was significantly lower compared to its layered counterpart, $GdBaMn_2O_{5+\delta}$, which exhibited enhanced diffusion due to ordered cations.[74] However, in $Ba_{0.5}Sr_{0.5}Co_{0.8}Fe_{0.2}O_{3-\delta}$ (BSCF), a common air electrode material in solid oxide fuel cells, molecular dynamics (MD) simulations revealed that cation disorder in the A-site Ba/Sr layers increased the oxygen diffusion coefficient and reduced the activation energy for oxygen diffusion.[75] This discrepancy can be explained by differences in the charge states of cations. In BSCF, A-site disorder does not affect charge distribution, while Gd^{3+}/Ba^{2+} disorder creates charged defects ($Gd_{Ba}^{\cdot}$ and Ba_{Gd}'), which trap oxygen vacancies and hinder ion migration. These insights suggest that long-range cation ordering in perovskites with well-defined compositions, stoichiometries, and atomic arrangements may provide more predictable control over structural, geometric, and electronic properties, thus improving electrocatalytic performance.[76]

Moreover, in $A_2(B'B'')O_6$ and $A_3(B'B_2'')O_9$, higher protonic conductivity is often associated with a higher degree of B-site cation disorder.[36] This is due to several factors: 1) disorder creates B′–B′ sites that act as trapping centers for protons; 2) in ordered structures, the energy required for protons to hop between B′ and B″ ions is greater, inhibiting proton mobility; and 3) compositional inhomogeneity arising from disorder leads to variable proton concentrations, which provide charge compensation in non-stoichiometric compounds. Additionally, other oxides with disordered crystal structures exhibit excellent proton conductivity, emphasizing the role of structural disorder.[57,77] However, in some cases, ordered structures outperform disordered ones in terms of catalytic activity. For instance, $LaBaCo_2O_{5+\delta}$, an A-site-ordered air electrode material, retains a higher concentration of oxygen vacancies at low temperatures.[78] This ordering is thought to increase the basicity of the oxygen vacancies, promoting hydration and enhancing proton uptake and conductivity. In conclusion, while disorders can enhance protonic conductivity in certain perovskites, ordered structures may offer superior catalytic performance under specific conditions by promoting oxygen vacancy stability and proton transport.

3.6. Oxygen Basicity

According to proton uptake mechanisms, protonic defects are formed by regular lattice oxygen or oxygen vacancies binding with protons from surrounding water molecules. This hydration can be regarded as a pure acid-base reaction since no electron transfer occurs. Consequently, oxygen basicity is closely related to proton affinity and plays a critical role in proton uptake and transport. Reducing the electronegativity of A-site and B-site cations increases the basicity of bonded O^{2-}, resulting in enhanced proton conductivity.[47,79] This is because lower average cation electronegativity always leads to a larger negative hydration enthalpy,[11c] while higher electronegativity promotes charge delocalization, leading to proton–hole interactions that reduce overall proton conductivity.[80] For A-site cations, due to the substantially lower electronegativity of Ba (0.85) compared to Sr (0.95)/La (1.1), the Ba-based perovskites generally have a better proton uptake ability than the Sr/La-based perovskites. For example, the C_H in $Ba_{0.75}La_{0.25}FeO_{2.53}$ increases from 0.004 to 0.03 mol unit^{-1} when La is partially replaced by Ba, and the C_H of $Sr_{0.5}Ba_{0.5}FeO_{2.5}$ is significantly higher at 0.019 mol unit^{-1} compared to $SrFeO_{2.5}$ (C_H = 0.0002 mol unit^{-1}), demonstrating Ba's positive impact.[80a] Similarly, K (0.82) has also been shown to improve proton conductivity due to its high basicity[81] (**Figure 9a,b**). In addition, electronegativity of B-site cations also plays a significant role in determining the oxygen basicity of perovskite oxides. Common B-site cations follow the electronegativity order: Ni (1.92) > Cu (1.90) > Co (1.88) > Fe (1.83) > Zn (1.65) > Mn (1.55) > Zr (1.33) > Y (1.22) > Ce (1.12). Lower electronegativity at the B-site correlates with higher oxygen ion basicity and greater proton uptake ability. This is evidenced by the increased C_H in Zn-substituted Co/Fe oxides such as $Ba_{0.95}La_{0.05}Fe_{0.8}Zn_{0.2}O_{2.4}$, $Ba_{0.5}Sr_{0.5}Fe_{0.8}Zn_{0.2}O_{2.4}$, and $Ba_{0.5}Sr_{0.5}Fe_{0.8}Zn_{0.2}O_{3-\delta}$,[80a,82] and the greater hydration ability calculated for stannate and cerate compared to zirconate.[83]

Furthermore, oxygen surface exchange kinetics are strongly linked to the basicity of perovskite oxides[84] (Figure 9c,d). More basic oxides exhibit greater surface coverage of oxygen molecules, as the binding strength between molecular oxygen and the oxide surface increases with basicity.[85] This correlation is most

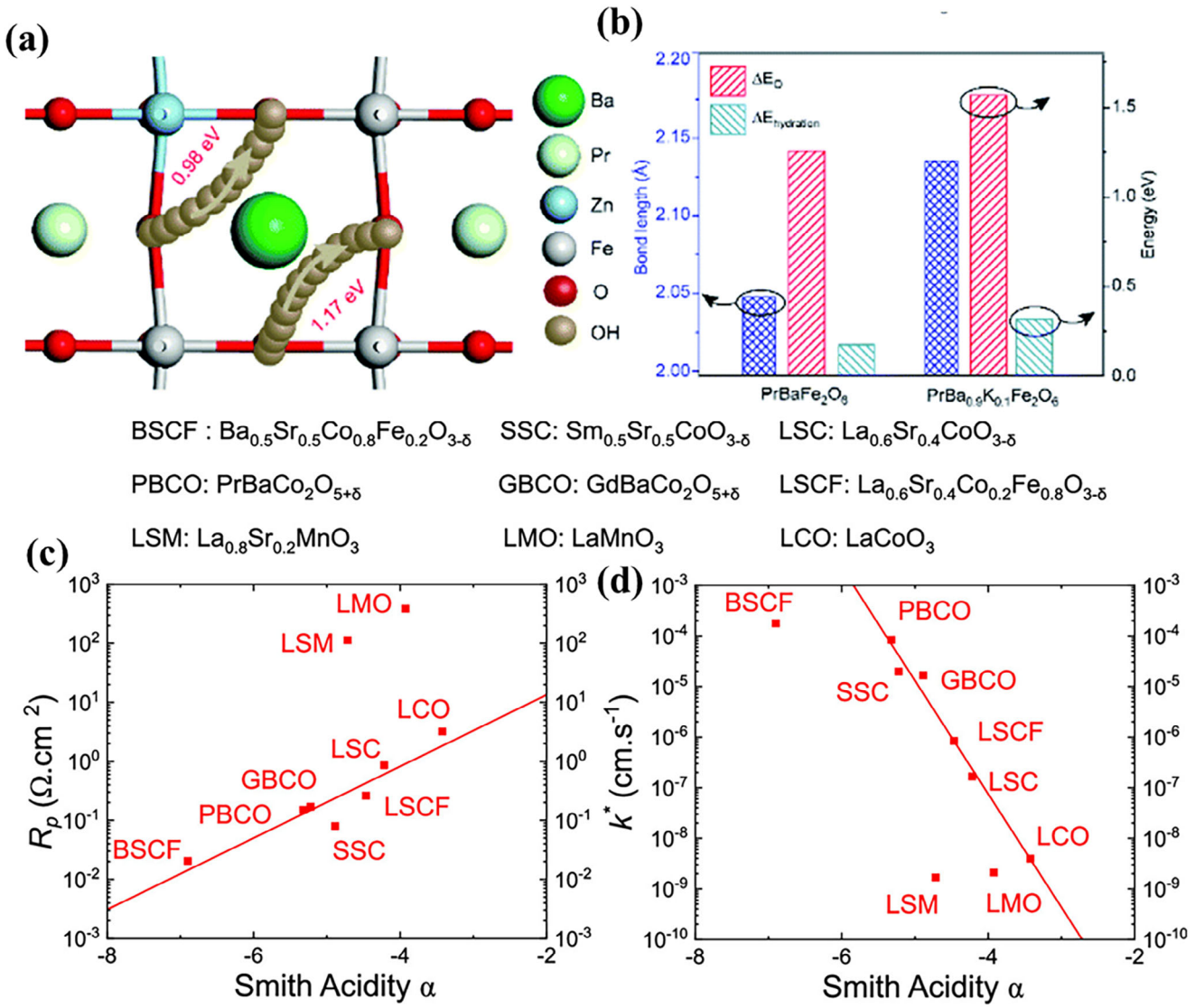

Figure 9. a) The activation energy of proton defects transfer on the oxygen vacancy near Zn or Fe site and b) the bond lengths, oxygen vacancy formation energy, and hydration energy of $PrBaFe_2O_6$ before and after K doping; c) the polarization resistance and d) the surface exchange coefficient k* as a function of Smith acidity for materials. a,b) Reproduced with permission.[81b] Copyright 2022, Royal Society of Chemistry. c,d) Reproduced with permission.[84] Copyright 2022, American Chemical Society.

evident when the oxide's mixed conductivity—both ionic and electronic—is already favorable, particularly in high-temperature gas/solid reactions.[84]

However, the high basicity of the anionic network in Ba/Sr-based materials compromises their stability. These materials tend to decompose into impurity phases, such as $BaCO_3$/$SrCO_3$ and $Ba(OH)_2$/$Sr(OH)_2$, in the presence of acidic gases (e.g., CO_2) or high water vapor partial pressures, limiting their catalytic performance and stability in practical applications.[86]

3.7. Ionization Potential

The ionization potential (IP), defined as the energy difference between the valence band (VB) maximum and the vacuum level, is closely related to the hydration enthalpy (E_{H2O}) of perovskite oxides.[87] The hydration enthalpy, which reflects the material's ability to incorporate protons, consists of the proton and hydroxide affinity, in addition to the constant gas-phase water dissociation energy ($H_2O \rightarrow H^+ + OH^-$). Specifically, hydroxide and proton affinity represent two distinct steps in the hydration process: first, an oxygen vacancy is filled by a hydroxide ion from the gas phase, followed by the attachment of the remaining proton from H_2O to an oxygen ion.[88] Proton affinity (PA) is expected to be more favorable for oxide ions with stronger basicity, whereas hydroxide affinity (HA) is favored when the surrounding cations possess a higher charge, corresponding to less basic and more acidic oxides.

These characteristics result in opposing trends for PA and HA as a function of the IP: materials with lower IP tend to exhibit

more favorable PA but less favorable HA. Despite this, materials with higher IP have a smaller distance between their O and OH states, resulting in a steeper observed slope for PA (≈1) compared to HA (≈−0.8).[87] Consequently, when considering both PA and HA, which contribute to E_{H2O}, materials with smaller IP values typically display more negative E_{H2O}, indicating enhanced hydration ability. For instance, $BaFeO_3$, which has a larger IP than $BaZrO_3$, exhibits less negative hydration enthalpy (+0.2 eV vs −1.0 eV). A similar trend is observed when comparing $BaTiO_3$.[87]

Furthermore, ideal dilute behavior may deviate due to interactions between electronic and ionic defects, particularly in redox-active perovskites where hole concentrations play a significant role. The non-ideal behavior is attributed to repulsive hole-hole interactions, which increasingly disfavor oxygen incorporation as the hole concentration rises.[89] Since protons are bound to oxide ions, the partial transfer of holes to oxygen, which alters oxygen's charge density and energy levels, also influences hydration thermodynamics. This effect was confirmed by the proton uptake and hydration van't Hoff plot for $Ba_{0.85}La_{0.15}FeO_{3-\delta}$, where the observed reduction in proton uptake was more pronounced than the slight decrease in oxygen vacancies would suggest.[80a,89d] This is explained by a detrimental hole–proton interaction, where holes are partially delocalized from B-site cations to oxygen, making hydration less favorable.

In parallel, oxygen X-ray Raman scattering (O-XRS) measurements indicated reduced delocalization of holes from Fe to O, which was correlated with increased proton uptake.[30a] Similarly, in materials such as $BaZr_{0.88-x}Y_{0.12}Fe_xO_{3-\delta}$, $BaZr_{1-x}Fe_xO_{3-\delta}$, and $BaCe_{0.7-x}Zr_{0.2}Y_{0.1}Fe_xO_{3-\delta}$, even small Fe substitutions significantly decreased proton uptake, exceeding expectations from a strictly localized defect model.[90] These findings highlight the beneficial effect of partially substituting B-site cations (e.g., Fe, Co) with typically oversized, redox-inactive cations (e.g., Zn, Y, Zr) to mitigate defect interactions.

3.8. Metal–Oxygen Bonds

The migration of oxygen ions within the perovskite lattice involves the breaking and reformation of covalent bonds with metal cations. Therefore, the strength of these metal–oxygen (M-O) bonds determines whether they can be broken easily during ion migration. In perovskites, where the BO_6 octahedron forms the basic structural framework (in both single and double perovskites), the bonding between oxygen and the smaller, more closely bound B-site cations is significantly stronger than that with A-site cations. As a result, researchers often use the average B-site metal–oxygen bond energy (B-O bond) as a proxy for the average M-O bond energy in the perovskite lattice.[55b] Generally, weaker M-O bonds are associated with lower oxygen migration barriers, as previous studies have demonstrated.[91]

Efficient vacancy-mediated oxygen ion transport requires a lower oxygen vacancy formation energy, so it is relatively easy to break M-O bonds, a key step in oxygen migration.[92] The lower oxygen vacancy formation energy observed in transition metal oxides can be attributed to weaker M-O bond strength, characterized by lower bond dissociation energy, metal ion ionization potential, enthalpy of formation, Madelung potential, as well as lower reduction potential.[93] In addition, shifting the O 2p band center closer to the Fermi level, which corresponds to reduced charge transfer from metal cations to oxygen and weaker M-O bond strength, further reduces the vacancy formation energy[92b,94] (**Figure 10**a,b). For example, in a study of over 40 Ba/Sr/Pr/La-based perovskite oxides, it was found that the oxygen migration barrier increased with higher vacancy formation energy, while it decreased with a higher O 2p band center energy[95] (Figure 10c). Similarly, Ni-doped lanthanum cobaltite-ferrite exhibits high oxygen nonstoichiometry and oxygen permeation due to the weak Ni-O bonds.[96] Likewise, doping lanthanum-ferrite-based electrodes with Cu has been shown to improve electrochemical performance[97] In general, $A^{3+}B^{3+}O_3$-type perovskites are expected to be better oxygen ion conductors, as B-O bond energy increases significantly in $A^{2+}B^{4+}O_3$ and $A^{1+}B^{5+}O_3$ perovskites, which is consistent with the lower oxygen conductivity observed in $SrTi_{0.8}Ga_{0.2}O_{2.9}$,[55b,98] despite the similar ionic radii of Sr^{2+} and Ti^{4+} compared to the typical radii of A- and B-site ions.[56a,65]

The lower oxygen vacancy formation energy, resulting from weaker M-O bonds, enhances the hydration ability of oxides, as these vacancies serve as proton uptake sites. Additionally, higher covalency in B-O bonds often leads to increased electron transfer from oxygen to the B-site cation, reducing the effective charge (and basicity) of the oxide ions. This, in turn, disfavors the generation of proton defects, as demonstrated by Zn doping in the $Ba_{0.95}La_{0.05}FeO_{3-\delta}$ air electrode.[99]

However, a more negative average B-site metal-oxygen bond energy (ABE) in perovskites (indicative of stronger M-O bonds) is associated with higher phase stability.[100] For instance, the ABE values for SFTi, SFNb, and SFCr are -308.03, -320.96, and -294.06 kJ mol^{-1}, respectively, compared to -284.36 kJ mol^{-1} for $SrFeO_{3-\delta}$, indicating that doping Ti, Nb, and Cr into the perovskite lattice increases the ABE, thereby stabilizing the perovskite structure and enhancing its resistance to CO_2 and H_2O[101] (Figure 10d).

3.9. Environmental Conditions

In addition to the intrinsic physical and chemical properties of oxides, environmental conditions during fabrication and testing, such as temperature, water partial pressure (pH_2O), and oxygen partial pressure (pO_2), significantly influence the conductivity of oxygen ions, protons, and electrons in these materials. For instance, in pure Ar gas at 900°C, the oxygen-ion conductivity of Sr_2ZnMoO_6 (SZMO) increased from 0.008 to 0.450 S cm^{-1}, while oxygen permeability improved from 0.03 to 0.78 mL cm^2 min^{-1} for SZMO samples fabricated in air (Air-SZMO) and hydrogen (H_2-SZMO), respectively[102] (**Figure 11**a–d). A similar enhancement in oxygen migration was observed when the pO_2 in the testing environment was reduced. For H_2-SZMO, the lower pO_2 caused a reduction of Mo^{6+} to $Mo^{5+/4+}$, generating more polaron electrons and enhancing electronic conductivity (Figure 11e). In addition, the increased Zn-O-Mo bond angle (due to a shorter Zn-O bond) led to a higher lattice symmetry (Figure 11f). This greater symmetry allowed for lattice relaxation, increasing the critical radius (r_c) and creating wider pathways for O^{2-} transport.[102]

The proton uptake and conduction in oxides are similarly influenced by environmental vapor pressure. For example, the C_H of the entire series of $La_{2-x}Sr_xNiO_{4+\delta}$ ($0.75 \leq x \leq 1.4$) is no more

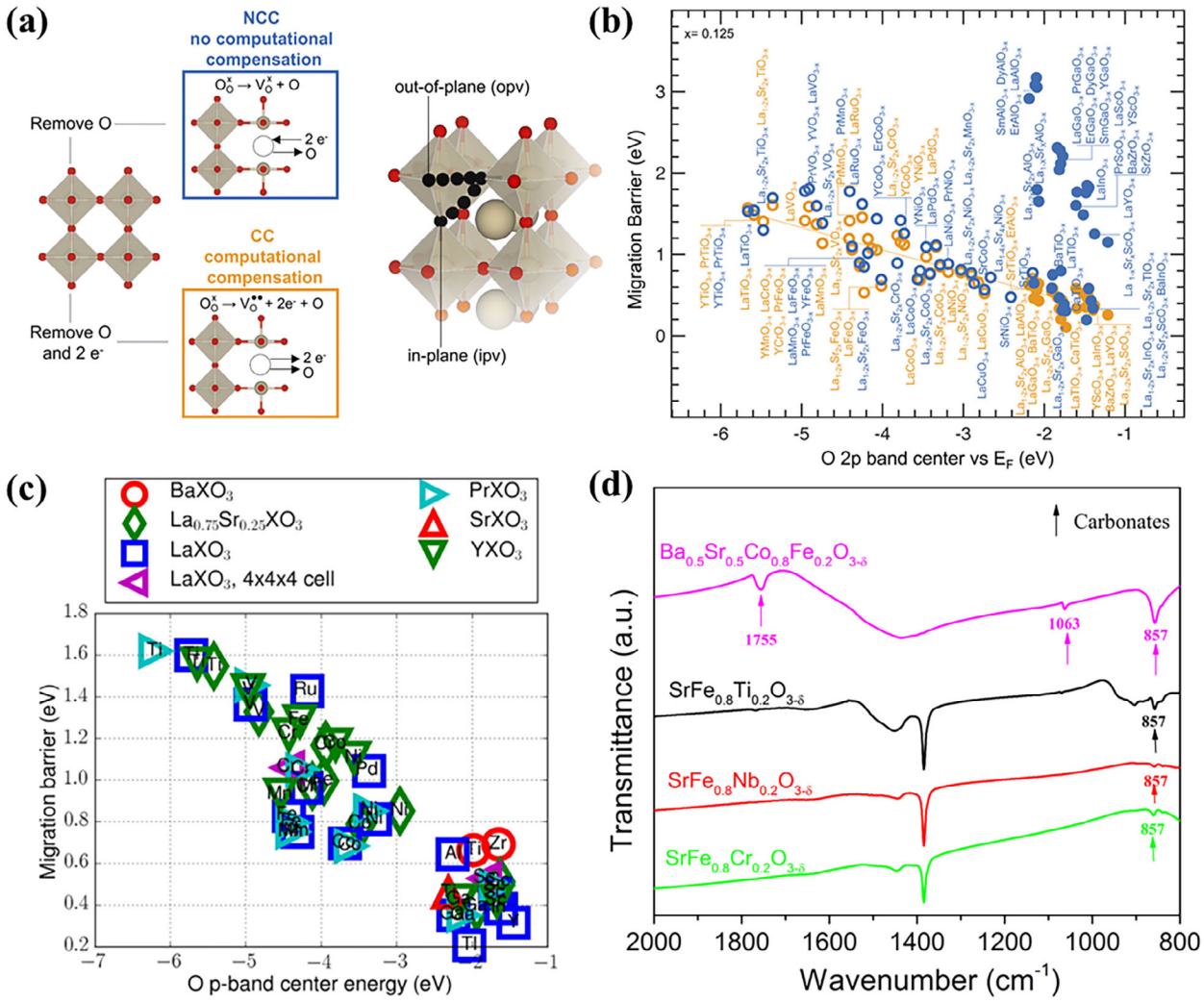

Figure 10. a) Schematic diagram of a non-computationally compensated (NCC) and a computationally compensated (CC) oxygen vacancy and its migration paths; b) the different oxygen migration barrier as a function of the energy of the O-2p and Fermi level; c) oxygen migration barrier versus oxygen p-band center energy; d) Fourier transform infrared (FT-IR) spectra of $SrFe_{0.8}M_{0.2}O_{3-\delta}$ (M = Ti^{4+}, Nb^{5+}, and Cr^{6+}) after treatment in CO_2. a,b) Reproduced with permission.[92b] Copyright 2024, Royal Society of Chemistry. c) Reproduced with permission.[95] Copyright 2016, Elsevier. d) Reproduced with permission.[101] Copyright 2016, Elsevier.

than 0.005 in an atmosphere containing 1.67% H_2O.[103] However, in an O_2–10% H_2O environment, the C_H in $La_{1.2}Sr_{0.8}NiO_{4+\delta}$ increased to 0.02.[40] Similarly, the C_H in LSM73 increased from 0.046 to 0.142 mol per unit as the water pressure (pH_2O) rose from 0.003 to 0.023 atm.[14] In $Ba_{0.85}K_{0.15}ZrO_{3-\delta}$, the dominant conduction mechanism transitioned from proton conduction to hole conduction when the atmosphere was changed from wet N_2 to wet oxidative conditions within the temperature range of 550–700 °C.[104]

4. Advances in Air Electrodes and Modification Strategies

4.1. Single Phase Air Electrode

In the past decades, perovskite oxides have been widely used as promising air electrodes for energy conversion and storage due to their outstanding catalytic activity, fine-tuned compositions and structure, and compatible thermal behavior.[105] According to the composition of the specific perovskite oxide materials with high oxygen ion and electron conductivity (partly with proton conductivity), the phase structure includes three types: single ($ABO_{3-\delta}$), double ($AA'BB'O_{6-\delta}$) and Ruddlesden–Popper (R-P) perovskite($A_{n+1}B_nO_{3n+1+\delta}$), the detailed structures are shown in **Figure** 12 and the following part.

1) $ABO_{3-\delta}$: In the single perovskite, A-site typically accommodates alkaline earth or rare earth metal ions in a 12-fold coordination and a valence of +1, +2, +3, exemplified by K, Cs, Ba, Sr, Pr, La, and Ca. For comparison, the B-site is commonly occupied by transition metal ions featuring a coordination number of 6 and a valence from +2 to +4, including Cu, Mg, Co, Fe, Ni, Zr, and Y. It is noteworthy that certain metal ions may exhibit higher valence states, such as Mo (+5 or +6),

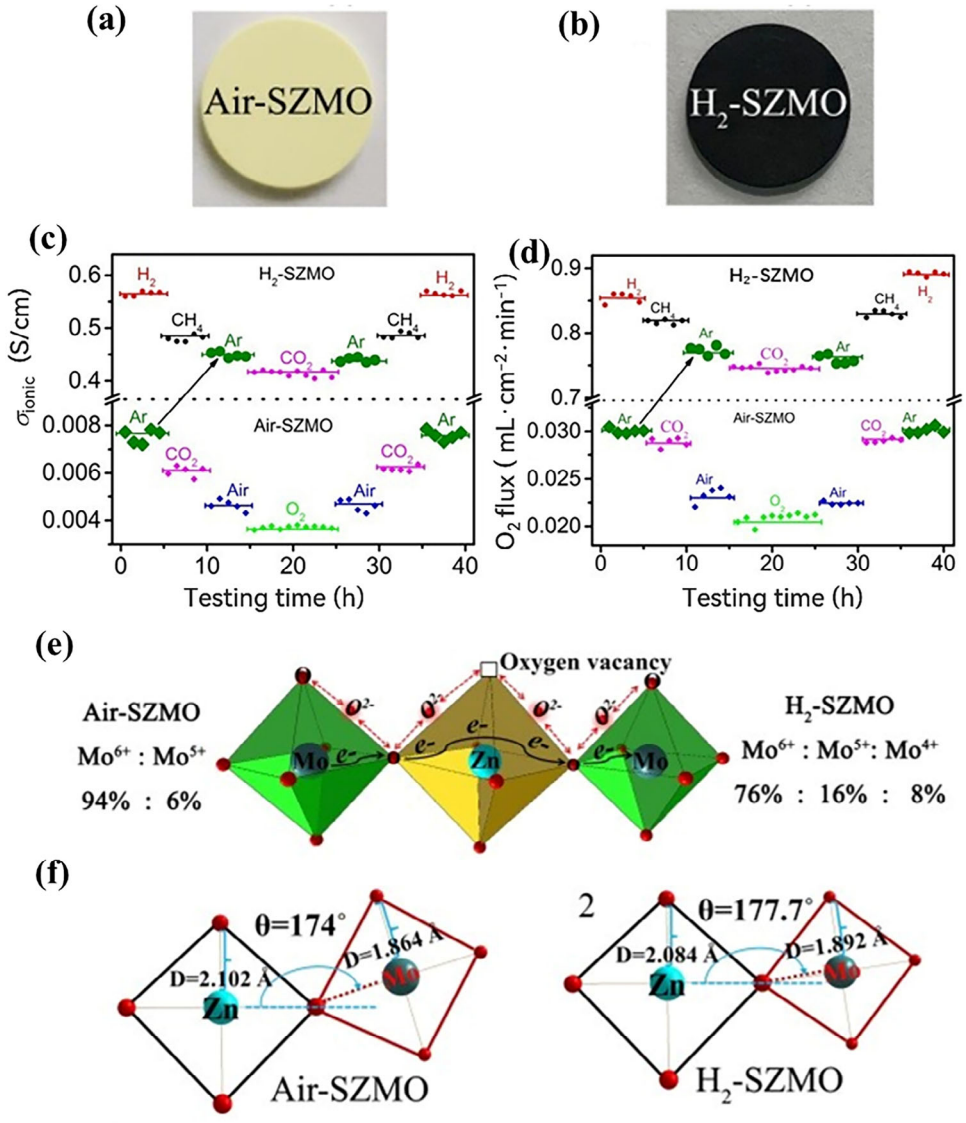

Figure 11. The environmental effect on the SZMO oxides: the color of samples sintered at a) air and b) H_2, respectively; the results of c) oxide-ion conductivity and d) oxygen permeability evaluated with Air-SZMO and H_2-SZMO; e) the different ratio of Mo ions and the transporting mechanism for electron and oxygen; f) the variation of band length and band angle in MoO_6 and ZnO_6 octahedrons. a–f) Reproduced with permission.[102] Copyright 2023, Elsevier.

Nb (+5), and Ta (+4 and +5). As illustrated in Figure 12a, the schematic depiction of the unit cell structure portrays a simple cubic arrangement. Oxygen atoms reside in the face-centered positions of the cube, forming octahedral coordination with the B-site metal ions. This structural configuration exhibits pronounced symmetry, thereby facilitating expedited electron and ion transport within the bulk phase. Conversely, a reduction in the symmetry of the lattice structure, as observed in orthorhombic or tetragonal perovskite phases, engenders increased transmission distances, consequently impeding the efficient transmission of ions and electrons.[11c]

2) AA'BB'$O_{6-\delta}$: The general composition of double perovskite structure is alternately stacked layers along the c-axis direction in the form of ...|AO|BO2|A'O|BO2|..., with its unit cell structure depicted in Figure 12b. Typically, the A-sites typically accommodate trivalent lanthanide metal ions such as Pr, Nd, Sm, and Gd, whereas the A'-sites commonly host divalent alkaline earth metal ions like Ba and Sr. Transition metal ions, like those found in simple perovskites, predominantly occupy the B-sites within the lattice. Notably, in ordered A-site double perovskite oxides, the larger ionic radius of A' ions tends to stabilize structures with a coordination number of 12, while A-site lanthanide ions (or Y ions) tend toward lower coordination numbers. Consequently, oxygen vacancies are primarily concentrated within the AO layers, and upon heating, a transition from ordered to disordered for oxygen vacancy occurs,[106] thereby accelerating the rapid anisotropic migration of oxygen ions across the ab plane. Furthermore, recent

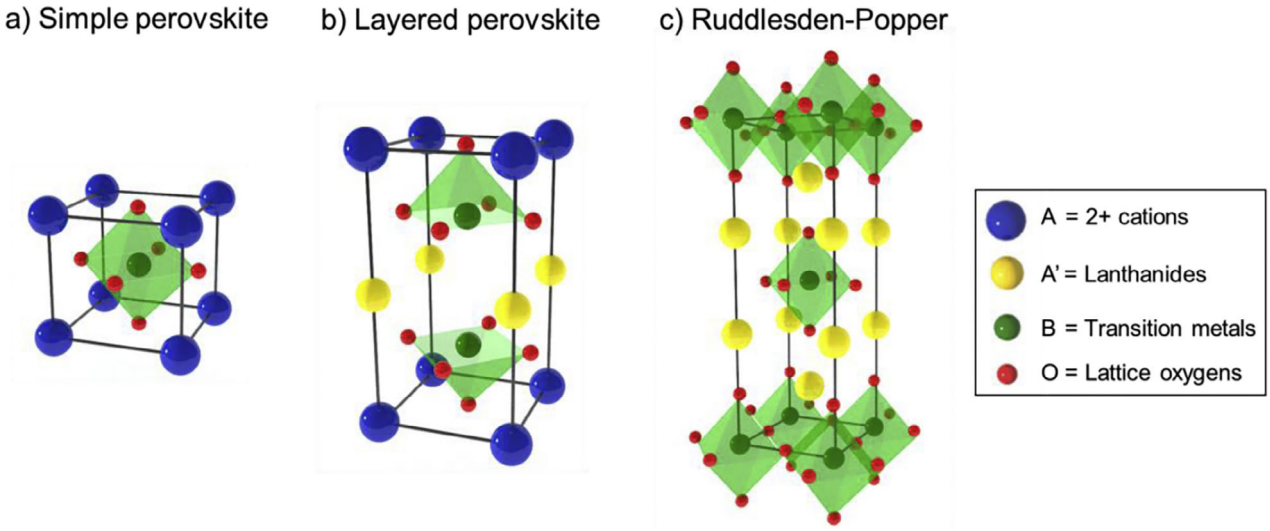

Figure 12. Typical perovskite oxide phase structures of air electrodes: a) simple perovskite; b) double perovskite; c) Ruddlesden–Popper perovskite. a–c) Reproduced with permission.[18] Copyright 2019, Elsevier.

investigations suggest that the ordered arrangement of A-site cations in double perovskites can preserve higher concentrations of oxygen vacancies while enhancing their basicity,[78] thereby positively impacting the hydration of protons in electrode reactions.

3) $A_{n+1}B_nO_{3n+1+\delta}$: For R-P type perovskite oxides, they were first synthesized and named by S.N. Ruddlesden and P. Popper in 1957. Specifically, the types of metal ions occupying the A and B sites of this structure are similar to those in single perovskite-type oxides. It can be conceptualized as comprising alternating layers of perovskite structure layers (ABO_3) and rock salt layers (AO) along the c-axis with the general formula $A_{n+1}B_nO3_{n+1-\delta}$, where 'n' represents the number of octahedral layers in the perovskite-like stack. Notably, the simplest structure is $A_2BO_{4+\delta}$, as depicted in Figure 12c, wherein the lattice is constructed using ABO_3 perovskite layers sandwiched between AO rock salt layers. Besides, the mixed ion-electron conductivity mainly arises from the migration of interstitial oxygen ions in the AO layer and the p-type electronic conduction of the ABO_3 layer.[107] Furthermore, higher-order R-P perovskites contain more BO_6 corner-sharing octahedra, providing additional conduction pathways and potentially exhibiting higher electronic conductivity compared to low-order R-P materials.[108]

In general, these three types of oxide materials can be modified in terms of their type, composition, preparation methods, and phase structure through appropriate strategies to achieve enhanced triple conductivity for electrons, oxygen ions, and protons, as well as improved surface properties. This enhancement significantly improves their catalytic activity for ORR and OER, as well as their long-term operational stability.

4.1.1. Single Perovskite Phase

In the early development of R-PCECs technology, the traditional R-SOCs air electrode materials (MIEC), including $La_{0.8}Sr_{0.2}CoO_{3-\delta}$ (LSC), $Sm_{0.5}Sr_{0.5}CoO_{3-\delta}$ (SSC), $La_{0.6}Sr_{0.4}Co_{0.2}Fe_{0.8}O_{3-\delta}$ (LSCF), and $Ba_{0.5}Sr_{0.5}Co_{0.8}Fe_{0.2}O_{3-\delta}$ (BSCF), were investigated as the initial air electrode candidates due to the excellent oxygen ion and electron conductivity characteristics. However, Han et al. confirmed that the systems of $La_{1-x}Sr_xCo_{1-y}Fe_yO_{3-\delta}$ (x = 0.1-0.7, y = 0–1) and $Ba_{0.5}Sr_{0.5}Co_{1-y}Fe_yO_{3-\delta}$ (y = 0.2-0.8) were difficult to hydrate, and the C_H value was not higher than 0.002 mol unit^{-1} at 600 °C.[109] This intrinsic limitation in proton conductivity hampers the kinetics of electrode reactions, thus resulting in relatively low overall electrochemical performance of R-PCECs. Consequently, extensive endeavors have been directed towards enhancing the proton conductivity of the conventional air electrodes to foster hydration/protonation.

In 2014, Poetzsch et al. found that $Ba_{0.5}Sr_{0.5}Fe_{0.8}Zn_{0.2}O_{3-\delta}$ (BSFZ), which can be construed as a strategic substitution of Zn for Co within the BSCF material system, was a mixed triple – electron, O^{2-}, and H^+ conductor.[110] The hydration property of this electrode material was experimentally corroborated through characteristic mass relaxation signals observed upon reversible alterations in pH_2O levels within the testing environment maintained at 400 °C (**Figure 13a**). However, despite these advancements, under identical testing conditions, the concentration of protonic charge carriers remained notably lower by 1–2 orders of magnitude compared to the concentration of oxygen vacancies and hole charge carriers, as depicted in Figure 13b. Subsequently, the enhancing effect of zinc ions on proton conductivity was confirmed within the perovskite family (Ba, Sr, La)(Fe, Co, Zn, Y)$O_{3-\delta}$.[80a] This enhancement primarily arises from the significant elevation of oxygen vacancy concentration, the presence of a redox-inactive cation, potential local lattice distortions, and the reduced electronegativity associated with Zn^{2+}. For comparison, the incorporation of Co ions at the B-site is observed to detrimentally influence proton absorption due to the diminished basicity of oxygen ions resulting from the strong covalent nature of Co-O chemical bonds, as shown in Figure 13c. Moreover, this study also suggests that A-site Ba

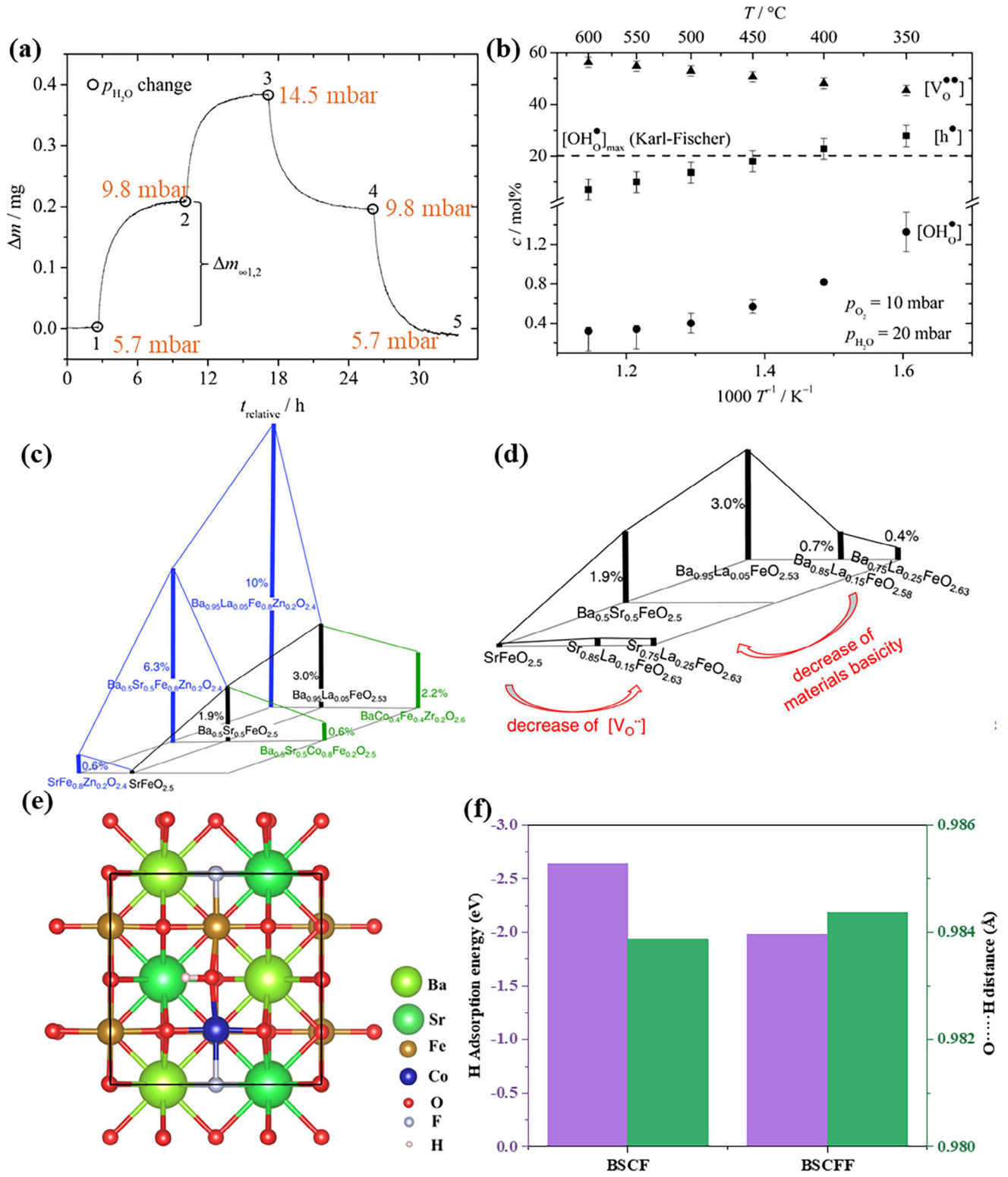

Figure 13. a) Exemplary mass relaxation curves at 400 °C; b) defect concentrations (% per BSFZ formula unit); c) effect of Zn and Co substitution on the B-site; d) variation of La and Sr content on the perovskite's A-site; e) schematic illustration of H^+ on Fe-O-Co in BSCFF cell; f) comparison of O···H formation energy and distance for BSCF(F) samples. a,b) Reproduced with permission.[110b] Copyright 2014, Royal Society of Chemistry. c,d) Reproduced with permission.[80a] Copyright 2018, Wiley. e,f) Reproduced with permission.[112] Copyright 2023, Elsevier.

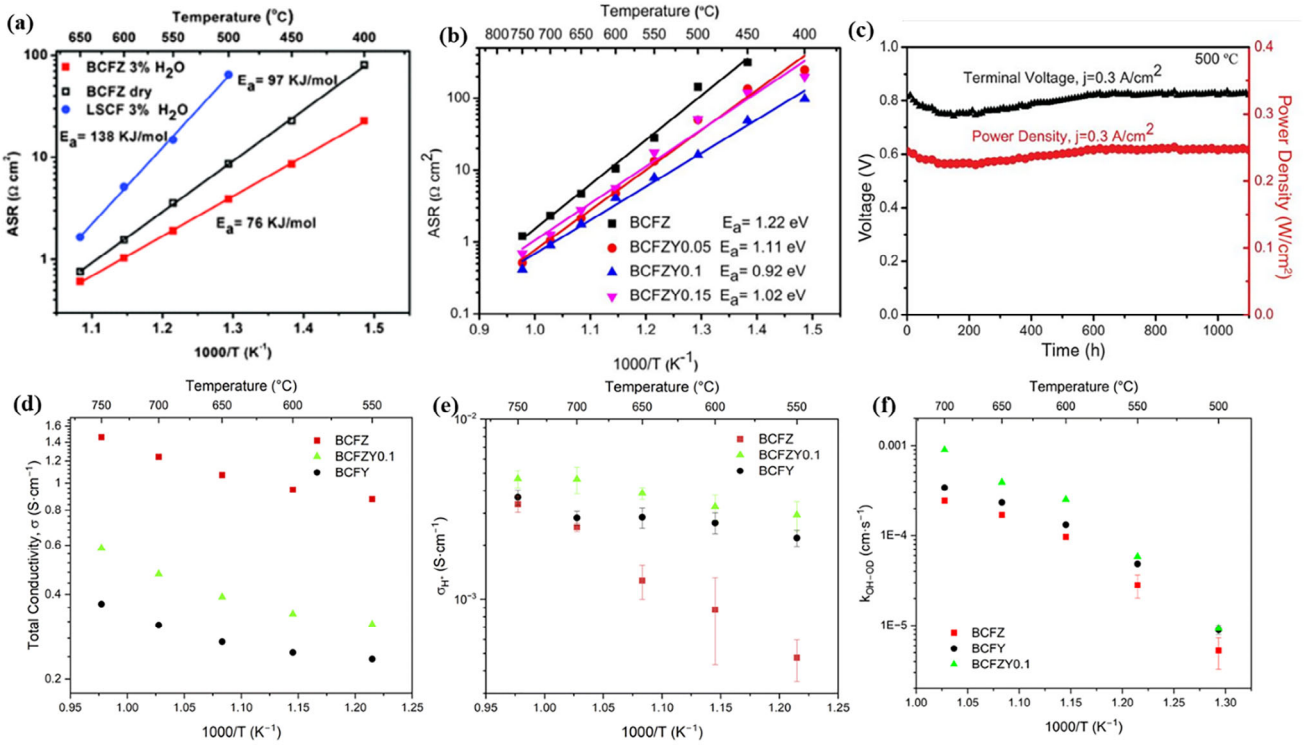

Figure 14. a) The ASR values for BCFZ and LSCF samples in dry and wet air; b) the ASR values for BCFZYx samples; c) terminal voltage and power density at a current density of 0.3 A cm^{-2} at 500 °C for BCFZY over 1100 h; d) the total conductivity (in 5%H_2/95%N_2) and e) proton conductivity (hydrogen permeation flux) for $BCFZY_x$ samples; f) fitting $k_{OH\text{-}OD}$ values for $BCFZY_x$ at 500–700 °C. a) Reproduced with permission.[114] Copyright 2013, Royal Society of Chemistry. b,c) Reproduced with permission[115] Copyright 2015, The American Association for the Advancement of Science. d–f) Reproduced from ref. [116] with permission from the Royal Society of Chemistry.

ions are more conducive to proton absorption compared to other ions (Sr, La), owing to the lower electronegativity (Figure 13d). Ultimately, the $Ba_{0.95}La_{0.05}Fe_{0.8}Zn_{0.2}O_{3-\delta}$ material exhibits the highest proton concentration, measured at 0.1 mol $unit^{-1}$ at 250°C.

In addition to substituting metal ions at the A and B sites of simple perovskite phases to enhance the triple conductivity of air electrodes, the substitution at appropriate O sites has also been demonstrated as an effective strategy. Xia et al. successfully synthesized F^--doped $Ba_{0.5}Sr_{0.5}Co_{0.8}Fe_{0.2}O_{3-\delta}$ (F-BSCF) air electrodes,[111] revealing improved catalytic performance attributed to the presence of more oxygen-active species and faster oxygen ion transport pathways. Furthermore, this type of air electrode can mitigate the diffusion of halogens, a common issue with F-doped electrolyte materials, under operating conditions (from electrolyte to air electrode), thereby exhibiting enhanced long-term stability. Ni et al. introduced different anions (F^-, Cl^-) into the lattice oxygen sites of BSCF air electrodes through a simple anion engineering approach,[112] resulting in accelerated electrode reaction kinetics. It is noteworthy that due to the distinct physicochemical properties of anions (ionic radius, electronegativity), F-doped BSCF air electrodes demonstrate the most robust catalytic performance for ORR/OER. Experimental and theoretical calculations reveal that this enhancement primarily stems from the significantly improved surface generation and bulk-phase transport processes of oxygen ions and protons, as illustrated in Figure 13e,f.

Furthermore, Tong et al. discovered that Zr-doped $BaCo_{0.4}Fe_{0.6}O_{3-\delta}$ perovskite oxide ($BaCo_{0.4}Fe_{0.4}Zr_{0.2}O_{3-\delta}$, BCFZ) serves as highly stable and active oxygen permeation membranes due to their elevated mixed oxygen ion and electron conductivity, coupled with outstanding chemical and structural stability.[113] More importantly, this material exhibits stronger hydration capabilities compared to traditional LSCF, as evidenced by the reduced area-specific resistance (ASR) values upon introducing water vapor (**Figure 14a**).[114] Consequently, when directly employed as air electrodes in proton-conducting fuel cells, BCFZ yielded significantly higher electrochemical performance compared to traditional MIEC electrodes. Subsequently, aiming to further enhance its proton conductivity, considering the lower valence state of Y^{3+} compared to Zr^{4+}, Duan et al. partially substituted Y^{3+} for Zr^{4+} in BCFZ and designed a new class of air electrode, $BaCo_{0.4}Fe_{0.4}Zr_{0.2-x}Y_xO_{3-\delta}$ ($BCFZY_x$) (Figure 14b). Among the compositions investigated, $BaCo_{0.4}Fe_{0.4}Zr_{0.1}Y_{0.1}O_{3-\delta}$ (BCFZY) exhibited the lowest ASR value and activation energy at a temperature down to 500 °C, as well as an exceptional durability over 1100 h (Figure 14c).[115] Moreover, the bulk proton conductivity and surface kinetics of these materials were systematically investigated through hydrogen permeation and electrical conductivity relaxation (ECR) measurements. Through three different types of conductivity relaxation measurements, including oxidation, hydration, and isotope exchange, it was observed that Y doping significantly improved proton dynamics under humidified oxidation conditions. The 10% Y-doped

BCFZY oxide exhibited the highest proton conductivity (0.0032 S cm^{-1} at 600 °C) (Figure 14e) approximately four times that of the parent material BCFZ, while further incorporation of Y slightly decreases conductivity (Figure 14d).[116] Furthermore, its proton surface kinetics were significantly accelerated, as evidenced by the $k_{OH\text{-}OD,chem}$ values obtained from an ECR experiment by switching atmospheric conditions from H_2O to D_2O ((Figure 14f)). Since then, BCFZY is regarded as a representative single perovskite phase air electrode with triple conductivity capabilities, and extensive research based on it has been conducted.

To further fine-tune the triple-conducting properties, an A-site deficiency strategy was employed to fabricate new perovskite oxides, $Ba_xCo_{0.4}Fe_{0.4}Zr_{0.1}Y_{0.1}O_{3-\delta}$ (x = 1, 0.95, 0.9).[70a] As a result of the higher concentration of oxygen vacancies and the enhanced oxygen-ion bulk diffusion and proton hydration kinetics, $Ba_{0.9}Co_{0.4}Fe_{0.4}Zr_{0.1}Y_{0.1}O_{3-\delta}$ exhibited the lowest ASR value (0.52 Ω cm^2) at 500 °C. Moreover, the noticeable weight gain peak (0.11% of weight) observed in the thermogravimetric relaxation curves further indicated the enhanced generation ability of hydroxide defects for $B_{0.9}$CFZY compared to the stoichiometric composition sample (0.07%). Furthermore, Shao et al. employed B-site doping to enhance the triple conductivity of BCFZY, synthesizing a series of air electrode materials, $Ba(Co_{0.4}Fe_{0.4}Zr_{0.1}Y_{0.1})_{0.95}M_{0.05}O_{3-\delta}$ (M = Ni, Mn, Zn, Cu).[117] Based on ECR experiments and oxygen and hydrogen permeation tests, it was demonstrated that Ni-doped BCFZY ($Ba(Co_{0.4}Fe_{0.4}Zr_{0.1}Y_{0.1})_{0.95}Ni_{0.05}O_{3-\delta}$) air electrodes exhibited enhanced oxygen ion and proton transport characteristics and surface exchange kinetics, thereby displaying enhanced ORR activity, with the ASR value decreased from 1.75 to 1.50 Ω cm^2 at 550 °C. In addition, partial doping of the BCFZY parent lattice with lower valence state Mg^{2+} ($Ba(Co_{0.4}Fe_{0.4}Zr_{0.1}Y_{0.1})_{0.95}Mg_{0.05}O_{3-\delta}$) and Zn^{2+} ($BaCo_{0.4}Fe_{0.4}Zr_{0.1}Y_{0.1-x}Zn_xO_{3-\delta}$) was also demonstrated to effectively to improve its triple conductivity characteristics.[118] Interestingly, despite the lower electron conductivity of BCFZY and its modified samples, which varies from 1 to 2 S cm^{-1} at 600 °C, their electrochemical performance is varied. This implies that air electrodes may not necessarily require a very high hole conductivity, but rather, achieve a balance between ion and hole conductivity and catalytic activity is more meaningful.

4.1.2. Double Perovskite Phase

The cation-ordered double-perovskite structures have gained significant attention owing to their facilitated oxygen ion diffusion, accelerated surface oxygen exchange, and enhanced electrical conductivity at lower temperatures.[119] In addition, as indicated by Grimaud et al.,[120] these layered perovskite materials demonstrated higher proton conductivities to some extent. Therefore, layered perovskites are promising candidate materials for air electrodes in R-PCECs.

Currently, the most commonly used double-perovskite air electrode for R-PCECs is $PrBa_{0.5}Sr_{0.5}Co_{1.5}Fe_{0.5}O_{5+\delta}$ (PBSCF), originating from the triple-conducting $NdBa_{0.5}Sr_{0.5}Co_{1.5}Fe_{0.5}O_{5+\delta}$ (NdBCSF) layered oxide reported by Kim in 2014.[121] The PBSCF air electrode was developed as an air electrode since the Pr analog offers higher electronic conductivity than Nd in the layered perovskite structure.[106] Moreover, the PBSCF exhibited excellent ORR/OER catalytic performance when it was exposed in steam atmosphere. For instance, the R-PCEC fabricated by Haile et al. achieved a current density of ≈0.65 A cm^{-2} at 0.7 V in FC mode and ≈-0.70 A cm^{-2} at 1.3 V in EC mode with an excellent reversibility over 50 h (**Figure 15a**).[122] This outstanding performance may be due to the suitable chemical compatibility with the electrolyte and the special H_2O uptake characteristics for PBSCF. As shown in Figure 15b.,[123] the C_H values determined by the difference H_2O uptake thermogravimetric profiles on cooling in dry and wet air ranges from 3.5 mol% at 200 °C to 1.7 mol% at 600 °C, which is much higher than that of BCFZ (0.5 mol% at 400 °C) and BCFZn (1.5 mol% at 350 °C). The higher proton concentration observed in PBSCF can be ascribed to its lower hydration entropy of -63 J mol^{-1} K^{-1} compared to -103 ± 5 J mol^{-1} K^{-1} in BCFZ and -140 ± 30 J mol^{-1} K^{-1} in BCFZn, respectively (Figure 15c), enabling PBSCF to maintain elevated proton levels under high-temperature conditions. Specifically, the proton solubility for the PBSCF was directly observed through dynamic secondary ion mass spectrometry and time-of-flight secondary ion mass spectrometry.[124] The depth profile (≈3.5 µm) and 3D map (50 × 50 × 1 µm3) of ^{2}D element for PBSCF bulk in D_2O-humidified air confirmed that the protons were spatially uniformly distributed without any segregation in a specific region such as grain boundary (Figure 15d). From the returned relativity precise values of α determined by the conductivity change (Figure 15e), it is confirmed that the proton uptake in PBSCF mostly occurs by the hydration reaction at 400–700°C. Despite the proton uptake mechanism, the migration kinetics of these protonic defects during hydration/dehydration is also investigated by employing the isotope exchange diffusion profile (IEDP) method,[125] in which deuterium is used as a tracking indicator of proton diffusion via time-of-flight secondary ion mass spectrometry (ToF-SIMS), as shown in Figure 15f. The surface exchange coefficient (k^*_H) and diffusion coefficient (D^*_H) of protons were 2.60 × 10^{-7} cm s^{-1} and 1.04 × 10^{-6} cm^2 s^{-1} at 550 °C (Figure 15g), respectively, much higher than most reported air electrodes (Figure 15h).[125] These results robustly confirmed the excellent triple-conducting properties of PBSCF family materials, which offer promising air electrode candidates. Moreover, reducing the high TEC caused by the higher Co concentration,[126] as well as minimizing the segregation of undesired elements and heterophase formation due to the high basicity of Ba and Sr in CO_2 or H_2O-containing atmospheres,[127] would improve its practical applicability.

4.1.3. R-P Perovskite Phase

Recently, there has been a growing interest in utilizing R-P type perovskite oxides as air electrodes for R-PCECs. The distinctive lattice arrangement of these materials, characterized by consecutive layers resembling perovskite structures comprised of corner-sharing BO_6 octahedra nestled between two layers of rock-salt, facilitates the existence of at least two distinct chemical environments within a two-dimensional layered framework, namely the perovskite slab and the rock-salt slab. This architectural arrangement facilitates anisotropic transport of charge carriers,

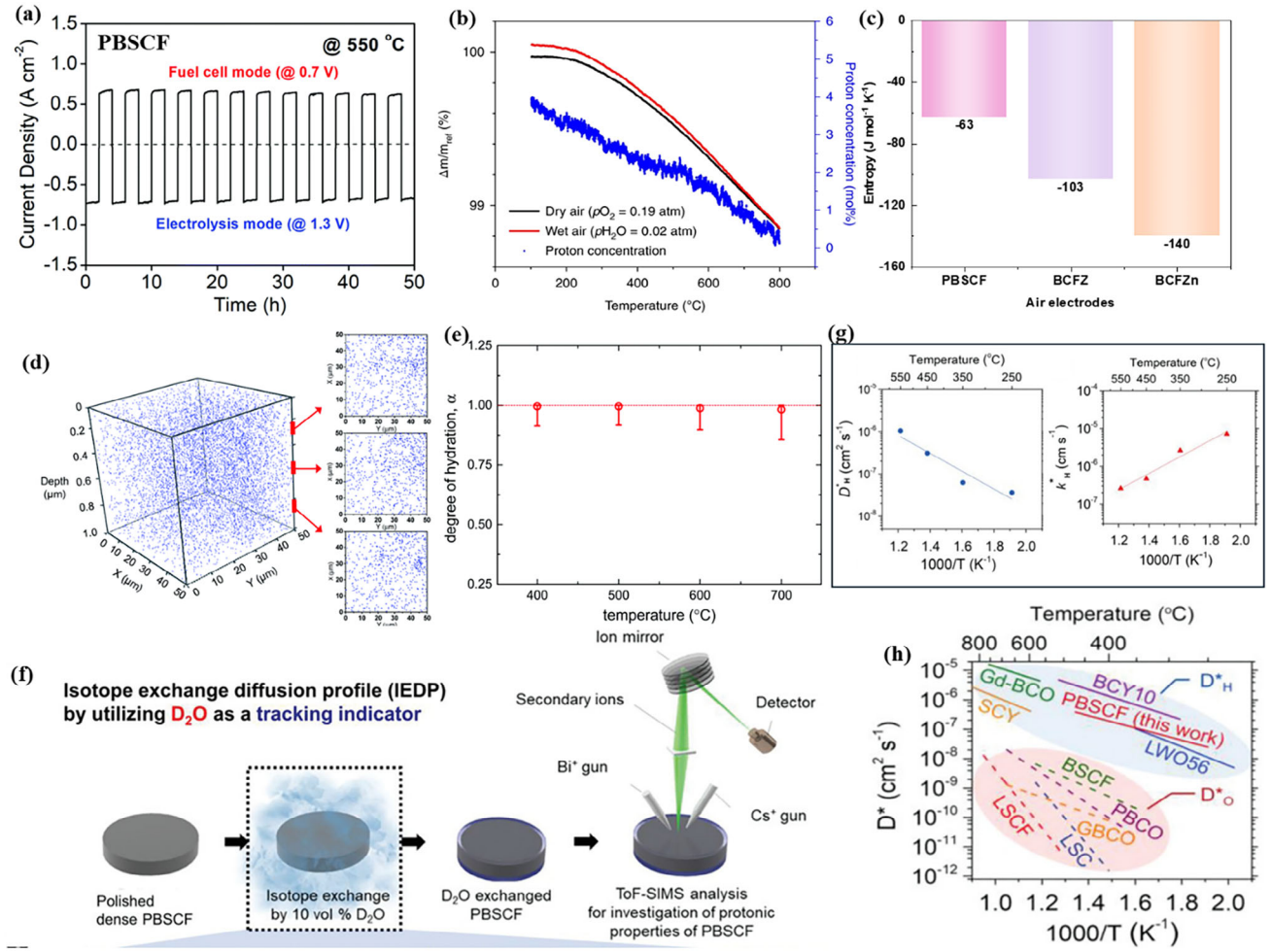

Figure 15. a) Cyclic operation modes for PBSCF at 550 °C; b) thermogravimetric profiles on cooling in dry and wet air and implied proton concentration; c) summarized entropy values for different air electrodes; d) 3D map of ^{2}D distribution; e) the degree of hydration, α, from the conductivity difference; f) schematic illustration of preparation and incorporation of D_2O for the ToF-SIMS measurement; g) the diffusion and surface kinetics coefficient of proton (D^*_H and k^*_H) values for PBSCF; h) comparison of D^*_H with different materials. a) Reproduced with permission.[122] Copyright 2019, Royal Society of Chemistry. b,c) Reproduced with permission.[123] Copyright 2018, Springer Nature. d,e) Reproduced with permission.[124] Copyroght 2022, Royal Society of Chemistry. f–h) Reproduced with permission.[125] Copyright 2021, Wiley.

including O^{2-} and proton defects.[128] Such transport dynamics differ significantly from the migration mechanism observed in conventional perovskite oxides, wherein oxide ions transport pathways connecting oxygen vacancies. In R-P perovskite oxides, particularly those featuring an excess of oxygen (as commonly encountered in the n = 1 referred as K_2NiF_4 structure), interstitial oxide ions within the rock-salt layers[107a,108] facilitate rapid and anisotropic conduction of oxide ions through a push-pull mechanism within the rock-salt layers. Such enhanced ion transport dynamics hold the potential to accelerate electrochemical processes, such as ORR/OER, at lower operating temperatures.

Initially, the excellent hydration and protonic defects transport ability were demonstrated in the $Pr_{2-x}Sr_xNiO_{4+\delta}$ ($x \leq 0.50$) oxides with the K_2NiF_4 structure (**Figure 16**a,b).[129] Considering the potential detrimental effects of Sr^{2+} incorporation on hydratable characteristics and the overall stability of the material, $Pr_2NiO_{4+\delta}$ has been selected for utilization as the air electrode, showcasing commendable chemical stability and outstanding electrochemical performance (0.06 Ω·cm^2 and 0.82 W·cm^{-2} at 650 °C).[130] Furthermore, in the $Ln_{1.2}Sr_{0.8}NiO_{4+\delta}$ (Ln = La, Pr) system, different A-site cations also affect the catalytic activity of the air electrode reaction. Specifically, compared to $Pr_{1.2}Sr_{0.8}NiO_{4+\delta}$, $La_{1.2}Sr_{0.8}NiO_{4+\delta}$ exhibits higher electrochemical performance in both FC and EC modes.[131] This difference is likely attributed to the lower electronegativity of La^{3+} compared to Pr^{3+} and the different oxygen chemical environment due to the difference for La and Pr-based R-P oxides, which may adversely affect proton/oxygen absorption and transport capabilities.[130] Besides, the introduction of Fe ions into B-site can further enhance its catalytic performance, as evidenced by $La_{1.2}Sr_{0.8}Ni_{0.6}Fe_{0.4}O_{4+\delta}$.[132]

Furthermore, the layered architecture inherent to R-P-type oxides imparts unique cation coordination environments and distinct manifestations of anion defects.[133] Modulating the number of layers, denoted as 'n', imparts changes to the dimensional characteristics of the layered structure, thereby

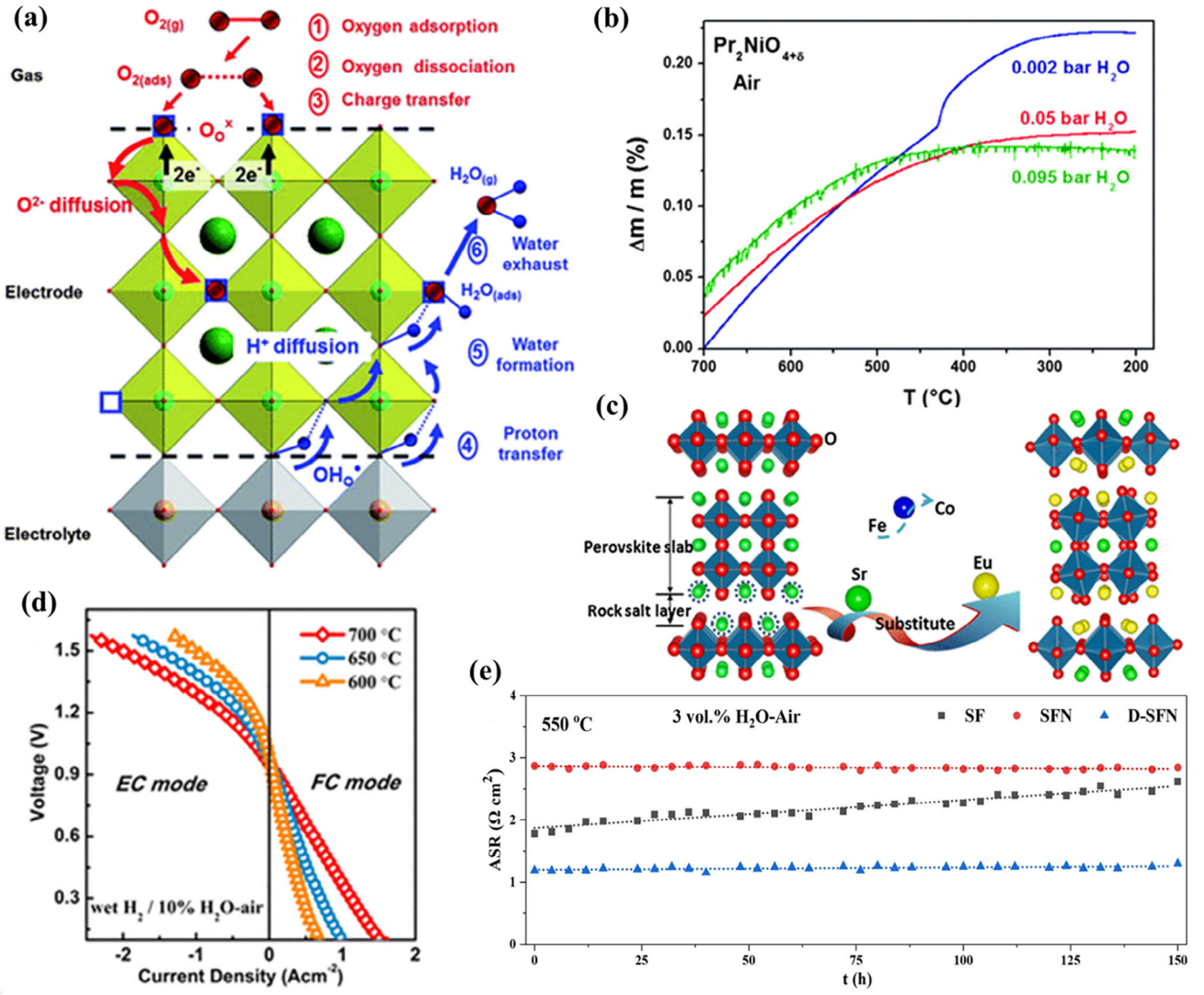

Figure 16. a) Schematic representation of the oxygen reduction and formation of water for TCO; b) weight change measured at decreasing temperature for $Pr_2NiO_{4+\delta}$ under air containing 0.002 up to 0.095 bar H_2O; c) design sketch from R-P-SF to SEFC; d) electrochemical performance for SEFC air electrode; e) ASR values for SF, SFN, and D-SFN air electrodes. a,b) Reproduced with permission.[129] from the Royal Society of Chemistry. c,d) Reproduced with permission.[86a] Copyright 2018, American Chemical Society. e) Reproduced with permission.[138] Copyright (2024), Springer Nature.

expanding the chemical diversity within the realm of R-P perovskites. Consequently, variations in stoichiometry are observed. For instance, low n-value R-P oxides tend to exhibit a prevalence of interstitial oxygen over oxygen vacancies, while high-order R-P oxides typically manifest oxygen-deficient configurations. Specifically, oxygen vacancies are localized within the perovskite layers (A'O), while interstitial oxygen is situated within the rock-salt layers (AO).[107a] The different oxygen contents affect crystal symmetry and oxidation states of B-site transition metal ions within the bulk lattice, thereby shaping the pathways for ion transport. Experimental investigations and theoretical analyses corroborate the notion that higher-order R-P oxides exhibit enhanced facilitation of oxygen ion and proton transport within the lattice structure.[134] Moreover, they demonstrate heightened chemical and thermal stability, attributes conducive to augmenting catalytic performance of air electrodes.[134,135]

A novel double-layer R-P oxides with the composition of $Pr_2BaNiMnO_{7-\delta}$ (PBNM) was reported as a preeminent, highly active low-temperature air electrode.[135a] In the selected $Pr_3Ni_2O_7$ system, simultaneous introduction of Ba^{2+} into the A-site and Mn^{3+}/Mn^{4+} into the B-site serves to enhance both stability (owing to the greater propensity of Ba ions for 12-coordination with oxygen) and catalytic performance (facilitated by the octahedral distortion induced by Mn ions in BO_6 to promote ion transport). Moreover, the tetragonal PBNM phase with I4/mmm space group symmetry exhibits exceptional chemical compatibility and performance, as evidenced by its notably low TEC (10.35×10^{-6} K^{-1}) and ASR (0.084 Ω cm^2 at 700 °C) value. Moreover, significant water intercalation, alongside potential proton defects, has also been identified in the double-layered R-P $Sr_3Fe_2O_{7-\delta}$ (R-P-SF), resulting in the formation of hydrated derivatives under humid conditions.[136] In response, Lu et al. pioneered its utilization

as an air electrode, substantiating its proficiency as an effective oxygen ion-electronic conductor in dry atmospheres through EIS results. Furthermore, employing first-principal calculations, R-P-SF was found to possess a low proton formation energy (≈−0.23 eV) and a low proton migration energy (≈0.62 eV) in humid atmospheres.[137] However, R-P-SF exhibits chemical instability in atmospheres involving Lewis acids (steam/CO_2) due to the high basicity of Sr. Consequently, the introduction of the lanthanide element Eu in partial replacement of Sr in the A-site of R-P-SF was proposed to mitigate this basicity at the cost of oxygen vacancies. To address this vacancy, Co was partially substituted for Fe, yielding $SrEu_2Fe_{1.8}Co_{0.2}O_{7-\delta}$ (SEFC), as illustrated in Figure 16c,d.[86a] By employing the SEFC air electrode, the R-PCEC button demonstrated smooth transitioning between FC and EC modes without any discernible degradation over a 135-hour long-term test.

Recently, Ni et al. devised a method involving the concurrent introduction of A-site deficiency and partial Nb-substitution to synthesize $Sr_{2.8}Fe_{1.8}Nb_{0.2}O_{7-\delta}$ (D-SFN).[138] This approach effectively restrained the formation of the secondary phase $Sr_3Fe_2(OH)_{12}$, thus stabilizing the lattice structure. In addition, partial Sr defects were intentionally introduced to elevate the concentration of oxygen vacancies. The resulting D-SFN air electrode exhibited markedly heightened electrocatalytic activity and stability (Figure 16e), demonstrating remarkable resilience under both FC and EC modes, including their switching mode.

Three-layered R-P oxides also serve as promising candidates for R-PCEC air electrodes. For instance, a novel single-phase air electrode, $Sr_3EuFe_{3-x}Co_xO_{10-\delta}$ (3-SEFCx, x = 0.0, 0.5, 1.0, 1.5), was synthesized through a co-doping approach involving Eu and Co (similar to the SEFC air electrode).[30c] This electrode demonstrated higher oxygen non-stoichiometry and favorable structural thermal stability. This active and stable single-phase air electrode exhibited lower polarization resistances and relatively improved peak power densities compared to the double-layered SEFC air electrode, which was ≈0.030 Ω cm^2 and 900 mW cm^{-2} at 700 °C, respectively.

The tunability afforded by the composition and structure of R-P perovskites engenders unique electronic configurations and an array of captivating physicochemical properties unattainable by traditional perovskite compounds or many other crystalline metal compounds. Thus, this presents promising avenues for the strategic design of electrocatalysts based on the distinct chemical, structural, and electronic attributes inherent to R-P perovskites.

Furthermore, some single-phase air electrodes designed for proton-conducting electrolytes, such as Zn (or Ce/Y) doped BSCF, PBSCF-based, and BCFZY, are also applicable to oxygen-ion-conducting solid oxide fuel cells.[139] This is primarily attributed to their outstanding oxygen-ion conductivity and superior compatibility with conventional oxygen-ion-conducting electrolytes, such as yttria-stabilized zirconia (YSZ) and gadolinium-doped ceria (GDC).

4.2. Composite Air Electrode

Due to the challenges posed by homogeneous oxides, achieving a balance in triple-conducting properties can be difficult. For instance, most high-performance MIECs often exhibit proton blocking and limited proton absorption and transport capabilities. Furthermore, excellent proton conductor electrolyte phases may lack sufficient electronic/oxygen ion transport capabilities. Consequently, there is a need to fabricate composite electrodes with coexisting phases possessing different functionalities to simultaneously achieve excellent conduction of oxygen ions, electrons, and protons.

4.2.1. Mechanical Mixing

Mechanical mixing is a physical technique that is commonly employed for the preparation of triple-conducting composite electrodes due to its cost-effectiveness and simplicity. This method involves minimal alteration to the sample composition while allowing for particle size reduction to the nanoscale. This reduction is achieved by controlling parameters such as milling speed, dwell time, ball-to-powder ratio, and milling media, ensuring thorough grinding of bulk samples (**Figure 17a**).

In the early stage, the composite air electrode was commonly fabricated by mixing a MIEC and a protonic conductor via mechanical milling. Compared with single-phase air electrodes, the use of proton-conducting composite electrodes can effectively expand the reaction sites to the entire air electrode surface, greatly accelerate the charge transfer process, and more importantly, improve the thermal matching with the electrolyte (Figure 17b). One of the early composite electrodes reported was $Sm_{0.5}Sr_{0.5}CoO_{3-\delta}$ (SSC) mixed with a proton conductor of $BaCe_{0.8}Sm_{0.2}O_{3-\delta}$ (BCS20).[140] When the composite ratio of SSC reaches 60%, its ASR reaches the lowest (0.21 Ω cm^2 at 700°C). In addition, SSC was also used to mix with some other proton-conducting phases, such as $BaCe_{0.5}Zr_{0.3}Y_{0.16}Zn_{0.04}O_{3-\delta}$,[141] $BaZr_{0.8}Y_{0.2}O_{3-\delta}$ (BZY20)[142] and $BaZr_{0.1}Ce_{0.7}Y_{0.2}O_{3-\delta}$.[143] A similar trend was observed in $Ca_{0.3}Y_{0.7}Fe_{0.5}Co_{0.5}O_{3-\delta}$-$BaZr_{0.1}Ce_{0.7}Y_{0.2}O_3$ (CFYC-BZCY)[144] composite air electrode (Figure 17c,d). As a result, the enhanced electrochemical performance varies from 277 to 445 mW cm^{-2} at 600 °C due to the different proton conductors and mixing ratios. As another classic MIEC, $La_xSr_{1-x}Co_yFe_{1-y}O_{3-\delta}$ family oxides have also been widely utilized as the primary phases of proton-conducting composite air electrode, such as $La_{0.6}Sr_{0.4}Co_{0.2}Fe_{0.8}O_{3-\delta}$ (LSCF) – $BaCe_{0.9}Yb_{0.1}O_{3-\delta}$ (10YbBC),[145] LSCF – $BaCe_{0.9}Y_{0.1}O_{3-\delta}$,[146] LSCF-$Ba(Zr_{0.1}Ce_{0.7}Y_{0.2})O_{3-\delta}$ (BZCY),[147] and $La_{0.6}Sr_{0.4}Co_xFe_{1-x}O_{3-\delta}$ – $BaZr_{0.8}Yb_{0.2}O_{3-\delta}$ (BZYb).[148] These air electrodes exhibit enhanced electrode catalytic performance compared to single-phase MIEC electrodes due to the additional proton conductor. Besides, the most popular MIEC air electrode, $Ba_{0.5}Sr_{0.5}Co_{0.8}Fe_{0.2}O_{3-\delta}$ (BSCF), is often applied to form composite air electrode due to the excellent oxygen/electron conductivity. Similar to SSC and LSCF oxides, BSCF was used to mix with the proton conductor to enhance the hydration and proton mobility ability, which can be evidenced in BSCF-$BaZr_{0.1}Ce_{0.7}Y_{0.2}O_{3-\delta}$,[149] BSCF-$BaZr_{0.1}Ce_{0.7}Y_{0.1}Yb_{0.1}O_{3-\delta}$ (BZCYYb),[150] BSCF-$BaZr_{0.65}Ce_{0.20}Y_{0.15}O_3$.[151] In addition to the typical single perovskite oxides, the double and R-P perovskite oxides and their novel derives were also used to fabricate composite air electrode via ball mixing, such as $PrBa_{0.9}Ca_{0.1}Co_{2-x}Zn_xO_{5+\delta}$ ($x \leq 0.2$) – BZCYYb,[152] $Nd(Ba_{0.4}Sr_{0.4}Ca_{0.2})Co_{1.6}Fe_{0.4}O_{5+\delta}$ – BZCYYb,[153] $Sr_2Fe_{1.5}Mo_{0.5}O_{6-\delta}$ – $BaZr_{0.1}Ce_{0.7}Y_{0.2}O_{3-\delta}$,[154]

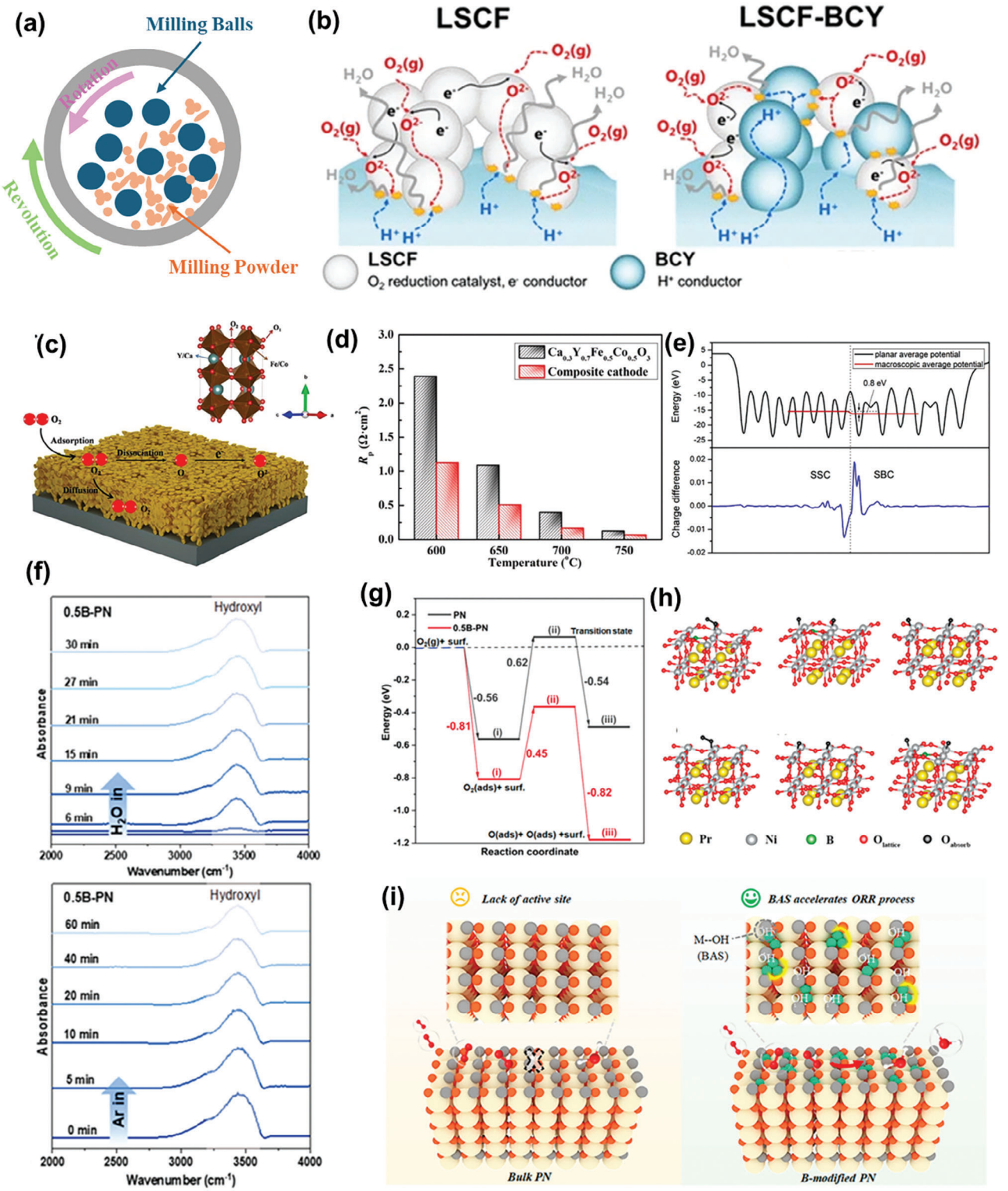

Figure 17. Mechanical mixing: a) a schematic sketch of high energy ball-milling treatment; b) the electrode reaction processes proposed for the LSCF and LSCF-BCY composite air electrode; c) the oxygen diffusion and transfer on CYFC air electrode and d) ASR values for CYFC and CYFC-BZCY; e) macroscopically averaged electrostatic potential curves and planar-averaged charge density difference of SSC-SBC interface; f) in situ DRIFT testing for 0.5B-PN air electrode in wet (top) and dry (bottom) air; g) Gibbs free energy required for the ORR process on PN and 0.5B-PN surfaces and h) the lattice-structures of the intermediates; i) schematic diagram of activation of the PN surface by B. b) Reproduced with permission.[146] Copyright 2024, Springer Nature. c,d) Reproduced with permission.[144] Copyright 2019, Elsevier. e) Reproduced with permission.[157] Copyright 2020, Elsevier. f–i) Reproduced with permission.[159] Copyright 2023, American Chemical Society.

$Pr_2NiO_{4+\delta}$- $BaZr_{0.2}Ce_{0.6}Y_{0.2}O_{3-\delta}$,[155] $La_2Ni_{1-x}Cu_xO_{4+\delta}$ ($x \leq 0.4$) – $BaCe_{0.5}Zr_{0.3}Dy_{0.2}O_{3-\delta}$.[156]

Furthermore, triple-conducting air electrodes can also be synthesized by combining other different perovskite oxides. For example, a composite oxide formed by mechanically mixing SSC and $SmBaCo_2O_{5+\delta}$ (SBC) has demonstrated higher oxygen reduction capabilities and structural robustness.[157] This composite achieves a peak power density of 1.57 W cm^{-2} and ASR of 0.021 Ω cm^2 at 750°C. DFT calculations indicate that upon contact, the SBC surface acquires electrons from the SSC. This interfacial electron transfer and redistribution promote electron-hole separation. As a result, the unstable bonding significantly increases the energy associated with the occupation of π^* orbitals by surface peroxide species originating from the tensile-strained interface (Figure 17e). This enhancement improves both the bulk and surface diffusion rates of oxide ions, thereby accelerating the electrochemical reactions. Additionally, inspired by the observation that isolated boron species in borosilicate form a —B[OH···O(H)—Si]$_2$ structure, which efficiently activates molecular oxygen and propane to promote dehydrogenation, the surface of the air electrode can be modified with boron species to enhance surface proton acidity.[158] By mechanically ball-milling a trace amount of boric acid (0.5 at. %) with $Pr_4Ni_3O_{10+\delta}$ (PN), a 0.5B-PN composite air electrode was successfully prepared (Figure 17f–i).[159] DFT calculations indicated that boron effectively reduces the formation energy of oxygen vacancies. Furthermore, the introduction of boron on the surface significantly enhances the CO_2 tolerance, surface hydration capacity, and Brønsted acid site (BAS, —OH) content of the PN material, thereby boosting the surface ORR kinetics and stability. At 600 °C, the maximum power density of a cell using the 0.5B-PN air electrode was 149.5% higher than that of a cell using the PN air electrode.

These findings emphasize the effectiveness of mechanical mixing as a simple and efficient method for fabricating triple-conducting composite electrodes. By thoroughly blending different materials, the synergistic interactions between phases enhance the electrocatalytic activity. The smaller particle size achieved through mixing also increases the surface area and facilitates better phase integration at the nanoscale. However, the thermodynamic and electrochemical properties of the resulting composite electrodes are highly dependent on the specific physicochemical characteristics of the constituent phases (typically representing oxygen-ion/electron-conducting and proton-conducting phases) and their synergistic blending effects, including phase ratios, interfacial properties, chemical and thermodynamic compatibility, and the grain size of each phase. This is reflected in the varying electrochemical performances and thermal expansion behaviors observed in different composite electrode formulations. Thus, careful selection of phase compositions and proportions, coupled with control of milling parameters such as rates and durations, is imperative to engineer composite electrodes via mechanical mixing, as these critical parameters exert significant influence on the ultimate performance of the composite electrode. Most composites prepared by physical mixing methods also have some disadvantages, such as inhomogeneity, micron-sized phases, high thermal expansion coefficients, undesired phase chemical interactions, and limited contact area of each phase, which will greatly decrease the air electrode reactivity.

4.2.2. Impregnation Engineering

In contrast to conventional mechanical mixing approaches, impregnation entails dispersing nano-catalysts onto a pre-prepared scaffold, which is a simple and effective approach for preparing composite air electrodes. The process involves infiltrating a porous framework with a precursor solution, followed by thermal treatment to convert the precursor into the corresponding phase or composition on the surface. Simultaneously, the morphology of the impregnated coating can be tailored by the interplay of metal ion adhesion within the precursor solution and the capillary forces of the substrate.[160] These surface nanoparticle coatings exhibit efficient catalytic activity and stability, therefore significantly enhancing the surface microstructure of the porous framework through the nano-size effect, which in turn increases its surface area to expand the triple-phase boundary and enhance surface exchange kinetics.[161] Moreover, impregnation coatings can introduce additional nanophases, significantly amplifying the conductivity of frameworks. For instance, impregnating a nano-MIEC into a porous proton-conducting phase electrolyte scaffold or impregnating a proton-conducting phase onto a MIEC scaffold effectively constructs highly efficient and stable triple-conducting composite air electrodes.[162] Lastly, impregnation can introduce stable materials into the electrode, enhancing its long-term stability.[163] Compared to other nanotechnologies, such as chemical vapor deposition and electrospinning, the impregnation method is simpler in terms of process and equipment and requires less active raw material to achieve the same loading.

Infiltrating traditional MIEC materials into proton-conducting phases stands as a prevalent methodology for crafting triple-conducting air electrode. For instance, when $Ba_{0.95}La_{0.05}Fe_{0.8}Zn_{0.2}O_{3-\delta}$ is infiltrated onto a BZCYYb scaffold,[164] the resulting nano-structured active layer, endowed with commendable proton conductivity and electrocatalytic prowess, effectively enlarges the proton-accessible area at the electrode/electrolyte interface, thereby showcasing enhanced ORR kinetics. Another composite air electrode, prepared by impregnating BCFZY into a porous $BaCe_{0.6}Zr_{0.3}Y_{0.1}O_{3-\delta}$ proton conductor carrier (**Figure 18**a,b), also exhibited superior electrochemical performance compared to the single-phase BCFZY electrode, evidenced by the lower ASR value of the assembled symmetrical cell.[115] Considering the superior oxygen ion transport capability of R-P-type perovskites, an R-P oxide $(Pr_{0.9}La_{0.1})_2(Ni_{0.74}Cu_{0.21}Nb_{0.05})O_{4+\delta}$ (PLNCN)-infiltrated $BaZr_{0.1}Ce_{0.7}Y_{0.2}O_{3-\delta}$ air electrode has been developed. Benefiting from the enhanced oxygen surface exchange process, the overall electrode reaction kinetics were accelerated with optimized loading (46.1 wt%).[165]

Similarly, the composite electrode decorated by infiltrating sub-100 nm $Ba_{0.5}Gd_{0.8}La_{0.7}Co_2O_{6-\delta}$ (BGLC) nanocatalysts onto a porous $BaZr_{0.8}Y_{0.2}O_{3-\delta}$ backbone manifests robust OER electrocatalytic activity.[166] Moreover, upon transforming the surface impregnation layer into $LaCoO_3$,[167] the electrocatalytic performance undergoes further enhancement, yielding an ASR value of only 2.18 Ω cm^2 at 500°C, and ensuring sustained operation for 900 hours under a 10% humidity air. The disparities in catalytic performance stemming from the impregnation of diverse nano-coatings primarily depend on discrepancies in the ion or electron conductivity of the coatings, the adhesion between

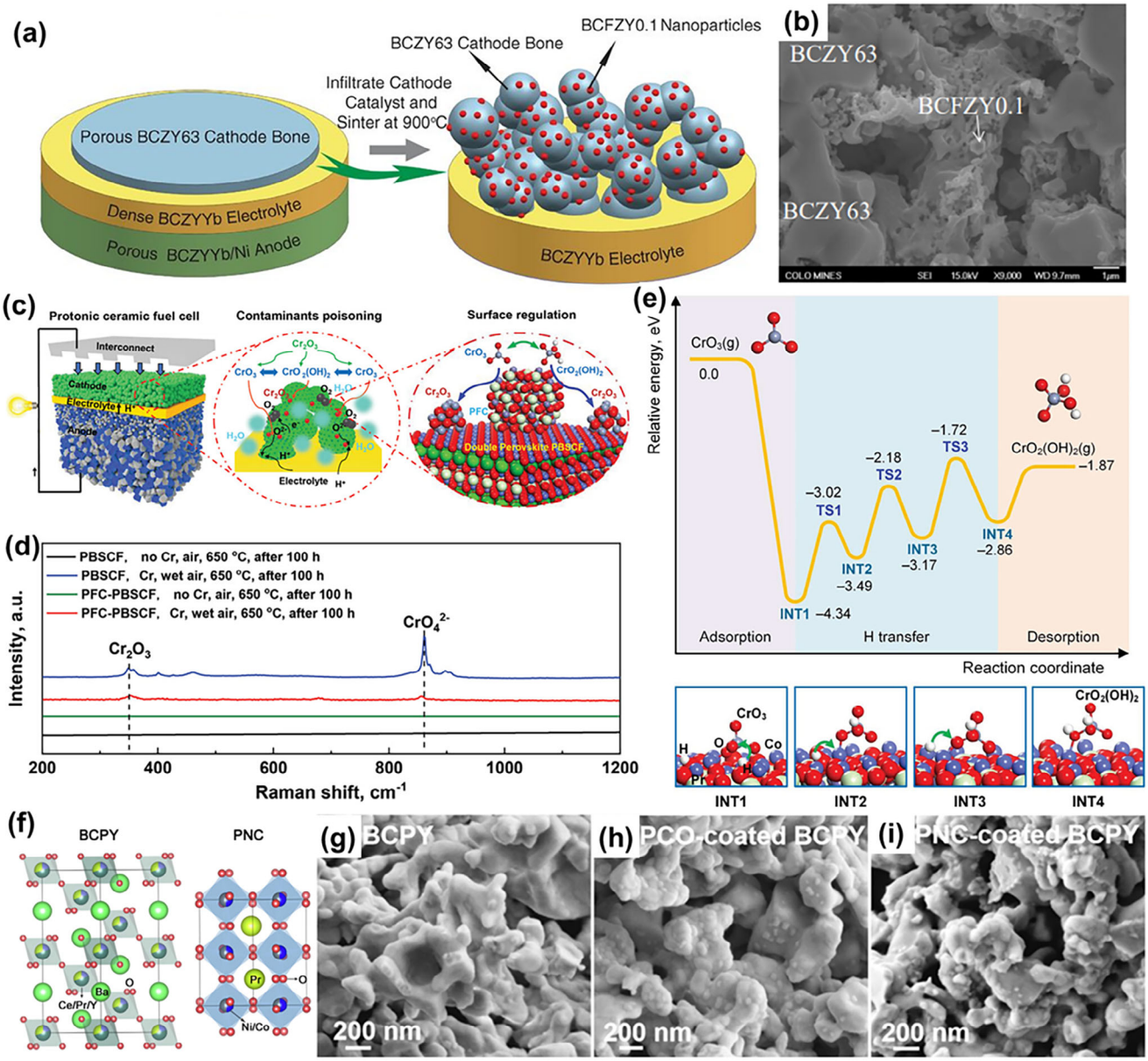

Figure 18. a) Fabrication process of infiltrated air electrode; b) corresponding SEM images of infiltrated composite air electrode; c) schematic illustration of the fuel cell and air electrode in the presence of contaminants (Cr and steam); d) Raman spectra of bare PBSCF and infiltrated PBSCF electrodes after exposure to wet air with direct Cr alloy contact; e) minimum energy pathways of the transformation of CrO_3 to $CrO_2(OH)_2$; f) Crystal structures of parent BCPY and infiltrated PNC; g–i) SEM images of bare and infiltrated electrodes. a,b) Reproduced with permission.[115] Copyright 2015, The American Association for the Advancement of Science. c–e) Reproduced with permission.[172] Copyright 2022, Wiley. f–i) Reproduced with permission.[173] Copyright 2023, Elsevier.

nanoparticles and the scaffold, and variances in the size and dispersion of nanoparticles. This underscores the importance for impregnation methods to select appropriate nano-coatings to facilitate superior design of triple-conducting air electrodes.

Moreover, depositing perovskite nanoparticles onto the surface of mixed oxygen/electron ion conductor frameworks can effectively enhance catalytic activity. By impregnating $BaCoO_{3-\delta}$ (BCO) nanoparticles onto conventional LSCF air electrode surfaces,[168] the kinetics of the surface oxygen exchange process enabled by BCO are further enhanced, leading to notable improvements in the electrochemical performance and durability of BCO-LSCF. DFT calculations have revealed that BCO nanoparticles preferentially deposit by binding with Fe ions on the surface of LSCF (lattice plane: 001), thus utilizing Co ions as active oxygen adsorption centers on LSCF with an energy barrier of -0.81 eV. Furthermore, impregnating $Pr_{0.5}Ba_{0.5}CoO_{3-\delta}$ (decomposes into $Pr_{1-x}Ba_xCoO_{3-\delta}$ and BCO phases) onto the surface of LSCF has also significantly enhanced its ORR/OER catalytic performance.[169]

Perovskite nanoparticle coating can also be used to suppress segregation trend of the A-site elements in the perovskite

oxide backbones. For instance, given the fact that the PBC oxides with favorable ORR/OER catalytic activity often suffer from Ba-enriched surface segregation, leading to faster degradation under high steam-containing atmosphere. A fluorite structure nanocatalyst of $Pr_{0.1}Ce_{0.9}O_{2+\delta}$ is coated on a PBC surface to fabricate a composite air electrode,[170] resulting in enhanced ORR/OER catalytic activity and durability as the coating layer provided more active reaction sites and prevent the segregation of Ba. Moreover, as the Cr-containing metallic interconnects can degrade the performance of Ba/Sr-containing electrodes by forming $SrCrO_4$, $BaCrO_4$, or $BaCr_2O_4$ on the electrode surface,[171] a Ba/Sr-free catalyst coating-$Pr_{0.9}Fe_{0.7}Co_{0.3}O_3$ (PFC) was applied to the surface of the PBSCF electrode to enhance ORR activity and Cr-poisoning tolerance (Figure 18c–e).[172] Raman spectroscopy and DFT calculations confirmed that the PFC coating effectively diminishes the formation of Cr species, such as $(Ba_{1-x}Sr_x)CrO_4$, on the electrode surface. Similarly, to enhance the surface oxygen exchange process and tolerance against steam and CO_2 of the $BaCe_{0.5}Pr_{0.3}Y_{0.2}O_{3-\delta}$ (BCPY) support, the catalyst $PrNi_{0.5}Co_{0.5}O_3$ (PNC) was coated by infiltration (Figure 18f–i).[173] PNC exhibited superior catalytic performance and excellent tolerance against steam and CO_2 due to its high ionic-electronic ($H^+/O^{2-}/e^-$) conductivity and absence of alkaline earth metals. CO_2-TPD and EIS results indicated that the PNC-BCPY showed the lowest CO_2 absorption and a slight increase in ASR value in a CO_2-H_2O-containing atmosphere, mainly due to the effective coverage of the alkaline earth metal (Ba) in BCPY by PNC. This high activity and stability are attributed to the synergistic effect between the BCPY support and PNC nanoparticles, where BCPY provides a main proton path, and PNC nanoparticles facilitate surface oxygen exchange and steam adsorption/desorption processes due to enriched surface oxygen vacancies.

In addition to the incorporation of perovskite oxide nanoparticles, the deposition of metal oxide nanoparticles on the surface of triple-conductive air electrodes has emerged as a promising strategy for enhancing electrode reaction kinetics. Specifically, the impregnation of thermodynamically stable NiO onto the well-known BCFZY triple-conductive air electrode surface has been shown to significantly enhance its surface exchange kinetics.[174] The NiO nanoparticles, characterized by the high adsorption and rapid dissociation ability of oxygen molecules, facilitate the enlargement of active sites for surface-exchange reactions without compromising the integrity of the BCFZY surface or the triple-phase boundaries where the H_2O is formed. Consequently, the incorporation of NiO nanoparticles into the air electrode results in a substantial reduction in polarization resistance, accompanied by a superior power density of 780 mW cm^{-2} at 600°C. Moreover, a multi-cationic oxide nano-catalyst is introduced, denoted as PCNCFO with a nominal composition of $Pr_{0.2}Ce_{0.2}Ni_{0.2}Co_{0.2}Fe_{0.2}O_x$, for coating onto the surface of the typic PBC air electrodes.[175] The exceptional proton conductivity and high catalytic activity of PCNCFO nanoparticles (≈40 nm) enable perfect adhesion or even embedding onto PBC backbone. Notably, the Ce oxide component within the nanocatalyst coating can react with segregated Ba species to form active $BaCeO_{3-\delta}$ phases, while other constituent elements such as Pr, Ni, Co, and Fe exist on the PBC particle surface in the form of their respective oxides. Consequently, the PCNFO-PBC composite exhibits significantly enhanced hydration performance, attributed to the excellent proton conduction characteristics of $BaCeO_{3-\delta}$, along with activated surface properties facilitated by nanoscale metal oxide catalysts. On the other hand, the metal-oxide precursor solution used for impregnation may undergo chemical reactions with the backbone, resulting in the formation of perovskite phase nanoparticles on the surface, thereby constituting a composite electrode. For instance, when a $Co(NO_3)_2$ precursor solution is impregnated onto the surface of R-P-type $La_{1.2}Sr_{0.8}NiO_{4+\delta}$ (LS8N) oxide and subjected to high-temperature calcination, the deposited solute reacts with the LS8N matrix to form LSC nanoparticles, leading to the construction of an LSC/LS8N hetero-interface.[176] The exposed LSC/LS8N heterogeneous interface comes into contact with oxygen gas, significantly enhancing the ORR activity of the electrode, as evidenced by the sharply reduced ASR from 4.22 Ω cm^2 for the bare electrode to 0.49 Ω cm^2 for the LSC/LS8N (treated with 0.2 mol L^{-1} $Co(NO_3)_2$) air electrode.

Surface decoration of air electrode materials with nonreactive insulators, such as carbonates and metal oxides, has proven to be an effective method for regulating the electronic structure of oxides and modifying reaction kinetics. For instance, inactive insulators like MgO, CaO, and $BaCO_3$ have been shown to significantly enhance the catalytic activity of air electrodes.[177] Recently, the effect of coating carbonates and oxides, including Y_2O_3, $BaCO_3$, $SrCO_3$, and Al_2O_3, on the surface of the air electrode $PrBaFe_2O_{5+\delta}$ (PBF) was studied to explore the impact of the nonreactive insulator/ MIEC interface on catalytic activity.[178] The results revealed that insulators with work functions lower than that of the PBF electrode, such as Y_2O_3 and $BaCO_3$, accelerated ORR kinetics by donating electrons to the PBF surface, as confirmed by Bader charge analysis. In contrast, insulators with higher work functions, such as Al_2O_3, hindered ORR kinetics by extracting electrons from the PBF oxides.

It is worth noting that the impregnation process cannot control the size and uniform distribution of nanoparticles on the scaffold. Additionally, the adhesion between the impregnated layer and the scaffold may be compromised by differences in TEC and electrochemical reactions, leading to delamination. These issues inevitably result in lower electrode performance and limited long-term stability. Furthermore, the high-temperature re-sintering after impregnation and the multiple impregnation steps needed to achieve the desired loading significantly increase both economic and time costs, while also introducing defects and damage to the material's structure and composition. In conclusion, while the impregnation method can enhance electrode performance, it still presents challenges and shortcomings that need to be addressed.

4.2.3. Core-Shell Microstructure

The core-shell architecture, incorporating additional phases as the shell to cover the core material, also plays an important role in fabricating composite electrodes via modifying the surface properties. By incorporating a shell structure on the electrode surface, which functions as a nanocatalyst or protective layer, the reactive surface area of porous air electrode materials (core) can be significantly enhanced, leading to improved stability against H_2O, CO_2, and Cr.[179] Furthermore, when an adequate amount of shell nanoparticles with superior mixed ionic/electronic conductivity

forms a continuous charge transport pathway, the electronic and ionic conductivity of the nanocomposite electrode is substantially increased. This heterojunction structure also facilitates grain refinement, preventing excessive agglomeration of internal nanometal particles during high-temperature sintering.[180] These beneficial effects contribute to the development of nanocomposite air electrodes with exceptional electrocatalytic activity and stability.

Many studies have demonstrated that the synergistic effects of core-shell heterostructure exhibit higher electrochemical performance than the bare air electrode material.[181] For instance, shaped coatings are used to inhibit the thermal expansion of grains and the chemical reaction with pollutants to improve the stability of electrodes.[182] Based on these conclusions, a triple conductive air electrode material with a core-shell structure by impregnating Co onto $BaZr_{0.4}Ce_{0.4}Y_{0.2}O_{3-\delta}$ (BZCY) supports was prepared. The core is BZCY framework, and the outer shell layer contains cubic phase $Ba(Zr_{0.4}Ce_{0.4}Y_{0.2})_{1-x}Co_xO_{3-\delta}$, cubic spinel phase Co_3O_4 and cubic fluorite phase (Ce, Zr, Y)O_2.[181b] This electrode displayed a good match with the electrolyte and exhibited a stable and efficient ORR catalytic performance in an aqueous atmosphere. In addition, the LSCF (surface layer)-LSM (core) composite electrode with core-shell structure was also synthesized.[181a] The high coverage of the highly active LSCF film shell on the LSM particles not only enhanced the oxygen surface exchange by providing high surface area properties and active surface sites, but also significantly enhanced the ionic conductivity of the electrode due to the formation of a connected ion-conducting network. These factors help to significantly enhance the dissociation and surface diffusion processes of oxygen associated with the electrode reaction, thus showing better catalytic activity for ORR. In addition, Li et al.[181c] studied a composite electrode with a modified $La_2NiO_{4+\delta}$ shell structure on a PBSCF support (core layer) and found that the surface of this core-shell structure is rougher, which provides more activity for the cathode surface reaction. At the same time, the alkaline-earth element-free nature of the $La_2NiO_{4+\delta}$ layer alleviates the performance degradation of the electrode due to pollutants.

Moreover, considering that perovskite $SrFeO_{3-\delta}$ has higher oxygen ionic and electronic conductivity, while the R-P type $Sr_3Fe_2O_{7-\delta}$ shows potential for proton conducting ability due to its unique layered structure, a strategy was proposed to create a heterostructure junction by partially converting $SrFe_{0.9}Nb_{0.1}O_{3-\delta}$ (SFN113) to $Sr_3Fe_{1.8}Nb_{0.2}O_{7-\delta}$ (SFN327) on its surface to fabricate a core-shell microstructure (**Figure 19a**).[183] Specifically, SFN113 powder was mixed with $Sr(NO_3)_2$ at a mass ratio of 1:0.4 in a solution using urea as a chelating agent, Triton X-100 as a dispersant, and deionized water as the solvent. The Sr-species on the SFN113 surface can react with its bulk to in-situ generate R-P type SFN327, forming a heterostructure triple-conducting air electrode with an SFN113 core and a tetragonal SFN327 shell (SFN113@327) through sintering at different temperatures. This synthesized core-shell microstructure was confirmed by SEM, XRD, and TEM results. Furthermore, electrochemical performance tests indicated that the core-shell SFN113@327 exhibited superior electrochemical performance compared to the parent SFN113, attributable to the synergistic effects of the heterostructure and the proton conductivity of the SFN327 shell. Similarly, the core-shell was also observed in the $Ba(Co_{0.4}Fe_{0.4}Zr_{0.1}Y_{0.1})_{0.9}Al_{0.1}O_{3-\delta}$ (BCFZYA) (10%Al doped BCFZY) air electrode due to the rearrangement of atoms in the several nanometer depth surface regions (Figure 19b,c).[184] Interestingly, perovskite oxide electrode materials can develop in situ double-shell structures, enhancing electrocatalytic performance beyond the typical single-shell configurations. For instance, the K_2NiF_4-type $La_{1.2}Sr_{0.8}Ni_{0.5}Mn_{0.5}O_{4+\delta}$ (LSNM) air electrode, when annealed in air at 1200 °C, forms a dual-layer shell structure featuring a B-site deficient LSNM and a new perovskite phase on its surface.[185] This distinctive tri-layer architecture (core-shell B-shell A) arises from concurrent atom rearrangement and dopant segregation during calcination (Figure 19d), driven by the elastic and electrostatic interactions of the dopant with the surrounding lattice in the perovskite-related R-P phase oxide LSNM.[127b,186] Cation segregation occurs within a 4.5 nm depth surface region (Figure 19e), while segregated atoms (La, Sr) accumulate within a 2 nm depth surface region, resulting in a bi-shell microstructure. The B-site over-deficient structure in the A-shell facilitates the formation of Ni or Mn vacancies, ensuring abundant oxygen vacancies and providing pathways for various oxygen species. Simultaneously, the B-site deficient perovskite LSNM-B in the B-shell offers substantial capacity for accommodating oxygen species and electron mobility, promoting efficient oxygen charge transfer (Figure 19f,g). These attributes are highly advantageous for oxygen-related reactions. Consequently, this core/bi-shell LSNM air electrode demonstrates remarkable electrochemical performance, achieving a PPD of 799 mW cm^{-2} at 600 °C, surpassing many reported Ln_2NiO_4-based air electrodes.

Although two-phase air electrode materials with a core-shell structure have the above-mentioned advantages due to the protective layer on the surface, it cannot be ignored that the rate-controlling step of the ORR/OER is still mainly limited by the gap of charge transfer sub-step between the electrode bulk phase and the core-shell layer. How to effectively reduce the interphase charge transport resistance is still a key issue in the modification of cathode materials with core-shell structures. At present, researchers mainly improve the charge transfer step by reducing the thickness of the core-shell layer, such as combining multi-step penetration methods to control the thickness of the core-shell layer.[182]

4.3. Nanocomposite Air Electrode

Nanocomposites refer to materials that are composed of two or more distinct constituents at the nanoscale (i.e. less than 100 nm). Unlike composite electrodes fabricated through conventional mechanical blending or impregnation methods, the formation of nanoscale composites offers an expanded interface between these various phases. This heterojunction interface, which is generated during the material compounding process, exhibits enhanced uniformity and robustness. These characteristics yield numerous advantageous effects for electrochemical reactions, including higher catalytic activity, improved electronic and ionic conduction, and superior stability. Furthermore, these nanocomposite electrodes are typically comprised of a combination of materials with diverse functionalities, such as catalysts, conductors, and stabilizers. The integration of these phases at the nanoscale facilitates shorter paths for charge/mass transfer and

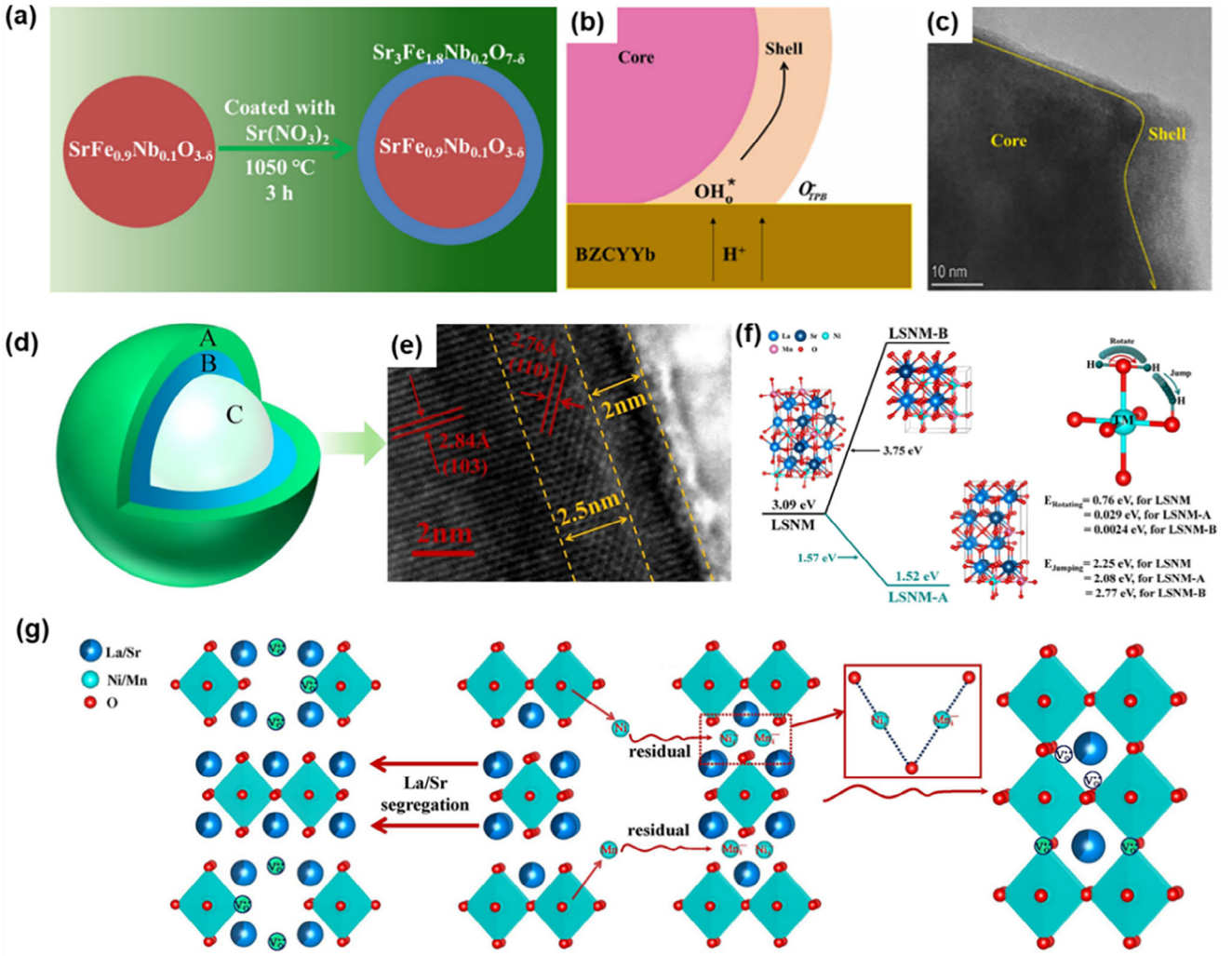

Figure 19. a) Schematic diagram of the core–shell structure SFN113@327; b) the enlarged core-shell surface region at the air electrode/electrolyte interface; c) HR-TEM image of the core-shell structure for BCFZYA ai electrode; d) schematic diagram and e) HR-TEM of the core/bi-shell structure for LSNM air electrode; f) the formation energy of oxygen vacancies comparison of LSNM-A in A-shell, LSNM-B in B-shell, LSNM in C-core and the proton rotating and jumping energy barrier; g) the phase conversion process for core-bi-shell structure for LSNM material. a) Reproduced with permission.[183] Copyright 2021, American Chemical Society. b,c) Reproduced with permission.[184] Copyright 2023, Elsevier. d–g) Reproduced with permission.[185] Copyright 2023, Elsevier.

provides a larger surface area for reactions. Owing to these benefits, nanocomposite electrodes have been garnering increasing attention.

4.3.1. Self-Assembly Strategy

Self-assembly refers to the process whereby a disordered system spontaneously forms an organized structure through interactions among its fundamental building blocks, such as attraction, repulsion, and chemical bonding, without external intervention.[187] This technique promotes the development of nanocomposite materials with multifunctional features through precise design and control of their properties.

For nanocomposite electrodes, the one-pot synthesis method is a crucial self-assembly strategy for obtaining nanocrystalline phases with complementary functions.[188] During this process, all components are synthesized simultaneously within the same reaction environment without additional treatment. The interactions between different phases can generate enhanced contact and smaller particles, ensuring intrinsic chemical cooperation among the components, uniform distribution, expanded heterointerfaces, enhanced three-phase boundaries, and robust interfacial cohesion.[189] These strong synergistic effects significantly enhance the electrochemical performance and durability, establishing self-assembly as a vital method in the preparation of nanophase catalysts.

Self-assembly technology is commonly employed to fabricate nanocomposite electrodes that possess both proton/electron-conducting phases and oxygen ion/electron-conducting phases to ensure high triple conductivity. For example, $BaCo_{0.7}(Ce_{0.8}Y_{0.2})_{0.3}O_{3-\delta}$ (BCCY) will spontaneously reconstruct

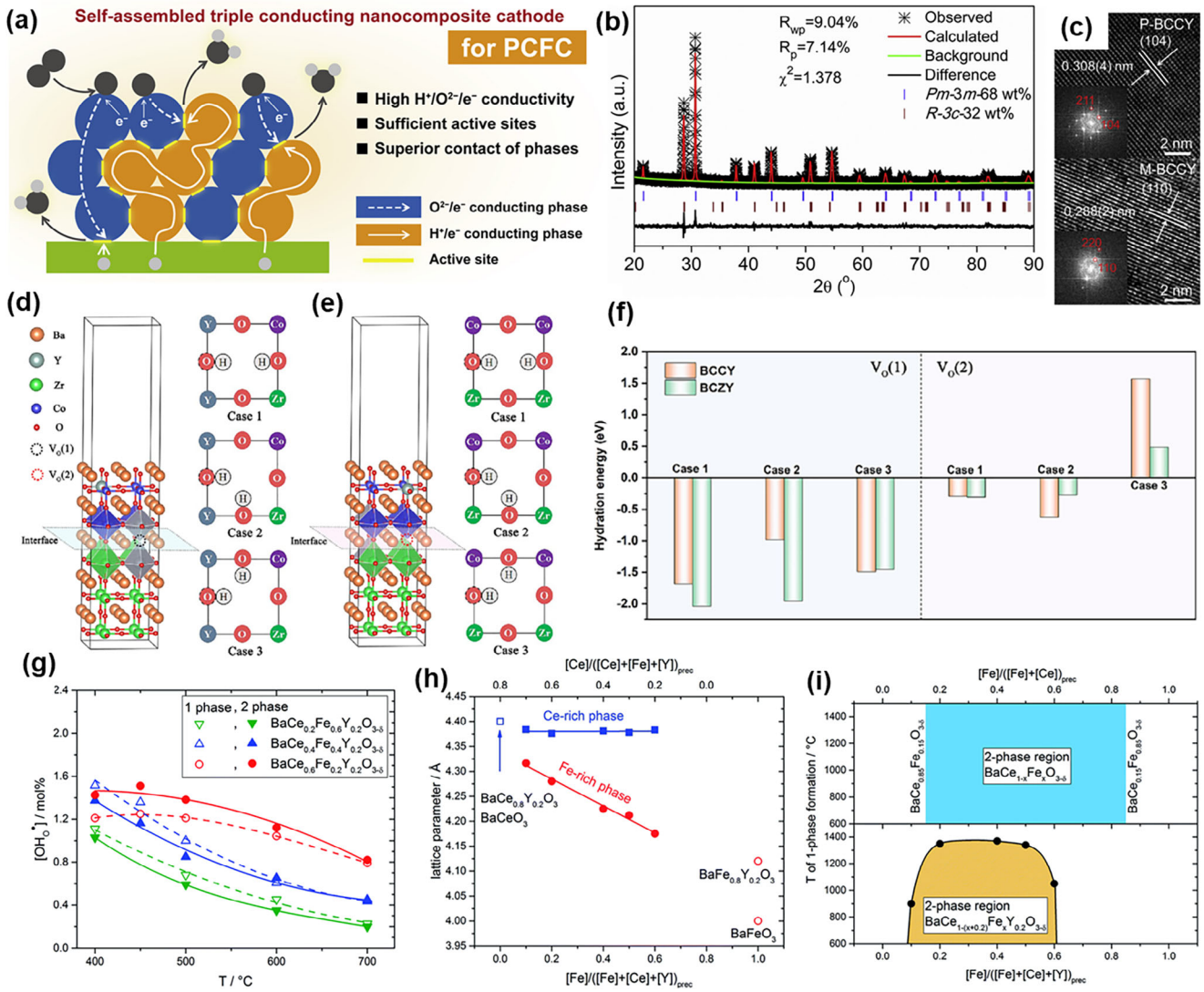

Figure 20. a) The electrode reaction processes for self-assembled nanocomposite electrode; b) refined XRD profiles and c) HR-TEM image of one-pot synthesized composite; d,e) schematic diagram of hydrated electrode interface and f) hydration energy of BCCY and BCZY electrodes; g) comparison of the proton concentration of two-phase nanocomposites; h) lattice parameters as functions of the Fe and Ce contents; i) the phase diagram shows the miscibility gaps. a–c) Reproduced with permission.[190] Copyright 2019, Elsevier. d–f) Reproduced with permission.[191] Copyright 2023, Elsevier. g–i) Reproduced with permission.[193] Copyright 2022, Royal Society of Chemistry.

into a Ce-rich H^+/e^- conducting phase close to $BaCe_{0.8}Y_{0.2}O_{3-\delta}$ (P-BCCY) and a Co-rich O^{2-}/e^- conducting phase close to $BaCo_{0.9}(Ce_{0.8}Y_{0.2})_{0.1}O_{3-\delta}$ (M-BCCY) after one-pot sintering (**Figure 20**a–c).[190] Furthermore, these two phases are well-mixed and intimately connected within the micrometer-sized grains (0.5-1.0 μm) at the nanoscale (P-MCCY-155.2 nm and M-BCCY-132.8 nm). Such nanocomposite also holds a high triple conducting capability. When the operating temperature ranges from 525 to 650 °C, the proton and oxygen ion conductivities measured using hydrogen and oxygen permeation reached 0.07–0.10 S cm^{-1} and 0.01–0.03 S cm^{-1}, respectively. Moreover, when the Ce was totally replaced by Zr for BCCY, the nanocomposite $BaCo_{0.7}(Zr_{0.8}Y_{0.2})_{0.3}O_{3-\delta}$ (BCZY) would self-assemble into three functional phases: a major cubic Co-rich phase (59.4 wt%, space group: Pm-3m), a minor cubic Zr-rich phase (35.6 wt%, space group: Pm-3m), and a very small amount of hexagonal Co-rich phase (5.0 wt%, space group: $P6_3/mmc$) (Figure 20d–f).[191] The catalytic activity and stability are enhanced due to the strongly interacting interface introduced by the interdiffusion of Co and Zr ions. A similar phenomena have been observed in cobalt-free materials, as the nanocomposite electrode $BaCe_xFe_{1-x}O_{3-\delta}$ (x = 0.36, 0.43, and 0.50) self-assembles into two phases after high-temperature sintering: the cubic perovskite (CP) and orthorhombic perovskite (OP) structures.[192] The CP phase $BaFeO_{3-\delta}$ demonstrates high oxygen ion permeability and electron conductivity, while the OP phase $BaCeO_{3-\delta}$ acts as a proton conductor. The self-assembled CP/OP mixture can be controlled by adjusting the Ce/Fe ratios to tailor the in-situ heterojunction structure and triple conductivity. Furthermore, the nominal composition $BaCe_{1-(x+0.2)}Fe_xY_{0.2}O_{3-\delta}$ ($0.1 \leq x \leq 0.6$) with Y sub-

stituting for Ce also self-assembles to form a Fe-rich cubic phase and a Ce-rich orthorhombic/trigonal phase via one-pot sol-gel method (Figure 20g–i).[193] The proton concentrations of the two-phase composite $BaCe_{0.4}Fe_{0.4}Y_{0.2}O_{3-\delta}$ in 17 mbar pH_2O reached 1.4 mol% due to the suitable ratios of different phases. A similar trend was also observed in the optimized $BaCe_{0.16}Y_{0.04}Fe_{0.8}O_{3-\delta}$ nanocomposite electrode, which was composed of a cubic $BaFe_x(Ce/Y)_{1-x}O_{3-\delta}$ phase (Pm-3m, 98.6wt%) and orthorhombic $Ba(Ce/Y)_xFe_{1-x}O_{3-\delta}$ phase (Pmcn, 3.4wt%).[194] Additionally, nanocomposite-$Ba(CeCo)_{0.4}(FeZr)_{0.1}O_{3-\delta}$ (BC-CFZ), containing both Ce-Zr and Co-Fe, also underwent a self-construction process, and a 40wt% mixed ion and electron-conducting phases of $BaCo_{1-(x+y+z)}Ce_xFe_yZr_zO_{3-\delta}$ (M-BCCFZ, Pm-3m) and another dominant (60%) proton-conducting phase of $BaCe_{1-(x+y+z)}Co_xZr_yFe_zO_{3-\delta}$ (H-BCCZF) were formed.[195] This low-cobalt-content self-assembled cubic-rhombohedral nanocomposite material exhibits suitable triple-conducting properties with a low enthalpy of protonation of -30 ± 9 kJ mol^{-1} and a low thermal expansion coefficient (TEC) of 9.6×10^{-6} K^{-1}. Such phase separation may derive from the significant differences between the B-site (Ce/Zr and Co/Fe) ionic radii,[193] this leads to automatic restructuring within the parent lattice to achieve a thermodynamically stable structure.

4.3.2. In Situ Exsolution Strategy

Exsolution is a controlled phase separation technique used to uniformly grow nanoparticles on a support, with perovskite oxides often serving as the host materials due to their good stability under redox conditions and high temperatures, as well as their ability to be doped and maintain non-stoichiometry. These nanoparticles (NPs), dispersed across the surface of oxide supports, significantly enhance catalytic activity through improved surface and interface properties, such as increased active surface area and phase boundaries. Additionally, exsolved nanoparticles are strongly anchored to the oxide support, creating robust particle-substrate interactions. This anchoring results in exceptional resistance to agglomeration, carbon coking, and sulfur poisoning, enabling long-term stable operations.[196] However, exsolution primarily occurs in reducing atmospheres (e.g., H_2) and, in oxidizing environments like the air electrode working atmosphere at high temperatures, these nanoparticles may gradually re-dissolve into the parent lattice, raising stability concerns for air electrode materials. Therefore, efforts are ongoing to identify suitable driving forces for exsolution and develop stable nanoparticles that can withstand wet air conditions to fabricate the nanocomposite air electrode for R-PCECs.

Utilizing H_2O as a mediator to induce the in-situ formation of active catalytic nanoparticles has demonstrated significant potential for enhancing electrochemical reactions. For example, when the highly moisture-tolerant layered perovskite oxide $PrBa_{0.8}Ca_{0.2}Co_2O_{5+\delta}$ (PBCC) is exposed to wet air (3 vol% H_2O–air), Ba ions segregated by H_2O spontaneously combine with Co ions from the host oxide through topotactic cation exchange, resulting in the in-situ generation of $BaCoO_{3-\delta}$ (BCO) catalysts on the bulk PBCC (**Figure 21a–c**).[197] This process leads to a heterogeneous catalyst-coated surface, as evidenced by the SEM, TEM, EDX, and Raman profilometry of the protonated PBCC sample ((Figure 21a).[197] Furthermore, the oxygen surface exchange kinetics are significantly improved due to the lower activation energy required for BCO nanoparticles (0.60 eV versus 1.42 eV), as revealed by DFT calculations.[197a] Detailed examination of the OER processes using DFT and density of states (DOS) reveals that H_2O adsorbs on the $BaCoO_3$ (110) surface and dissociates into surface species (i.e., OH* and H*). The OH* intermediate then dissociates into O* and H*, leading to the formation and desorption of O_2 on PBCC (010) (Figure 21b,c).[197b] As a result, the BCO-PBCC exhibited excellent electrochemical performance- the ASR value is only 0.02-0.035 Ω cm^2 at 700°C. This exceptional activity is attributed to the rapid water dissociation on BCO nanoparticles and efficient oxygen desorption on PBCC. BCO nanoparticles stand out as superior catalyst particles, maintaining stability in high steam and CO_2 atmospheres, and ensuring robust performance in both FC and EC modes.[197b] The in-situ exsolution of BCO NPs was also observed in a $Pr_{1-x}Ba_xCoO_{3-\delta}$ thin film coated $(La_{0.6}Sr_{0.4})_{0.95}Co_{0.2}Fe_{0.8}O_{3-\delta}$ (LSCF) air electrode exposed to high concentrations of water.[169] This heterogeneous catalyst coating significantly enhanced the electrocatalytic activity and stability of the LSCF electrode, attributed to improved surface oxygen exchange, rapid proton diffusion, and efficient H_2O and O_2 dissociation on the catalysts, as confirmed by DFT analyses. Similarly, $PrBaCo_{1.6}Fe_{0.2}Nb_{0.2}O_{5+\delta}$ (PBCFN) can interact with steam to generate Nb-deficient particles $PrBaCo_{1.6}Fe_{0.2}Nb_{0.2-x}O_{5+\delta}$ on its surface.[198] SEM images of the PBCFN electrode before and after testing revealed the presence of these nanoparticles, confirmed by HAADF TEM results, which indicated they are Nb-deficient and provide more active reaction sites in wet air. Comparable Nb-deficient NPs were also formed on the $Ba_{0.9}Co_{0.7}Fe_{0.2}Nb_{0.1}O_{3-\delta}$ (BCFN) air electrode skeleton via a water-promoted surface restructuring process (Figure 21d,e).[199] Calculations of segregation energy (E_{segt}) for co-dopant cations and their interaction with steam indicated a segregation order of Co > Fe > Nb (Figure 21f), leading to Nb-deficient NPs.

When a novel air electrode material, $Ba_{1-x}Gd_{0.8}La_{0.2+x}Co_2O_{6-\delta}$ (BGLC), was used in R-PCEC in electrolysis mode at 600 °C under 1.5 bar of steam for 72 h, partial substitution of Ba with La ($x < 0.5$) resulted in two phases: double perovskite and hexagonal BCO.[200] Indeed, XRD analysis showed that BGLC with 50% Ba substitution ($x = 0.5$) remained stable under these conditions, without BCO precipitation. These findings may suggest that both high steam concentrations and the unique lattice structure (segregation cations and their interactions with neighboring atoms and oxygen vacancies) contribute to in situ exsolution of NPs. Another sample is the A-site doping air electrode. Specifically, $BaCo_{0.4}Fe_{0.4}Zr_{0.18}Y_{0.02}O_{3-\delta}$, a well-known TCO air electrode, remains stable in wet air. However, partial replacement of Ba with monovalent alkali metals (Li, Na, K) to fabricate $K_{0.05}Ba_{0.95}Co_{0.4}Fe_{0.4}Zr_{0.18}Y_{0.02}O_{3-\delta}$ (KBCFZY) led to the exsolution of BaO_x on the surface in humidified air (Figure 21g–i).[201] This exsolution is driven by the formation of barium and oxygen vacancies facilitated by A-site acceptor doping, and DFT results showed a decrease in oxygen vacancy formation energy from 0.10 to -0.20 eV after K-doping (Figure 21i). Additionally, water vapor likely contributes to this process through hydration and hydrogenation reactions that redistribute holes and redox-active elements, triggering BaO_x exsolution via lattice cation

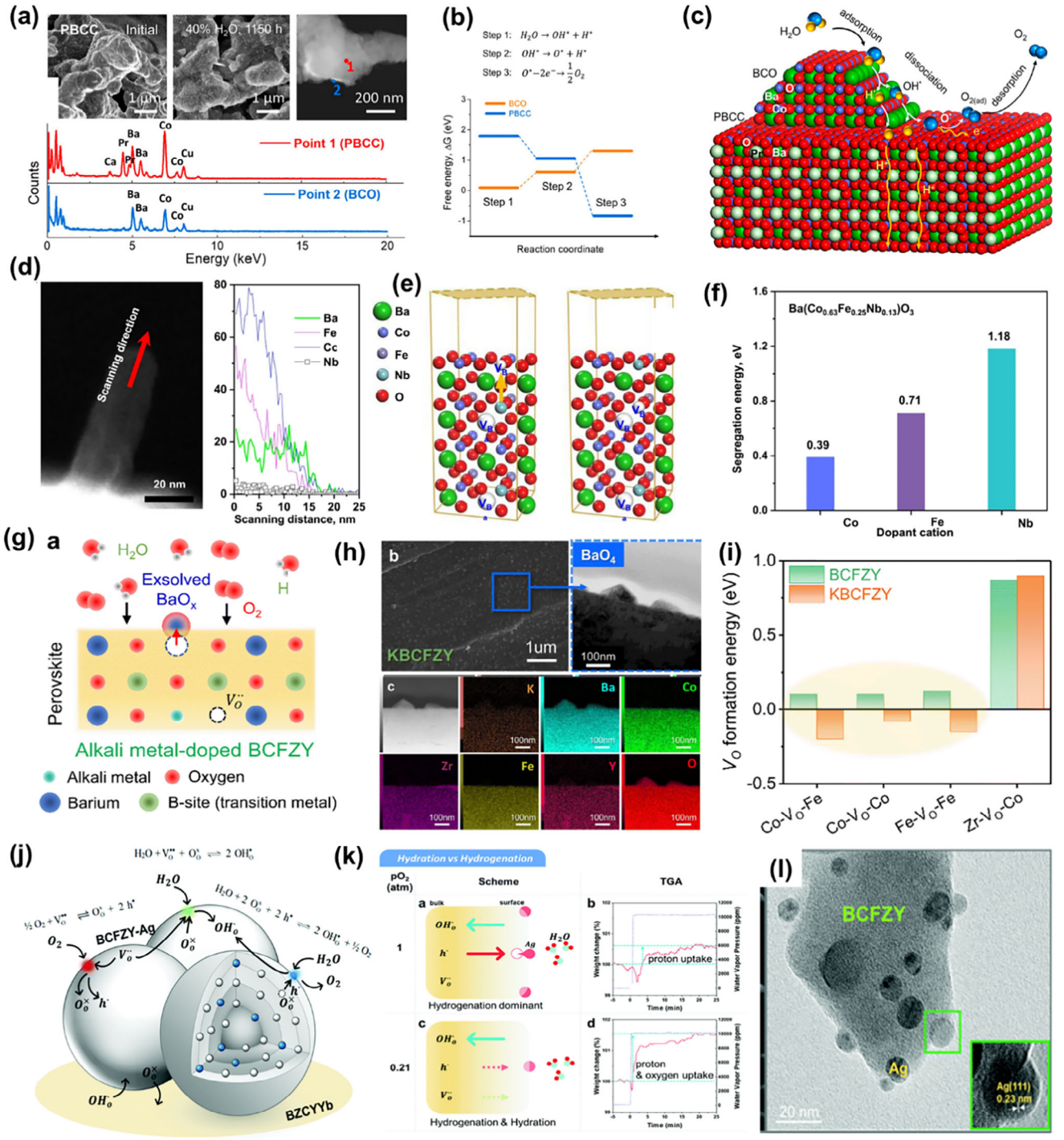

Figure 21. a) SEM, TEM, and EDX mapping images of the air electrodes before and after testing in humid conditions; b) Gibbs free energy changes for the OER on the exsolved air electrode surface; c) proposed OER mechanism; d) elemental profile along the scanning line shown in the TEM image; e) models of segregated Nb from the bulk to the surface; f) calculated segregation energy; g) reaction mechanism of ABCFZY in humidified air; h) BaO_x exsolution onto KBCFZY (FE-SEM, TEM, HR-TEM, and FFT pattern) and the mapping results; i) the DFT calculated oxygen vacancy formation energy; j) schematic diagram of water-mediated ex-solution; k) water uptake and thermogravimetric profiles of dense BCFZY-Ag pellets; l) HRTEM image of exsolved Ag nanoparticles, (inset) magnified image. a–c) Reproduced with permission.[197b] Copyright 2021, American Chemical Society. d–f) Reproduced with permission.[199] Copyright 2022, Springer Nature. g–i) Reproduced with permission[201] Copyright 2024, Royal Society of Chemistry. j–l) Reproduced from ref. [202] with permission from the Royal Society of Chemistry.

vacancy formation. Additional factors such as relaxation of lattice strain and defect interactions may also contribute. Moreover, the highly basic BaO_x phases can act as catalysts for acid-base reactions, particularly hydration, enhancing the electrode's activity by facilitating proton incorporation. This feature ensured the KBCFZY air electrodes demonstrated higher activity and stability for both ORR and OER, achieving over 1.65 W cm^{-2} PPD in FC mode and over 6.5 A cm^{-2} in EC mode at 1.3 V at 650°C. Another instance of water-mediated exsolution involves Ag-doped $BaCo_{0.4}Fe_{0.4}Zr_{0.1}Y_{0.1}O_{3-\delta}$ (BCFZY-Ag).[202] Specifically, when exposed to a humid atmosphere, the redox-active elements (Ag^+ in this case) in protonic conducting oxides reacted with water through hydrogenation, consuming electron holes generated by the exsolution process (Figure 21j,k). This promoted the exsolution of Ag^+ with extreme reducibility, resulting in in situ formation of Ag nanocatalysts on the BCFZY surface without additional treatment (Figure 21l). Notably, unlike other metal oxide catalysts with generally low electronic conductivity and thus slow down the charge transfer process on the electrode surface, Ag exhibits outstanding electronic conductivity, which facilitates charge transfer in triple-conducting electrodes. Furthermore, it is stable under high oxygen partial pressure conditions and maintains excellent gas adsorption/desorption and anti-poisoning properties, resulting in the Ag-BCFZY air electrode exhibiting robust dual catalytic performance and stability for both ORR and OER processes.

Additionally, the lattice strain in perovskite oxides also plays a critical role in regulating the size and distribution of exsolved nanoparticles. For instance, studies on 100 nm $La_{0.2}Sr_{0.7}Ni_{0.1}Ti_{0.9}O_{3-\delta}$ thin films revealed that compressive strain produces smaller nanoparticles with higher population densities compared to tensile strain. This phenomenon is attributed to the relaxation of lattice misfit strain energy, which promotes surface nucleation kinetics under compressive conditions. However, contrasting behavior has been observed in $La_{0.6}Sr_{0.4}FeO_3$ (LSF) thin films, where tensile strain enhances oxygen vacancy formation, favoring Fe nanoparticle exsolution. These findings highlight the importance of tailoring the inherent structural properties of perovskite oxide supports to optimize strain-induced behaviors in thin-film systems.

4.3.3. Self-assembly-triggered in-situ exsolution

Furthermore, the self-assembly process of materials can initiate the exsolution of nanoparticles, as confirmed by the influence of sintering temperature control on the air electrode. For instance, under high-temperature firing conditions (1100 °C for 10 h), the air electrode $Ba_2Co_{1.5}Mo_{0.25}Nb_{0.25}O_{6-\delta}$ (BC1.5MN) decomposes into a single-perovskite phase $BaCoO_{3-\delta}$ (SP-BCO, 55 wt%) and a double-perovskite phase $Ba_{2-x}Co_{1.5-x}Mo_{0.5}Nb_{0.5}O_{6-\delta}$ (DP-BCMN, 45 wt%) (**Figure 22**a–c).[203] The exsolved BCO phase enhances surface catalytic activity for the ORR and the hydration reaction for steam splitting (OER), as evidenced by the lower valence state of Co cations (Figure 22d), a reduced Co-O coordination number observed in X-ray absorption near edge structure (XANES), and increased H_2O adsorption shown in H_2O-TPD plots (Figure 22e). The interaction between SP-BCO and DP-BCMN improves structural stability and facilitates the diffusion of triple-ions, resulting in excellent cycling stability of 220 h and outstanding performance with a PPD of 1.17 W cm^{-2} and an electrolysis current density of 2.04 A cm^{-2} at 650°C. Similarly, the double perovskite oxide $PrSrCo_{1.8}Nb_{0.2}O_{6-\delta}$ (PSCN) in-situ generates $SrCo_{0.5}Nb_{0.5}O_{3-\delta}$ (SCN) NPs on its surface during calcination (900 °C for 2 h) and maintains stability throughout annealing (Figure 22f–i).[204] XRD and SEM results at different sintering temperatures (800-1000°C), along with corresponding DFT calculations, suggest that the presence of a metastable structure during calcination triggered exsolution (Figure 22h–i). Electrochemical measurements and DFT calculations indicate that the improved OER and ORR activities of the air electrode are due to the fast kinetics of surface oxygen exchange, low oxygen formation energy, and low dissociation energy for H_2O and O_2 induced by the SCN clusters and their strong interface with PSCN.

Finally, specific lattice regulation techniques, such as the introduction of A-site defects and the modulation of M-O bonds within the bulk phase, can facilitate the in-situ generation of NPs through a self-assembly transformation process under dry air conditions. The prepared precursor, $Sr_{0.9}Ce_{0.1}Fe_{0.8}Ni_{0.2}O_{3-\delta}$ (SCFN),[205] undergoes automatic reconstruction into multiple phases: a tetragonal $SrFeO_{3-\delta}$ (SF)-based phase (I4/mmm, 77.4wt%) and an R-P-based phase (I4/mmm, 11.7wt%) with surfaces decorated by CeO_2 (Fm-3m, 4.8wt%) and NiO (Fm-3m, 6.1wt%) nanoparticles. Mass spectrometry (MS) and Fourier transform infrared (FTIR) spectroscopy, coupled with theoretical calculations, demonstrate that the RP phase enhances hydration and proton transfer, while NiO and CeO_2 nanoparticles facilitate O_2 surface exchange and the transfer of O^{2-} from the surface to the primary perovskite phase. The synergistic effect among these phases ensures rapid triple conduction ($H^+/O^{2-}/e^-$), thereby enhancing ORR/OER activities. Similar research was conducted on synthesizing precursors with the nominal composition $Ba_{0.95}(Co_{0.4}Fe_{0.4}Zr_{0.1}Y_{0.1})_{0.95}Ni_{0.05}O_{3-\delta}$ (BCFZYN-095). Under an oxidizing atmosphere, the material self-assembled to form a major perovskite phase (m-BCFZYN, Pm-3m) and a minor NiO phase (Fm-3m) (Figure 22j–l).[206] The in-situ generation of nanoparticles on the surface of the parent perovskite oxide is driven by several factors: A-site cation deficiency, the low co-segregation energy of Ni ions, and a spatial effect related to the ionic radius difference between Ni^{3+} (0.56 Å) and Ni^{2+} (0.69 Å).[206a,207] The major perovskite phase, achieved through precise cation non-stoichiometric manipulation, enhances bulk proton conduction and O_2 desorption. The hydration energy (E_{hydr}) of D-BCFZYN is only -0.155 eV, which is significantly lower than that of the pristine BCFZY (0.117 eV). Concurrently, the NiO nanoparticles facilitate the oxygen and steam surface exchange processes, as demonstrated by the notable lower energies for steam and oxygen adsorption on the NiO(111) surface (−1.679 eV and −3.301 eV) (Figure 22k). These positive effects result in improved ORR and OER catalytic performance. Moreover, when the stoichiometric $Ba(Co_{0.4}Fe_{0.4}Zr_{0.1}Y_{0.1})_{0.95}Ni_{0.05}O_{3-\delta}$ perovskite oxide without deficiency was further modified by the anion F^- with greater electronegativity, the nanocomposite-$Ba(Co_{0.4}Fe_{0.4}Zr_{0.1}Y_{0.1})_{0.95}Ni_{0.05}F_{0.1}O_{2.9-\delta}$ (N-BCFZYNF) also exhibited a major cubic perovskite phase (99.0 wt%, Pm-3m) and a minor NiO phase (1.0 wt%, Fm-3m) (Figure 22m,n).[208] The nanoparticle generation can be associated with the low co-segregation energy of Ni ions and attenuated metal-oxygen chemical bonds

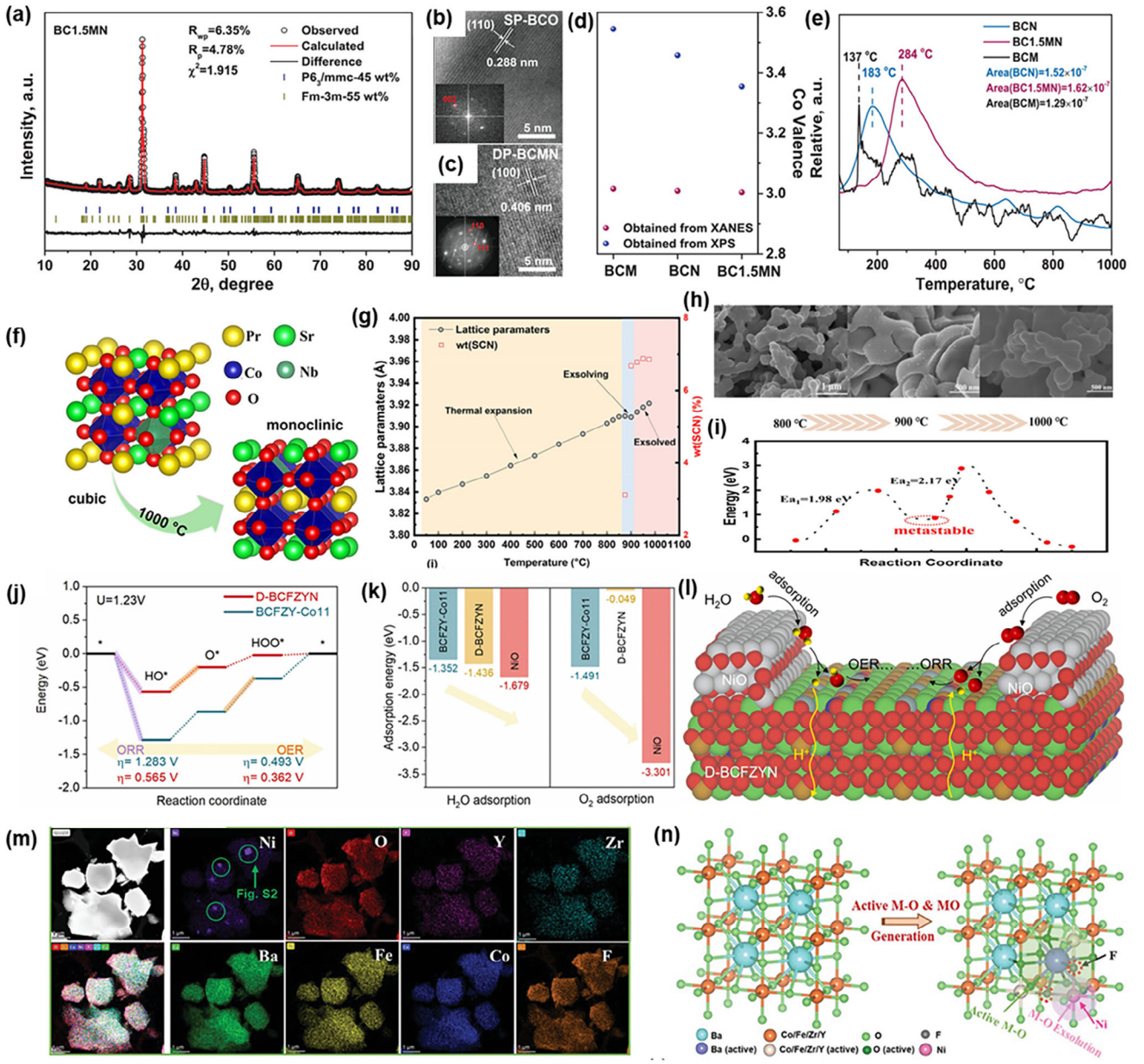

Figure 22. a) Rietveld results of B1.5MN; HRTEM images of b) BCO and c) BC1.5MN; d) Co valence state from XANES and XPS; e) H_2O-TPD signal for BCM, BCM, and BC1.5MN; f) phase transition process; g) variation of lattice parameters of PSCN at increasing temperatures; h) SEM images of powders; i) energy profiles along the different reaction coordinate; j) ORR/OER reaction paths and calculated free energies; k) adsorption of H_2O and O_2; l) proposed ORR/OER process for D-BCFZYN air electrode; m) mapping results n) active M-O and MO for N-BCFZYN air electrode. a–e) Reproduced with permission.[203] Copyright 2022, Wiley. f–i) Reproduced with permission.[204] Copyright 2024, American Chemical Society. j–l) Reproduced with permission.[206a] Copyright 2024, Elsevier. m,n) Reproduced with permission.[208] Copyright 2024, Wiley.

in the lattice. Consequently, the synergistic optimization effects weaken bulk-phase metal-oxygen bonds and surface formation of metal oxide nano-catalysts substantially improved oxygen adsorption/desorption and hydration rates, as well as capabilities of O^{2-}/H^+ migration, resulting in better performance in FC and EC modes. Interestingly, the Ni-doped $PrBaFe_{1.9}Mo_{0.1}O_{6-\delta}$ (PBFMN) air electrode also in situ generated the NiO partially via self-assembled process.[209] The bulk Ni-modified PBFMN promoted oxygen vacancy formation and thus enhanced the proton migration rate while NiO NPs improved oxygen surface exchange by facilitating oxygen adsorption and dissociation.

4.4. High Entropy Air Electrode

It is widely accepted that excess energy in a system typically drives spontaneous transitions to low-energy steady states,

increasing the overall entropy of the system. Inspired by this phenomenon, researchers have developed high-entropy perovskites (HEPs) (**Figure 23a**). These materials utilize the high configurational entropy of perovskite to enhance thermodynamic stability, surpassing conventional materials in this regard. Notably, HEPs retain robust structural stability without compromising their catalytic activity (Figure 23b).[210]

High-entropy materials were first introduced as high-entropy alloys (HEAs) in 2004.[211] HEAs contain five or more principal elements at near-equimolar ratios, typically ranging from 5% to 20% molar ratio. The defining characteristic of HEAs is their high configurational entropy, which can be expressed as Equation (25):

$$S_{config} = -R\left(\sum_{i=1}^{n} x_i \ln\left(x_i\right)\right) \tag{25}$$

where R is the ideal gas constant, x_i represents the molar fraction of elements, and n is the number of elements. The higher the value of the configurational entropy, the greater the likelihood of forming a stable single-phase crystal structure. According to this equation, the maximum configurational entropy occurs in systems with equal atomic fractions, and the maximum S_{config} values are1.61R and 2.30R when n is 5 and 10, respectively. According to published results,[212] materials with an S_{config} of 1.5R or greater are classified as "high entropy," those with S_{config} values between 1.0R and 1.5R are categorized as "medium entropy," and those with S_{config} values of 1.0R or less are considered "low entropy." Consequently, high-entropy oxides typically consist of at least five principal metallic elements in equal or near-equal proportions.[213]

Like HEAs, the configurational entropy of HEPs utilized as the air electrode can also be defined by taking both cations and anions into consideration, which is given by Equation (26).

$$S_{\text{config}} = -R\left[\left(\sum_{a=1}^{A} x_a \ln x_a + \sum_{b=1}^{B} x_b \ln x_b\right)_{\text{cation-site}} + \left(\sum_{j=1}^{M} x_j \ln x_j\right)_{\text{anion-site}}\right] \tag{26}$$

Here, A, B, and M refer to the number of elements present at the A-site, B-site, and anion positions, respectively; x_a, x_b, and x_j indicate their corresponding mole fractions; and R is the universal gas constant (R = 8.314 J (mol K)$^{-1}$).

The HEP materials, with configurational entropy (S_{config}) equal to or greater than 1.5R (Figure 23c), typically feature A-sites occupied by alkali, alkaline earth, or rare earth metal cations, B-sites occupied by transition metal cations, and M-sites by halogen, oxygen, nitrogen, or sulfur anions[210b] Unlike conventional perovskites, HEPs exhibit greater lattice distortion due to the substitution of multiple elements with differing ionic radii.[214] The increase in configurational entropy can lead to the entropy stabilization of HEPs, resulting in a high probability of stabilizing a single-phase crystal structure when the entropy exceeds 1.5R, thus classifying them as entropy-stabilized perovskites.[215] Although not all HEPs are entropy-stabilized, the high entropy imparts four main effects: high-entropy effect, severe lattice distortion, sluggish diffusion, and cocktail effect.[216] Consequently, HEPs possess significant advantages over traditional materials, such as superior mechanical strength, structural stability, high-temperature stability, and exceptional magnetocaloric effects.[217]

4.4.1. High Entropy Oxides

Due to the attractive properties of high-entropy materials, significant efforts have been dedicated to employing this strategy to design efficient air electrodes for R-PCEC. The first reported high-entropy air electrode for proton-conducting fuel cells was the spinel ceramic oxide, $Fe_{0.6}Mn_{0.6}Co_{0.6}Ni_{0.6}Cr_{0.6}O_4$ (FMCNC).[218] High-temperature and in-situ X-ray diffraction (XRD) results demonstrated that FMCNC exhibits excellent phase stability during high-temperature sintering and in CO_2-containing atmospheres. Atomic-level studies, conducted using first-principle calculations, indicate that the high-entropy structure merges the benefits of the individual oxides. This results in a lower O_2 adsorption energy for FMCNC, specifically −2.85 eV on the exposed (001) surface, suggesting that O_2 adsorption is thermodynamically favorable, thereby enhancing catalytic activity. Furthermore, compared to traditional spinel oxides, the high-entropy FMCNC exhibits lower hydration energy (−2.85 eV) and a p-band center for oxygen that is closer to the Fermi level (p-DOS, −2.56 eV). These features indicate improved protonation and oxygen migration characteristics in the high-entropy oxide. Consequently, by incorporating high-entropy into spinel oxides, the high-performance FMCNC air electrode demonstrated significantly reduced polarization resistance of 0.057 Ω·cm^2 at 700 °C, which is half of that observed in traditional $Mn_{1.6}Co_{1.4}O_4$ (MCO) without the high-entropy design.

4.4.2. High Entropy Perovskite Oxides—B Site

Moreover, the high-entropy perovskite oxides (HEPOs) have also been extensively investigated as air electrodes for RePCC. For instance, the B-site HEPO with the composition $BaCo_{0.2}Fe_{0.2}Zr_{0.2}Sn_{0.2}Pr_{0.2}O_{3-\delta}$ (BCFZSP) was meticulously designed (Figure 23d–f),[219] and the estimated atom ratio was further confirmed by the X-ray spectroscopy mapping results. Compared to the typical BCFZY, which possesses triple conducting properties, the high-entropy BCFZSP material exhibits significantly stronger hydration and dehydration capabilities. This is evidenced by the higher proton concentrations, reaching 6.92 mol% vs 1.34 mol% at 500 °C. Furthermore, ECR measurements indicated that both the oxygen and proton surface exchange and bulk migration kinetics were enhanced in the BCFZSP electrode. This enhancement contributes to superior catalytic performance, as demonstrated by the polarization resistance of BCFZSP (0.448 Ω·cm^2), which is approximately half that of BCFZY (0.932 Ω·cm^2). Notably, BCFZSP maintains a pure cubic phase in a highly concentrated steam atmosphere with $p(H_2O)$ as high as 50% atm, indicating its excellent structural stability under high-steam conditions. To address the issue of interface degradation and separation between the cobalt-based perovskite air electrode and the proton-conducting electrolyte, another B-site HEPO, $BaCo_{0.2}Zn_{0.2}Ga_{0.2}Zr_{0.2}Y_{0.2}O_{3-\delta}$ (BCZGZY),[220] was designed with a cubic phase structure. The incorporation of Zn, Ga, and Y cations not only reduces the

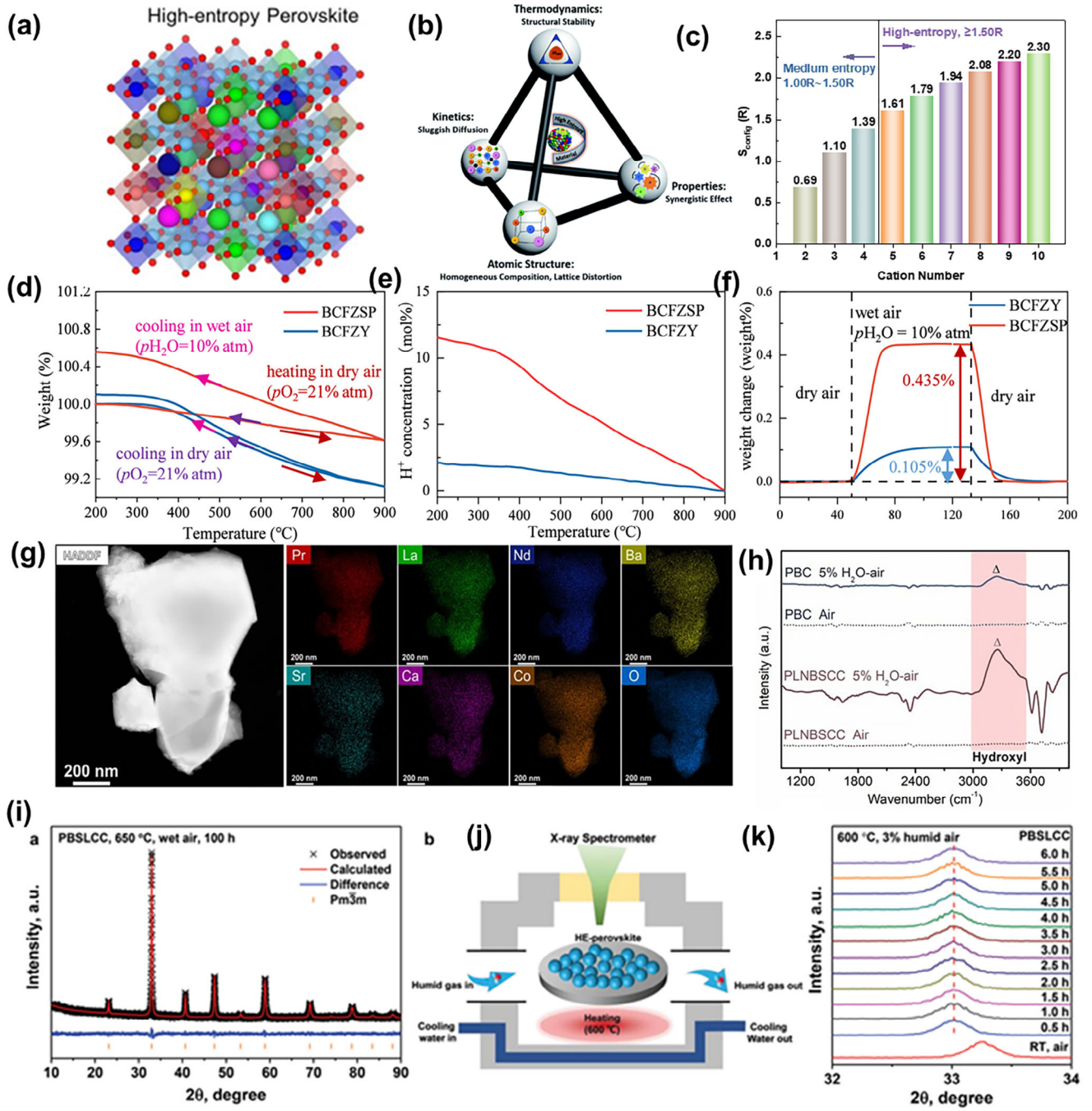

Figure 23. a) Schematic diagram of the HEPO lattice structure; b) the four core effects of high-entropy strategy; c) the relationship between entropy value and the number of cations; d) TGA plots in dry and wet atmospheres; e) calculated proton concentrations in the BCFZSP and BCFZY samples; f) thermogravimetric relaxation curves based on switching from dry to humid condition; g) EDX spectra of prepared PLNBSCC powder and its h) IR spectra in dry air and 5% H_2O–air; i) the Rietveld refinement of the PBSLCC sample; j) schematics of the experimental settings used for in situ XRD measurement and k) the corresponding patterns. a) Reproduced with permission.[212a] Copyright 2023, Elsevier. b) Reproduced with permission.[230] Copyright 2021, Royal Society of Chemistry. d–f) Reproduced with permission.[219] Copyright 2023, Elsevier. g,h) Reproduced with permission.[222] Copyright 2022, Springer Nature. i–k) Reproduced with permission.[223] Copyright 2023, Wiley.

average valence state of $Co^{3+/4+}$ but also increases the ionic radius at the B-site within the perovskite structure. This modification weakens the Co-O bond strength, thereby facilitating the generation of oxygen vacancies in BCZGZY. Consequently, BCZGZY exhibits enhanced hydrophilicity, as indicated by the noticeable mass variation in wet air (0.75%), and a lower TEC value of 12.75×10^{-6} K^{-1}. These attributes promote the formation of protonic defects and cohesion robust interface, which are beneficial for ORR/OER catalytic activity and stability.

Recently, high-entropy R-P oxides with a K_2NiF_4-type structure have also been developed as air electrode materials. Specifically, the novel HEPO $La_{1.2}Sr_{0.8}Mn_{0.2}Fe_{0.2}Co_{0.2}Ni_{0.2}Cu_{0.2}O_{4+\delta}$ (LSMFCNC) was synthesized via B-site entropy engineering.[221] The LSMFCNC exhibited a single tetragonal layered K_2NiF_4 structure with I4/mmm space group symmetry and demonstrated excellent chemical compatibility with the BZCY electrolyte. Notably, by leveraging the unique properties of the multiple elements Mn, Fe, Co, Ni, and Cu, the B-site transition metals in LSMFCNC evolved into a lower average B-site valence state and increased bond length. This results in the expansion of the crystal structure and a reduction in the bond strength between cations and oxygen ions. Consequently, this promotes the formation of oxygen vacancies and achieves high proton and oxygen diffusion rates.

4.4.3. High Entropy Perovskite Oxides—A Site

In perovskite oxides, the B-site transition metal ions are typically regarded as catalytic active sites for electrode reactions. Consequently, increasing the configurational entropy at the B-site can inevitably reduce electrocatalytic activity, even though it effectively enhances the structural stability of electrode materials. To address this issue, A-site configuration HEPOs have also been designed, offering abundant opportunities for improved design and customization of bifunctional catalysts for ORR/OER. The novel A-site HEPO, specifically $Pr_{1/6}La_{1/6}Nd_{1/6}Ba_{1/6}Sr_{1/6}Ca_{1/6}CoO_{3-\delta}$ (PLNBSCC) (Figure 23g,h), derived from the $PrBaCo_2O_{5+\delta}$ (PBC) prototype, has been reported as a highly active and stable air electrode for ORR and OER in R-PCEC.[222] While the composition of the material was not explicitly determined via inductively coupled plasma (ICP) analysis, its atomic composition was corroborated by the EDX spectrum results, which indicated a strong correlation with the theoretical values. The increased configurational entropy (S_{config} = 1.79R) enables the stable formation of a cubic structure in PLNBSCC oxide at lower temperatures, preventing impurity phases and poor crystallinity compared to PBC oxide. The synergistic strengthening from the abundant trivalent rare earth elements and divalent alkaline earth metal elements at the A-site in PLNBSCC significantly enhances the triple conductivity (e^-: 950–2038 S cm^{-1} at 800–500 °C; O^{2-}: 0.064 S cm^{-1} at 750 °C) and hydration ability, as evidenced by the prominent hydroxyl characteristic peak in high-temperature in situ IR spectra. These significant improvements in the PLNBSCC air electrode, driven by the increased configurational entropy, resulting in excellent performance in single cells, demonstrating long-term stability (500 hours), thermal cycling tolerance (nearly 1000 min), high water pressure tolerance (pH_2O = 30% in air), and bifunctional cycling tests (1120 minutes, 43 cycles). Similarly, another A-site HEPO air electrode, with the detailed composition $Pr_{0.2}Ba_{0.2}Sr_{0.2}La_{0.2}Ca_{0.2}CoO_{3-\delta}$ (PBSLCC) (Figure 23i–k), was meticulously designed.[223] This design capitalizes on the exceptional conductivity and expansion coefficient of $Pr^{2+/3+}$, the active oxidation reactivity and reduced B-O bond strength imparted by La^{3+}, and the stable chemical properties and cost-effectiveness of Ca^{2+}. The construction of this high-entropy system ensured that the cubic phase structure and morphology of PBSLCC remained stable even after treatment in wet air with a high steam concentration (pH_2O = 20%) at 650 °C for 100 h. Furthermore, STEM–EDS mapping of PBSLCC after 600 h of treatment in wet air demonstrated that the elements Pr, Ba, Sr, La, Ca, and Co were uniformly distributed within the grains, suggesting a robust crystal structure without phase segregation (e.g., SrO, $SrCoO_3$, or $BaCoO_3$). The composition of the PBSLCC sample was confirmed to be $Pr_{0.2}Ba_{0.19}Sr_{0.19}La_{0.19}Ca_{0.23}CoO_{3-\delta}$ through ICP analysis, demonstrating a close alignment with the intended stoichiometric ratio following steam treatment. Additionally, PBSLCC exhibited superior oxygen-steam reaction kinetics and excellent durability, with a low Rp value of 2.13 Ω cm^2 at 500 °C and stable operation at 550 °C for 600 h in wet air, showing a deterioration rate of only 0.013 Ω cm^2 per 100 h—significantly lower than the parent oxide $PrBa_{0.8}Sr_{0.2}Co_2O_{6-\delta}$ (PBSC), which exhibited an ASR of 2.13 Ω cm^2 at 500 °C and a deterioration rate of 0.21 Ω cm^2 per 100 h at 550°C. Consequently, the R-PCEC with the HE-PBSLCC air electrode demonstrated a high peak power density of 1.51 W cm^{-2} in FC mode and a remarkable current density of −2.68 A cm^{-2} at 1.3 V in EC mode at 650 °C, with reasonable Faradaic efficiencies. Importantly, these cells exhibited excellent operational stability in both FC and EC modes for 270 and 500 h, respectively, and maintained stability in cycling mode for 70 h. The superior performance can be attributed to the efficient mass and charge transfer properties of the high-entropy structure, as well as its ability to maintain structural integrity in humid environments.

Furthermore, in addition to equimolar high-entropy materials, there exist non-equimolar high-entropy compositions. An example is the A-site HEPO air electrode, $Ce_{0.2}Ba_{0.2}Sr_{0.2}La_{0.2}Ca_{0.2}CoO_{3-\delta}$ (CBSLCC).[224] Although it was designed with equimolar proportions, analysis through ICP and XRD reveals that CBSLCC exhibits a multiphasic structure, including a major cubic perovskite phase with cerium deficiency, designated as $Ce_{0.2-y}Ba_{0.2}Sr_{0.2-x}La_{0.2-x}Ca_{0.2}CoO_{3-\delta}$ (CD-CBSLCC), a secondary oxide phase of cerium dioxide (CeO_2) and a minor tetragonal perovskite phase of $La_{0.5}Sr_{0.5}CoO_{3-\delta}$ (LSC). The resulting three-phase heterostructures, endowed with multifunctional capabilities, effectively enhance the catalytic activity for ORR and OER under humidified air conditions for R-PCECs. Consequently, this cell achieved an exceptional fuel cell performance of 1.66 W cm^{-2} at 600 °C, alongside a high current density of −1.76 A cm^{-2} at 1.3 V and 600 °C, while demonstrating stable operation over a period of 200 hours. Moreover, several additional air electrodes can be classified as non-equimolar HEPOs including compositions such as $LnBa_{0.5}Sr_{0.5}Co_{1.5}Fe_{0.5}O_{5+\delta}$ (where Ln represents Pr, Nd, or Gd) and $Ba_{0.5}Sr_{0.5}(Co_{0.7}Fe_{0.3})_{0.6875}W_{0.3125}O_{3-\delta}$,[225] both of which exhibit structural entropy values exceeding 1.50 R. However, the design of these air electrode materials has primarily focused on investigating the effects of specific A or B-site cations, such as Pr, Nd, Gd, and W, on the overall catalytic performance of the electrodes, with comparatively less attention given to the implications of entropy variations.

Nevertheless, it is important to acknowledge that the high stability of these materials may be influenced by the inherent effects of high entropy. In contrast to the application of non-equimolar design in air electrodes, this approach is more prevalently utilized in electrolyte materials, as demonstrated by examples such as $BaSn_{0.15}Ce_{0.35}Hf_{0.25}Y_{0.1}Yb_{0.1}Ho_{0.05}O_{3-\delta}$, $BaSn_{0.16}Zr_{0.24}Ce_{0.35}Y_{0.1}Yb_{0.1}Dy_{0.05}O_{3-\delta}$, and $BaCe_{0.4}Zr_{0.4}Y_{0.15}Ni_{0.01}Cu_{0.01}Co_{0.01}Fe_{0.01}Zn_{0.01}O_3$.[226] This observation suggests that future research could benefit from the exploration of rational non-equimolar designs for high-entropy materials, as well as the investigation of the potential effects of entropy variations in non-equimolar high-entropy air electrodes.

In a word, HEPOs have gained attention for their potential as air electrodes in R-PCECs due to their multiple cation sites that enable complex atomic arrangements and extensive composition tuning, but further exploration and improvement are needed. The multi-element composition results in complex structures and compositions, making the catalytic active sites, typically formed by metal elements, complicated in the reaction processes.[227] Therefore, it is crucial to understand the factors that ensure stable HEPO formation across various crystal structures and compositions, investigate individual cation contributions to overall properties, and elucidate the relationships between crystal structure, phase, and microstructural properties and their impact on ORR and OER catalytic performance.[228] Certainly, other materials with high stability and excellent proton or oxygen ion conductivity prepared using high-entropy strategies, such as high-entropy alloy catalysts and high-entropy ceramics with fluorite, rock-salt, and spinel structure,[229] also offer valuable insights for designing triple-conducting air electrodes that better meet the requirements.

4.5. Unique Morphological Air Electrode

In addition to regulating the specific composition (such as elemental, surface, and phase composition) of air electrode materials to alter their physicochemical properties, precise control of their microstructure is also a crucial approach for further performance enhancement.[231] Specifically, the microstructure of air electrodes significantly influences their catalytic performance through the following parameters:

1) Porosity and pore size distribution: For air electrode materials, appropriate porosity enables rapid gas diffusion while maintaining pathways for electron and ion conduction. Excessive porosity may reduce the number of ion transport paths (reducing active sites), whereas insufficient porosity can decrease gas transport rates, increasing ohmic polarization resistance and lowering the electrochemical reaction rate.
2) Thickness: The thickness of the air electrode typically affects its mass transport rate. Like porosity, an overly thick air electrode can hinder gas transport to active sites, while an overly thin electrode may not provide sufficient catalytic activity and mechanical strength.
3) Particle size: Generally, smaller particle sizes after high-temperature sintering result in larger surface areas, providing more active reaction sites. However, during high-temperature calcination, electrode particles, especially nano-sized particles, may agglomerate, reducing catalytic activity. Therefore, avoiding high-temperature calcination or preventing microstructural changes of nano-sized particles in humid or CO_2 conditions is crucial for improving the stability and activity of air electrodes.

Therefore, regulating the microstructure of air electrodes requires careful attention to these critical parameters. Below, two structural optimization techniques, nano-fiber formation and three-dimensional microstructure tailoring, are discussed.

4.5.1. Nanofiber and Insert Layer Microstructure

Unlike traditional sol-gel methods for preparing cathode materials, the thin-film air electrode layers produced by electrostatic spray deposition (ESD), pulsed laser deposition (PLD), and atomic layer deposition (ALD) exhibit smaller particle sizes and higher porosity. This significantly enhances charge and ion transport pathways and improves gas diffusion, resulting in excellent oxide ion conductivity and superior power output capabilities, providing a novel approach for the fabrication of high-efficiency, low-cost air electrodes.[232]

In 2018, one-dimensional air electrode fibers composed of LSCF-$BaCe_{0.5}Zr_{0.35}Y_{0.15}O_{3-\delta}$ (BCZY) were successfully synthesized using ESD technology (**Figure 24a**).[233] These highly porous electrodes with continuous fiber microstructures and well-developed perovskite structures ranged from 90 to 150 nm in diameter (Figure 24b,c), effectively promoting gas diffusion and charge transfer processes. Subsequently, $Sm_{0.5}Sr_{0.5}CoO_{3-\delta}$ (SSC) fibers embedded with BCZY particles were also fabricated as composite air electrodes via ESD technology.[234] By electrospinning the obtained mixture with SSC solution, continuous and elongated fibers were produced, with fiber diameter of 150 to 200 nm after calcination. Single-cell measurements indicated that the fibrous composite air electrode exhibited significantly higher electrochemical properties than a typical nanocomposite electrode across the entire operating temperature range of 550 to 700 °C. Notably, the R_p of the fibrous air electrode was 0.186 $\Omega \cdot cm^2$ at 700 °C, lower than that of a conventional electrode. Moreover, ESD technology ensures the pure phase structure of the electrode at a low sintering temperature of 700 °C,[235] effectively suppressing adverse chemical reactions between the electrode and electrolyte phases at high temperatures and mitigating excessive nanoparticle grain growth. Despite the excellent porosity of nano-fiber electrodes, the physical mixing or grinding with organic binders during electrode preparation can alter the morphology of the fibers, making it challenging to preserve the original microstructure.

In addition to ESD technology, PLD technology is also extensively utilized to enhance the surface structure of air electrodes. For instance, a thin-film air electrode consisting of nanoporous LSCF combined with highly ordered, self-assembled nanocomposite layers of LSCF and $Ce_{0.9}Gd_{0.1}O_{2-\delta}$ (GDC) was developed using PLD for O-SOFCs.[236] In this heterogeneous porous nanostructure, the porous LSC layer (≈1 μm) covers the entire upper surface of the air electrode, facilitating efficient gas diffusion and providing a high surface area for ORR active sites. Simultaneously, the nanoscale stripe distribution of the LSCF-GDC nanocomposite (≈0.3 μm) offers high interfacial density,

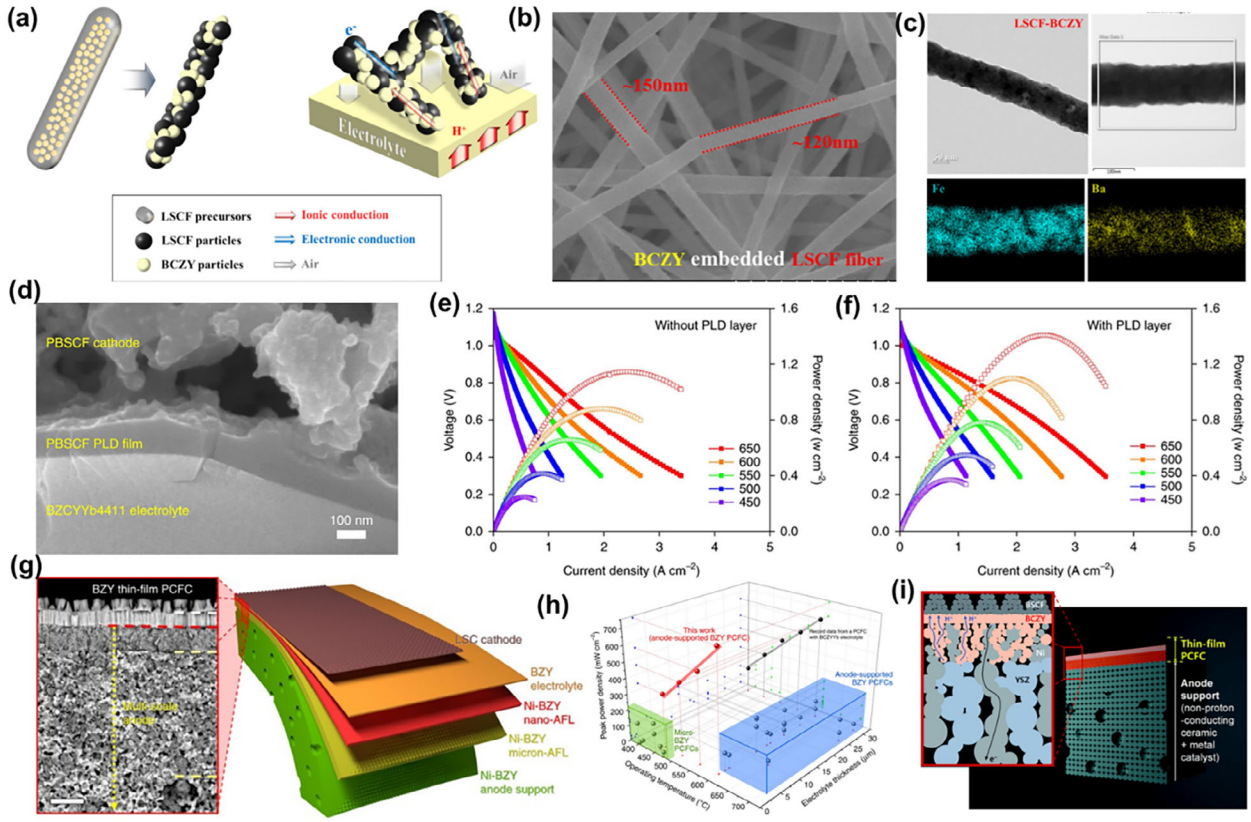

Figure 24. a) Schematic microstructures of BCZY particles embedded LSCF fiber; b) SEM and c) TEM images and element distribution of LSCF-BCZY composite electrode prepared by ESD; d) PCFC with ultra-thin PBSCF prepared by PLD; i-V-P curves of a representative cell e) without and f) with a PLD layer; g) SEM and schematic diagram of the overall microstructure of PCFC with LSC-coated composite electrode prepared by PLD technique; h) performance comparison; i) schematics of a thin-film PCFC with a non-proton-conducting ceramic matrix phase. a–c) Reproduced with permission.[233] Copyright 2018, Elsevier. d–f) Reproduced with permission.[123] Copyright 2018, Springer Nature. g,h) Reproduced with permission.[237] Copyright 2017, Springer Nature. i) Reproduced with permission.[238] Copyright 2016, Royal Society of Chemistry.

while the underlying GDC interlayer functions as a cathode buffer layer with numerous heterointerfaces. For proton-conducting fuel cells, PLD technology is also employed effectively. One notable example is the deposition of a highly active air electrode, $PrBa_{0.5}Sr_{0.5}Co_{1.5}Fe_{0.5}O_{5+\delta}$ (PBSCF), as a thin dense interlayer film between the air electrode and the electrolyte (Figure 24d–f).[123] This method significantly reduced the contact resistance caused by electrode-electrolyte mismatch and was made feasible by the proton permeability of PBSCF. The polarization behavior demonstrated exceptionally high activity for the PBSCF air electrode, with the PPD at 600 °C exceeding 800 mW cm^{-2} (Figure 24f). Another instance involves incorporating a $La_{0.6}Sr_{0.4}CoO_{3-\delta}$ air electrode into the dense electrolyte layer using PLD technology (Figure 24g–i).[237] This approach simultaneously fabricated the dense electrolyte and nano anode functional layer (nano-AFL). Due to the columnar structure tightly integrated with the nanogranular air electrode and nanoporous anode supports, the cell achieved a record high-power output performance.

Moreover, a thin-film PCFC with a total thickness of less than 10 μm was also fabricated on rigid Ni–YSZ cermet supports using PLD,[238] exhibiting promising fuel cell performance with a power output of 742 mW cm^{-2} at 650 °C.

Moreover, ALD technology is particularly well-suited for ceramic cell electrodes due to its capability of controlling deposition thickness at the atomic level to form sub-nanometer films and achieving uniform coatings on complex surfaces.[239] For instance, high-performance CoO_x active materials can be uniformly deposited onto the surface of porous PBSCF materials using ALD technology to create composite air electrode, thereby maximizing surface activity.[240] Additionally, the coated NPs can inhibit the formation of secondary phases through Ba or Sr aggregation and prevent deformation through electrostatic attraction between oxygen vacancies and cations, thus enhancing the stability of the composite electrode.

4.5.2. Three-Dimensional Microstructure

Designing unique three-dimensional (3D) morphological electrodes through structural optimization, intended to enhance gas diffusion rates and extend the TPB length, is an effective strategy to advance the oxygen reaction process and enhance low-temperature kinetics.[241]

Inspired by the advantages of highly porous electrodes and the exceptional performance of $PrBa_{0.5}Sr_{0.5}Co_{2-x}Fe_xO_{5+\delta}$ ($PBSCF_x$),

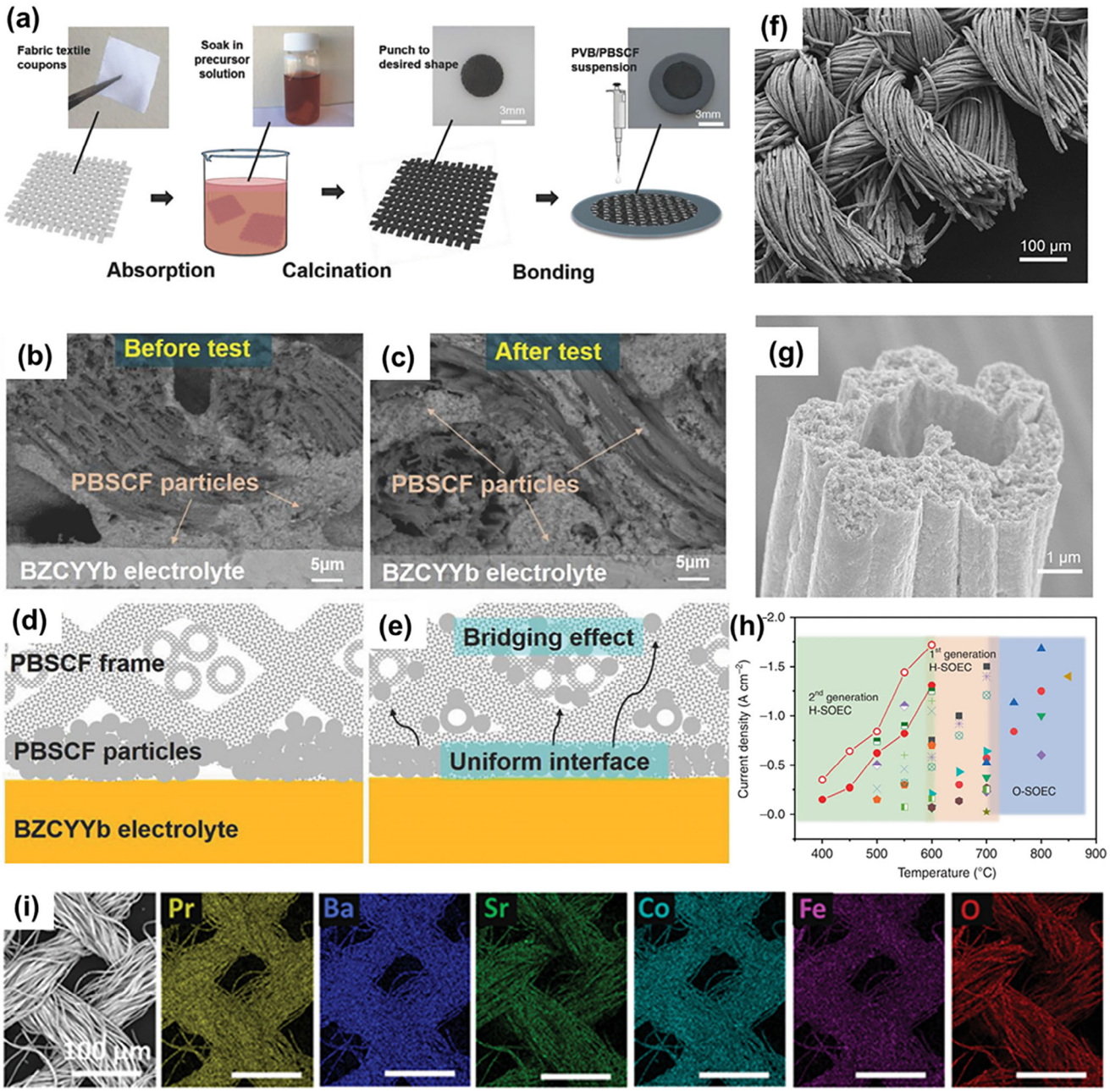

Figure 25. a) Processes for fabricating SAUP 3D PBSCF textile steam electrode; SEM image near steam electrode/electrolyte interface (b) before and (c) after steam electrolysis; schematic diagrams of steam electrode/electrolyte interface before (d) and (e) after electrolysis present the interface reorganization bridging process; f,g) SEM images of the electrode mesh with different magnification; h) performance comparison of representative FCs at electrolysis voltage of 1.4 V; (i) elemental distribution in EC-800 sample. a–e) Reproduced with permission.[242] Copyright (2018), Wiley. f–h) Reproduced with permission.[19d] Copyright (2018), Springer Nature. i) Reproduced with permission.[243] Copyright (2021), Wiley.

a self-architecture ultra-porous (SAUP) 3D air electrode using $PBSCF_x$ materials was developed for water splitting (**Figure 25a–e**).[242] The ceramic framework was created through a template-derived and self-architecture process (Figure 25a). A fabric textile was immersed in the $PBSCF_x$ precursor solution overnight, followed by firing at 750 °C for 4 hours to form the $PBSCF_x$ ceramic textile. Subsequently, the punched ceramic textile coupon was affixed to the top of a prepared half-cell and co-sintered at 750 °C for 2 hours. The textile-like microstructure (Figure 25b–e), consisting of bundles of fibers, provides the framework with sufficient mechanical strength and flexibility compared to randomly aligned nanofiber electrodes, as well as adequate porosity (57.7%) to ensure fast mass transfer and an enlarged surface area for steam electrolysis reactions. This enhancement enables the 3D $PBSCF_x$ air electrode to exhibit significant electrolytic performance of about -0.54 A cm^{-2} at 1.6 V

(500°C), surpassing the regular PBSCF counterpart electrode. Furthermore, the electrolysis current of PCEC with the SAUP 3D air electrode showed no degradation during the entire 78-hour steam electrolysis process, attributed to the bridging effect between electrode fibers and interface reorganization. Similarly, the triple-conducting air electrode $PrNi_{0.5}Co_{0.5}O_{3-\delta}$ (PNC) perovskite was developed as an R-PCEC air electrode with an SAUP 3D microstructure (Figure 25f,g).[19d] Each bundle consists of hollow PNC fibers with through holes (≈3 µm in diameter) to facilitate gas diffusion across the nanoparticle-structured surface where reactions occur. Each fiber comprises nanoparticles ranging from 20 to 50 nm. Incorporating this nanostructured electrode into the cell resulted in higher performance, evidenced by an increase in electrolysis current density from 0.85 A cm^{-2} (regular PNC) to 1.18 A cm^{-2} at 1.3 V at 600°C, as well as a 15.7% increase in PPD (Figure 25h).

However, while the high porosity of the air electrode structure facilitates the generation and migration of O_{ad}- from catalytic sites to triple-phase boundaries, excessive porosity can lead to a loss in surface area, affecting charge transfer in mixed ionic and electronic conducting electrodes. Inspired by this, phase field modeling and experimental verification were conducted to analyze charge and mass transfer inside the 3D-engineered PBSCF air electrode (Figure 25i).[243] By calcining the fabricated PBSCF with a 3D microstructure at different temperatures (700, 800, 900 °C), varying porosities and morphologies of the air electrode were obtained. According to actual electrochemical performance results, the EC-800 sample (fabricated at 800°C) achieved the best performance with a porosity of 52.1% and average particle size of around 80 µm, aligning with phase field simulation results. These findings suggest that the balance of charge and mass transfer is best achieved at 800°C, resulting in the highest oxygen ion generation rate and performance. Similarly, another TCO air electrode, BCFZY, exhibited comparable results. Ion beam-scanning electron microscopy indicates that BCFZY prepared at 800 °C shows the largest specific surface area and air electrode/electrolyte contact area, leading to more catalytically active sites and the best electrochemical performance.[244]

3D microstructure tailoring has shown significant potential by improving surface properties compared to conventional air electrodes. However, it is important to note that these 3D microstructure electrodes typically consist of porous materials, which often exhibit reduced mechanical strength. Issues such as breakage and distortion are significant concerns. Therefore, maintaining the morphology and electrochemical stability of these air electrodes remains a substantial challenge.

4.6. Robust Air Electrode–Electrolyte Interface

To achieve the excellent electrochemical performance of R-PCECs, it is crucial to not only adjust the composition and structure of the air electrode but also to enhance the interface between the air electrode and the electrolyte.[245] Since the ORR/OER in the air electrode requires sufficient proton transfer from/to the electrolyte, increasing the contact area between the electrode and electrolyte provides more pathways for proton transport. Additionally, mismatched thermal expansion properties between most air electrodes (specifically for Co-based materials) and electrolytes often result in poor interfacial contact, leading to issues such as delamination and peeling. These issues significantly increase contact resistance and reduce mechanical strength, thereby diminishing the overall catalytic activity and lifespan of the cell. Improving the surface properties of the electrolyte and introducing functional layers between the electrolyte and air electrode are current key strategies for enhancing the interface.

A robust interface can be achieved by acid-treating the electrolyte surface (**Figure 26a–e**). Specifically, the electrolyte surface of the co-sintered hydrogen electrode-electrolyte bilayer undergoes nitric acid treatment before bonding with the oxygen electrode.[246] This etching process removes surface impurities and creates a roughened texture (increasing surface roughness from 0.28 to 0.77 µm) (Figure 26a–d), thereby enhancing bonding and adhesion between the electrolyte and oxygen electrode, as well as removing segregating elements and promoting atomic-scale diffusion and reactions at the interface. These enhancements lead to increased mechanical strength (as evidenced by an increase in peeling strength from 18.6 N for the untreated to 23.5 N for the 10-minute treated sample) (Figure 26e), restored proton conductivity (as confirmed by conductivity measurements), and improved electrochemical efficiency (fuel efficiencies exceeding 98% for all measured cells). These results lead to superior electrochemical performance in both FC and EC modes for R-PCECs, with a PPD of 300 mW cm^{-2} at a low temperature of 350 °C and stable electrolysis operations with current densities above 3.9 A cm^{-2} at 1.4 V. Additionally, a chevron-shaped electrolyte was successfully fabricated using a novel imprinting-assisted transfer technique (Figure 26f–h), as confirmed by SEM and EDX images.[247] Compared to traditional flat cells, the micropatterned cells exhibit over a 40% increase in electrode-electrolyte interface areas and more electrochemical reaction sites, significantly enhancing performance in both fuel cell (with an increase of over 45%) and electrolysis cell (with an increase of 30%) modes. However, these methods also have limitations. For instance, the nitric acid treatment necessitates precise regulation of key parameters, such as treatment duration, the contact area with the electrolyte surface, and acid concentration. Inadequate control of these factors may result in localized overconsumption of electrolyte, leading to leakage issues.

4.7. Machine Learning and Kinetics Simulations for Air Electrodes

In the development of novel air electrode oxides, the vast number of potential material combinations makes traditional experimental approaches—characterized by high costs, labor intensiveness, and trial-and-error processes—resource-demanding and time-consuming. Recently, the application of machine learning (ML) in materials science has gained momentum, offering significant potential to accelerate material discovery, reduce experimental costs, and optimize material design.[248] By applying ML algorithms to large datasets, researchers can uncover correlations between composition, structure, and performance, enabling the identification of optimal material combinations from numerous candidates.

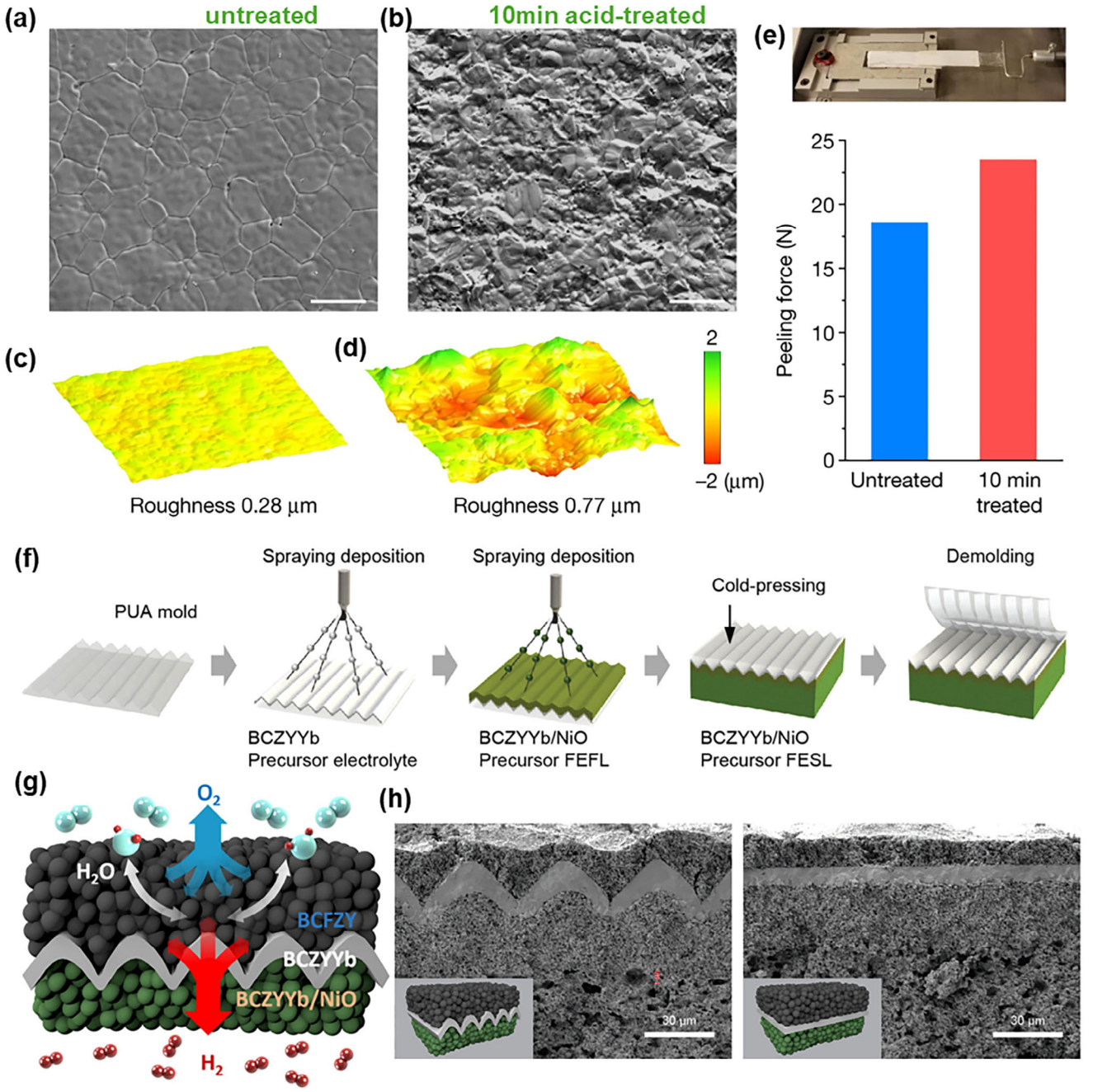

Figure 26. SEM images for a) untreated and b) 10-min treated electrolyte surface; c) atomic force microscope for the untreated (c) and 10-min treated d) electrolyte surface; e) peeling strength of air electrode–electrolyte interface (lower panel); Schematic illustration of the f) fabrication processes by the imprinting-assisted transfer technique and g) its working mechanism; h) the SEM image of patterned (left) and flat (right) R-PCECs. a–e) Reproduced with permission.[246] Copyright 2022, Springer Nature. f–h) Reproduced with permission.[247] Copyright 2022, American Chemical Society.

However, the application of ML to predict the catalytic performance of perovskite materials is still in its early stages. Few studies have employed ML to predict key properties such as ASR and oxygen conductivity. Traditionally, descriptors like the oxygen p-band center, derived from DFT calculations, have been used to establish relationships between various perovskite properties, such as oxygen surface exchange rates and electron work functions. While useful, these correlations are based on a relatively simple ML model that relies on moderately costly DFT computations, limiting the speed at which new materials can be proposed or property trends understood.[249] As a result, there is a need to explore more advanced data-driven approaches, such as ML, to facilitate the discovery of high-performance air electrode materials.

A recent study by Ni and colleagues used a dataset of 85 ASR values, a neural network-based ML model, elemental features, and a newly proposed ion Lewis's acidity (ISA) descriptor to

screen for promising new perovskite air electrode materials.[250] They screened 6,871 possible compositions and identified four materials with low predicted ASR values. Subsequent experimental validation confirmed that one of the ML-screened materials, $Sr_{0.9}Cs_{0.1}Co_{0.9}Nb_{0.1}O_3$ (SCCN), exhibited superior ORR catalytic activity, with the lowest ASR value (0.01 Ω cm^2 @ 700 °C).

ML models for ASR prediction have also been developed and evaluated. For example, by incorporating elemental features, one-hot encoding of electrolyte types, and a separate ML model predicting ASR activation energy barriers as input, a more accurate ASR prediction model was developed.[249a] This approach enabled low-error predictions and allowed for temperature-dependent ASR forecasts. This model was subsequently employed to explore a large compositional space of approximately 19 million perovskites, identifying $BaFe_{0.75}Cu_{0.125}Zr_{0.125}O_3$ ($1.15/kg, log(ASR) = 0.12 Ω cm^2 @ 500 °C), $BaFe_{0.5}Co_{0.25}Mo_{0.25}O_3$ (18.0 meV/atom, log(ASR) = -0.02 Ω cm^2 @ 500 °C), and $SrCo_{0.75}Nb_{0.125}Ta_{0.125}O_3$ (SCNT) (log(ASR) = -0.43 Ω cm^2 @ 500 °C) as the most cost-effective, stable, and active materials, respectively. The model demonstrated strong predictive capability for identifying promising materials based on time-cross validation.

Accurately measuring the intrinsic oxygen ion and proton conductivities of air electrodes remains challenging, as these values are significantly lower than electronic conductivity. While existing methods, such as hydrogen/oxygen permeation tests using palladium membranes, secondary ion mass spectrometry (SIMS), and conductivity relaxation techniques, have been employed to characterize ionic conductivity, they come with limitations related to equipment, experimental procedures, and the intrinsic ionic transport properties of materials.[251] ML techniques present a potential solution to these challenges. For instance, in 2021, a machine learning model based on the XG-Boost algorithm was successfully developed to predict the conductivity of 97625 perovskite oxides under various temperatures and environmental conditions, such as in humid (3% H_2O) hydrogen and humid air.[252] These oxides were classified into H^+ conductors, O^{2-} conductors, H^+/e^- conductors, and O^{2-}/e^- conductors, as illustrated in **Figure 27**a,b.

In addition to direct predictions of proton conductivity, proton-conducting ability can also be inferred from a material's hydration capability. Since hydrated proton concentration (HPC) is a critical factor in determining proton conductivity, a random forest (RF)-based ML model was successfully employed to predict HPC for 3,200 air electrode materials across the 50–700 °C temperature range,[253] as shown in Figure 27c. The results indicated that (La,Ca/Ba)(Co,Ni/Fe/Mn/Zn/Cu)O_3 oxides containing Co, Ni, or Cu in the B-site showed good performance, with Ni demonstrating superior performance. Furthermore, Ca as the A-site element had a more significant influence than Ba in the 400–500 °C range. The optimal composition, $(La_{0.7}Ca_{0.3})(Co_{0.8}Ni_{0.2})O_3$ (LCCN7382), was identified, exhibiting excellent electrochemical performance, with a peak power density of 719 mW cm^{-2} at 650 °C in fuel cell mode and a current density of 1420 mA cm^{-2} at 1.3 V in electrolysis mode.

While ML presents numerous advantages in materials science, several challenges remain in using ML to develop high-performance TCO air electrode materials for R-PCECs. A key obstacle is the availability and quality of data required for training ML models. The reliability of predictions depends heavily on data quality; however, it is resource-intensive and costly to gather and manage these specialized datasets. Issues such as data inconsistency, errors, and missing values further complicate the process. Additionally, the complex and diverse physicochemical properties of materials often involve multiple descriptors that impact performance simultaneously. Accurately translating these key descriptors into inputs for ML algorithms and ensuring they are interpreted correctly is a significant challenge. Furthermore, while ML models can generate valuable predictions and insights, experimental validation is essential to confirm and refine these findings. Aligning computational predictions with experimental results can be difficult, given the experimental constraints, limitations, and uncertainties that must be considered in practice.

In the context of R-PCEC air electrode reactions, kinetic simulations play an essential role in elucidating reaction mechanisms and enhancing electrode design. By conducting microscopic-scale simulations of electrode kinetics, one can examine processes such as the adsorption of oxygen and vapor, the formation and migration of oxygen ion and proton defects, as well as electron transport within the air electrode kinetics. When integrated with DFT calculations, the energy requirements for each of these processes along different paths (e.g., surface and bulk, different crystal planes, various metal ions) can be quantitatively assessed. This approach facilitates the identification of optimal reaction pathways (which require minimal energy) and the kinetic processes that can ameliorate rate-limiting steps (lowering energy demands). For example, through molecular dynamics (MD) simulations and ab initio calculations, crucial data regarding hydration energies, oxygen vacancy formation energies, defect formation energies, and proton transfer barriers for various co-substituted $BaFeO_{3-\delta}$ air electrodes were obtained, which ultimately guided the selection of the optimal composition, $Ba_{0.875}Fe_{0.875}Zr_{0.125}O_{3-\delta}$, for air electrodes.[70b]

In contrast to MD, Kinetic Monte Carlo (KMC) represents a stochastic approach that generates a series of microscopic states without the need to consider the equations governing particle motion.[254] This characteristic enables the execution of larger time steps in KMC modeling, which has been widely adopted in SOC technology to investigate ion diffusion kinetics and associated mechanisms. Furthermore, diffusion simulations of the proton-conducting $BaZr_{0.8}Y_{0.2}O_{3-\delta}$ system utilizing KMC methodology were performed, considering various local configurations of Y on the Zr sites.[255] The findings indicated that protons are more frequently located in clusters containing a minimum of three YO_6 units, and the proton transfer energies derived from the nudged elastic band (NEB) method corroborated favorable percolation and elevated proton conductivity in Y-doped $BaZrO_{3-\delta}$. Analogously, by integrating KMC with DFT theoretical calculations, diverse 1D, 2D, and 3D Y superstructures in $BaZr_{0.8}Y_{0.2}O_{3-\delta}$ were successfully simulated,[256] thereby elucidating the correlation between average proton mobility and doping concentrations.

Recently, a comprehensive array of perovskite oxides was constructed as candidates for air electrodes in protonic ceramic cells, achieved by selecting three A-site ions (Ba, Sr, $Pr_{0.5}Ba_{0.5}$) and combining them with five catalytically active B-site ions (Mn, Fe,

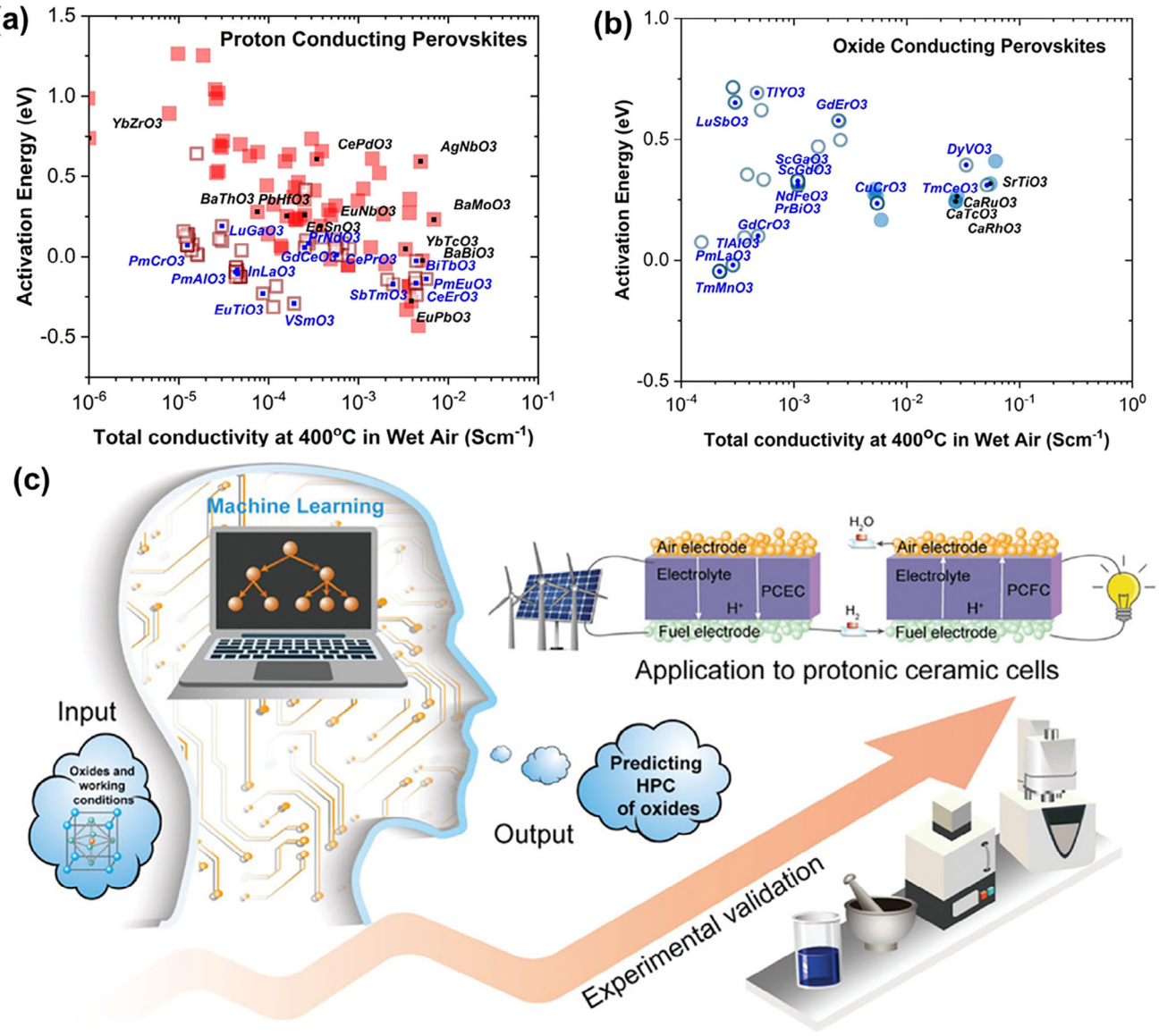

Figure 27. The predicted a) proton-conducting and b) oxide-conducting oxides in wet air based on eXtreme Gradient Boosting (XGBoost) model; c) research process illustration of screening air electrode with high HPC by ML model. a,b) Reproduced with permission.[252] Copyright 2021, Springer Nature. c) Reproduced with permission.[253] Copyright 2022, Wiley.

Co, Ni, Cu), in addition to 37 distinct B-site dopants.[257] Notably, the optimal elemental distribution for each candidate was determined through molecular dynamics–Monte Carlo (MD–MC) simulations. The E_{hull} value, a pivotal descriptor of thermodynamic stability, was established through structural relaxation and static calculations. To prevent excessive reliance on E_{hull} values, which could potentially bias assessments of material stability, a data-driven material analysis method termed decomposition analysis (DA) was proposed. Subsequent refinement through DA and experimental validation culminated in the identification of a highly durable composite air electrode, $PrBaCo_{1.9}Hf_{0.1}O_{5+\delta}$, which demonstrates exceptionally high electrocatalytic activity.

5. The Electrochemical Performance of Current Air Electrodes

5.1. Symmetrical Cell Performance

To facilitate a more direct comparison of the catalytic activities of different air electrodes, we have compiled electrochemical performance data from recent studies on symmetric cells based on proton-conducting materials and advanced air electrodes. This approach ensures a more accurate assessment of the intrinsic properties of these electrodes since it mitigates the performance variations of other components.

Our analysis focuses on the most advanced triple-conducting air electrodes developed over the past five years, providing insights into the current status of air electrode technology for R-PCECs. As shown in **Table 1** and **Figure 28a**, ≈50% of air electrodes tested at 550 °C in wet air exhibit ASR values between 0.40 and 0.80 Ω·cm^2, while 20% display values below 0.40 Ω·cm^2, and the remaining 30% show poorer performance with ASR values exceeding 0.80 Ω·cm^2. The lowest ASR, recorded at 0.21 Ω·cm^2, was observed in BLCF0.95, a single perovskite oxide with B-site deficiency coupled with A-site La doping. Similar low ASR values were reported for BSTC, BCFZY-Ag, and BCFZYMg oxides, which achieved 0.29, 0.24, and 0.26 Ω·cm^2, respectively. Moreover, the evaluation of electrode materials reveals a notable correlation between Co content and ASR values. Specifically, electrodes with elevated Co concentrations, such as BSTC, BCFZY-Ag, BCFZY-Mg, BCT20, PNC73, and BSGC-BSPY, exhibit significantly lower ASR values than their counterparts. Conversely, Co-free Fe or Ni-based materials demonstrate inferior electrochemical performance. For instance, materials such as NSTF0.3, U-BFZ-NM, P2.7NCNO, PSFN/Fe_2O_3, D-SFN, PBF-06Y_2O_3, and BLFZ0.95 consistently present ASR values above 0.70 Ω·cm^2 at 550 °C, reaching a maximum of 6.43 Ω·cm^2. Additionally, the phase composition of these electrode materials plays a critical role in their electrocatalytic activity. Pure single-phase electrodes or nanocomposite materials characterized by surface-exsolved nanoparticles (or secondary phases) demonstrate enhanced electrocatalytic properties. In contrast, conventional mechanically mixed composites, such as PSFN/Fe_2O_3, 2W-PBSCF, BCFN-BZCYY, LBSCF-BZCY, BZFN-BZCY, BSGC-BCPY, and SSC-SBC, exhibit suboptimal electrochemical performance, with ASR values predominantly surpassing 1.0 Ω·cm^2 at 550 °C. This indicates that the microstructural and compositional characteristics of the electrode materials are paramount in determining their electrochemical efficacy.

However, as illustrated in Table 1 and Figure 28b, limited ASR data are available for temperatures below 550 °C, particularly at 450 °C or even lower, likely due to the significant decline in catalytic performance at lower temperatures. In the reported 2024 studies, only two oxides-BSTC and N-BCFZYN-showed ASR values at 450 °C, measuring 1.87 and 4.78 Ω·cm^2, respectively. Despite the substantial improvement in air electrode performance over the past 5 years through various modification strategies in the 650–550 °C range, further research is required to elucidate the rate-limiting steps in the reaction kinetics at even lower operating temperatures. This would be crucial for enhancing ORR/OER catalytic performance in air electrodes under reduced temperature conditions.

Air electrode stability is another critical factor in advancing R-PCEC technology. **Table 2** and Figure 28c summarize degradation rates (DR) for advanced air electrodes tested in wet air, reflecting the real operational conditions. Notably, novel HE-PBSLCC and BC1.5MN air electrodes demonstrated low DR, ≈1.0×10^{-4} Ω·cm^2·h^{-1}, in steam-containing environments (up to 20%) at 550 °C. In contrast, conventional single-phase and composite air electrodes, such as PBC, LSCF, PBSC, and BB-PC, exhibited much higher DR, exceeding 12.0×10^{-4} Ω·cm^2·h^{-1}. Moreover, the comparative analysis of air electrodes fabricated via the BB-OPS and BB-PC reveals a notable disparity in their performance decay rates. Specifically, the BB-OPS electrodes exhibit a remarkably reduced decay rate, decreasing from 27.2 to 4.9 $\times 10^{-4}$ Ω·cm^2·h^{-1}, whereas the BB-PC electrodes demonstrate a more pronounced degradation. This disparity underscores the superiority of the one-pot self-assembly technique in mitigating performance degradation, thereby enhancing the overall efficacy and durability of the air electrodes. Moreover, regarding PNC air electrodes, the application of the SAUP method, compared to the conventional glycine-citrate combustion method, significantly enhances both porosity and the distribution of nanoparticles. This enhancement results in a marked reduction in the ASR value, which decreases from 0.13 to 0.055 Ω cm^2 at 500 °C (single cell). Indeed, there are circumstances in which the performance of electrode materials synthesized through different methodologies is comparable. For instance, the ASR values of NiO-BCFZY electrodes fabricated via both the impregnation method and in situ exsolution are found to be ≈0.36 Ω·cm^2 at 550 °C. This parity in performance can also be ascribed to several factors, including the specific quantity of impregnation utilized and the extent of A-site defects present in the nanoparticles generated during the fabrication process.

A significant concern is the lack of sufficient data on air electrode stability under conditions of high steam pressure. As previously mentioned, higher water vapor pressure is often required for air electrodes, as it promotes proton conductivity, thereby enhancing ORR/OER catalytic activity. Additionally, when air electrodes operate in electrolysis mode, elevated water vapor pressure tends to improve Faradaic efficiency and hydrogen production rates. While some air electrode materials exhibit good proton uptake capacity, they are prone to phase segregation under high water vapor pressure, which can adversely impact their overall catalytic performance. Future research should prioritize investigating the stability of air electrode materials in high-moisture environments, focusing on factors such as phase structure, surface chemistry, and catalytic behavior.

5.2. Electrochemical Cell Performance

To comprehensively assess the electrocatalytic activity of air electrodes under practical operating conditions, this review compiles and analyzes the electrochemical performance of representative air-electrode-based R-PCECs in FC, EC, and reversible modes. It is important to recognize that actual electrochemical performance is influenced by various factors, including other cell components such as fuel electrode materials, electrolyte composition and thickness, and operational environmental conditions. Therefore, relevant experimental parameters are provided in the analysis.

In FC mode (**Figure 29a** and **Table 3**), R-PCECs exhibit favorable electrochemical output within the operating temperature range of 650 °C to 450 °C, regardless of whether the air electrode operates in dry or humid (up to 10% H_2O) air. For instance, at 550 °C, ≈41% of R-PCECs report peak power densities (PPDs) exceeding 0.60 W cm^{-2}, while around 90% of them achieve PPDs above 0.30 W cm^{-2}, indicating that the ORR catalytic activity of these air electrodes is sufficiently high at or above 550°C. However, at lower temperatures, such as 350 and 400 °C, performance data are scarce, and the PPDs of advanced air electrodes often fall below 0.35 W cm^{-2}. This decline is largely attributed to the

Table 1. The ASR values of advanced air electrodes based on proton-conducting symmetrical cells in wet air at 450–650 °C.

Air Electrodes	Electrolyte	Atmosphere	ASRs [Ω cm^2]					Refs.
			650 °C	600 °C	550 °C	500 °C	450 °C	
NSTF0.3	BZCYYb1711	5%H_2O–air	0.19	0.33	0.77	1.82	/	[258]
PCNCFO- PBC	BZCYYb1711	3%H_2O–air	0.09	0.18	0.43	1.20	/	[175]
SCM- BCFZY	BZY0.15	3%H_2O–air	/	0.18	/	/	/	[259]
C/H-BSCF	BZCYYb1711	3%H_2O–air	0.11	0.26	0.68	2.13	/	[260]
U-BFZ-NM	BZCYYb1711	3%H2O–air	0.38	1.03	2.71	/	/	[261]
CBSLCC	BZCYYb1711	3%H2O–air	/	0.23	/	1.65	/	[224]
BCFT10	BZCYYb1711	3%H_2O–air	0.12	0.24	0.51	1.28	/	[262]
BSCFEr0.1	BZCYYb1711	5%H_2O–air	0.10	0.16	0.32	0.70	/	[263]
BSTC	BZCYYb4411	3%H_2O–air	0.08	0.15	0.29	0.56	1.29	[264]
PNCO64	BZCYYb1711	3%H_2O–air	0.12	0.27	0.73	2.31	/	[265]
N-BCFZYNF	BZCYYb1711	3%H_2O–air	0.08	0.17	0.41	1.34	4.78	[208]
PBCCHf0.1	BZCYYb1711	3%H_2O–air	0.11	0.27	0.55	/	/	[266]
P2.7NCNO	BZCYYb1711	3%H_2O–air	0.10	0.25	0.67	/	/	[267]
PBCCPd	BZCYYb1711	3%H_2O–air	0.11	0.26	0.62	1.82	/	[268]
PSFN/Fe_2O_3	BZCYYb1711	3%H_2O–air	0.16	0.35	0.92	2.66	/	[269]
D-SFN	BZCYYb1711	3%H_2O–air	0.15	0.40	1.21	4.81	/	[138]
PBF-06Y_2O_3	BZCYYb1711	Wet air	0.79	2.65	6.43	/	/	[178]
BLFZ0.95	BZCYYb1711	Wet air	0.07	0.12	0.21	/	/	[71b]
2W-PBSCF	BZCYYb1711	3%H_2O–air	0.24	0.36	0.80	1.39	/	[270]
PCO-LSCF	BZCYYb4411	3%H_2O–air	0.14	0.32	0.79	/	/	[271]
HE-PBSLCC	BZCYYb1711	3%H_2O–air	0.12	0.26	0.75	2.13	/	[223]
PBCsC	BZCYYb1711	3%H_2O–air	0.16	0.28	0.53	1.53		[272]
PNCO-64	BZCYYb1711	3%H_2O–air	0.14	0.34	0.82	/	/	[273]
BCFN-BZCYY	BZCYYb1711	3%H_2O–air	0.71	2.20	6.64	/	/	[274]
BSCFC	BZCYYb1711	3%H_2O–air	0.10	0.23	0.53	1.37	4.37	[112]
BCZY	BZCYYb1711	3%H_2O–air	0.15	0.25	0.56	1.42	/	[191]
PNC-BCPY	BZYb82	3%H_2O–air	0.06	0.18	0.49	/	/	[173]
BCFNS	BZCYYb1711	3%H_2O–air	0.08	0.23	0.51	1.80	/	[275]
BSCFN-F0.1	BZCYYb1711	Wet air	0.11	0.23	0.53	1.51	5.11	[276]
LBSCF-BZCY	BZCY352	3%H_2O–air	0.12	0.42	1.53	/	/	[277]
BCCFYb	BZCYYb1711	2.5%H_2O–air	0.08	0.26	0.68	2.23	/	[278]
NBSCFN5	BZCYYb1711	3%H_2O–air	0.71	1.58	4.26	11.33	/	[279]
BCT20	BZCYYb4411	3%H_2O–air	0.12	0.23	0.39	0.65	1.20	[280]
PBCFN	BZCYYb1711	Wet air	0.23	0.80	/	/	/	[198]
BCYF	BZCYYb1711	5%H_2O–air	0.60	1.02	1.88	3.85	8.40	[194]
BCFZY-Ag	BZCYYb1711	3%H_2O–air	0.06	0.11	0.24	0.59	1.83	[202]
BCFZYMg	BZCYYb1711	3%H_2O–air	0.06	0.14	0.26	0.48	1.17	[118b]
BC1.5MN	BZCYYb1711	3%H_2O–air	0.13	0.24	0.47	1.08	3.26	[203]
PLNBSCC	BZCYYb1711	5%H_2O–air	0.16	0.35	0.81	2.09	/	[222]
PNC73	BZCYYb4411	3%H_2O-O_2	/	0.12	0.30	0.87	2.82	[281]
BGPC	BZCYYb1711	3%H_2O–air	0.14	0.27	0.67	1.88	/	[282]
BCFZnY	BZCYYb1711	5%H_2O–air	0.13	0.19	0.29	0.57	1.55	[39]
BSCFP0.05	BZCYYb1711	5%H_2O–air	0.24	0.38	0.66	1.53	/	[283]
BZFN-BZCY	BZCY172	Wet air	0.81	1.98	5.66	/	/	[284]
BB-OPS	BZCYYb1711	5%H_2O–air	0.09	0.16	0.30	0.66	/	[285]
D-BFZ	BZCYYb1711	3%H_2O–air	0.11	0.23	0.51	1.32	/	[70b]
BCO-LSCF	BZCYYb1711	3%H_2O–air	0.08	0.17	0.37	0.84	/	[168]
SCFN	BZCYYb1711	3%H_2O–air	0.08	0.20	0.58	1.98	8.35	[205]

(*Continued*)

Table 1. (Continued)

Air Electrodes	Electrolyte	Atmosphere	ASRs [Ω cm^2]					Refs.
			650 °C	600 °C	550 °C	500 °C	450 °C	
BCFZYMn	BZCYYb1711	5%H_2O–air	0.15	0.35	1.04	2.34	/	[117]
PBCC	BZCYYb1711	3%H_2O–air	0.05	0.24	0.51	1.33	/	[197b]
LSCF2.7	BZCY172	Wet air	0.20	0.44	1.14	3.76	/	[286]
NiO-BCFZY	BZCYYb1711	Wet air	/	0.15	0.35	0.96	/	[174]
BSGC5124	BCY82	3%H_2O–air	0.52	0.81	1.36	2.13	3.12	[287]
BSGC-BCPY	BCY82	3%H_2O–air	0.12	0.20	0.31	0.52	1.13	[287]
GCCCO	BZCYYb1711	3%H_2O–air	0.63	0.92	1.36	2.14	4.06	[288]
PBCC95	BZCYYb4411	3%H_2O–air	/	0.15	0.39	1.06	/	[289]
SSC-SBC	BZCYYb1711	Wet air	0.35	/	/	/	/	[157]
SCFZ	BZCYYb1711	Wet air	0.15	0.38	1.01	2.42	/	[290]
BCCY	BZCYYb1711	2.5%H_2O–air	0.08	0.25	0.49	1.40	4.76	[190]
BSSNC	BZCY172	3%H_2O–air	0.25	0.66	1.52	4.21	/	[291]
LBCO	BZY91	3%H_2O–air	/	0.15	0.32	0.72	1.87	[78]
BCFZY	BZCYYb1711	Wet air	0.35	0.62	1.05	1.83	/	[115]
BCFZ	BZCYYb1711	3%H_2O–air	0.60	1.02	1.88	3.85	8.40	[114]
PBC	BZCY172	Wet air	0.31	0.73	1.67	4.68	/	[292]

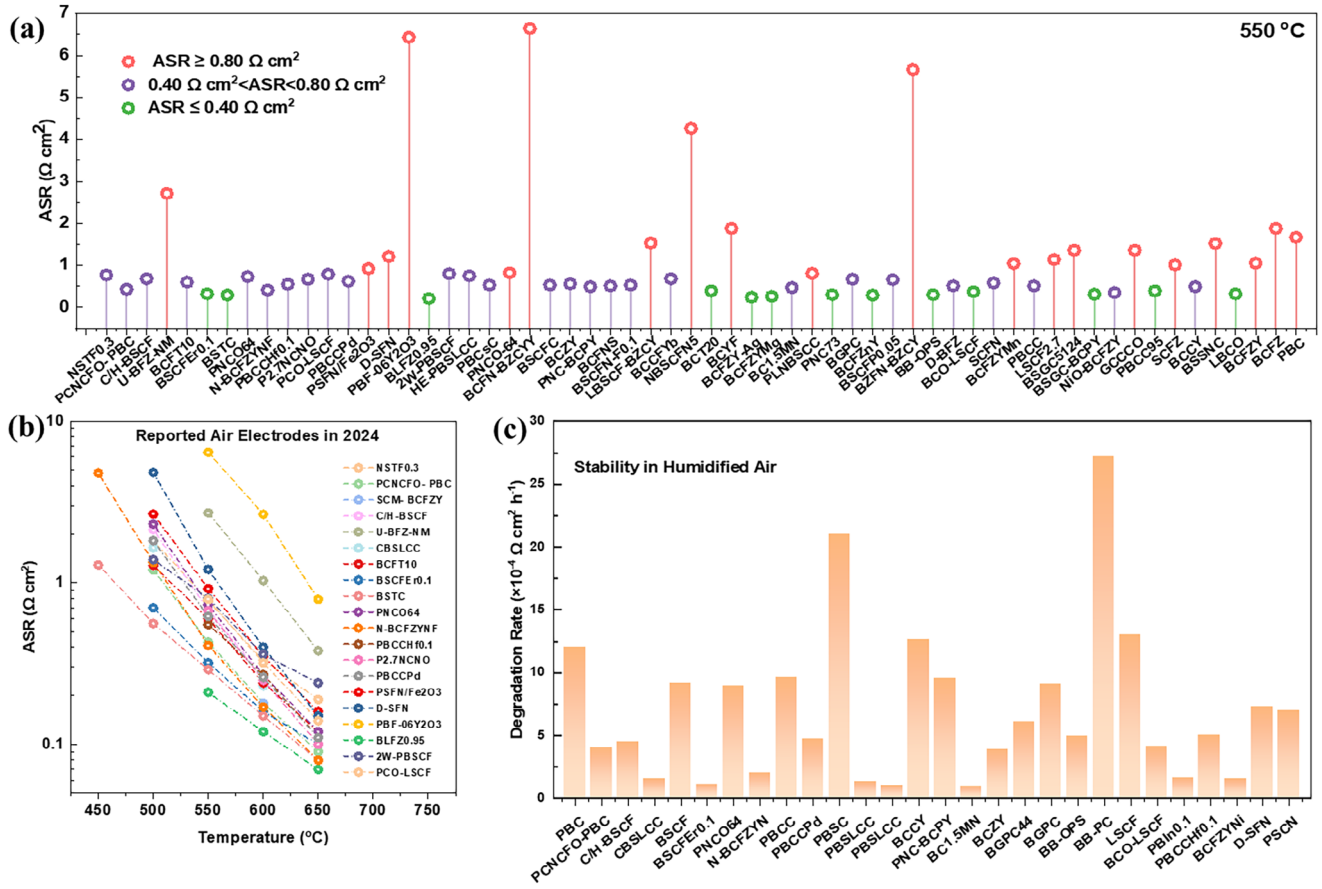

Figure 28. a) The summarized ASR values of air electrodes tested at 550 °C in wet air; b) the ASR values of reported air electrodes in 2024, evaluated across the temperature range of 650 to 450 °C; c) the degradation rates (DR) of various air electrodes in wet air conditions.

Table 2. Degradation rates of air electrodes in humidified air at different operation durations.

Air electrodes	Degradation rate [$\times 10^{-4}$ Ω cm^2 h^{-1}]	Temperature [°C]	Atmosphere	Operation time [h]
PBC	12	600	3%H_2O–air	100
PCNCFO-PBC	4.0	600	3%H_2O–air	100
C/H-BSCF	4.5	550	3%H_2O–air	300
CBSLCC	1.5	600	3%H_2O–air	200
BSCF	9.2	600	5%H_2O–air	240
BSCFEr0.1	1.1	600	5%H_2O–air	380
PNCO64	8.9	600	3%H_2O–air	74
N-BCZYN	2.0	550	3%H_2O–air	300
PBCC	9.6	600	3%H_2O–air	100
PBCCPd	4.7	600	3%H_2O–air	130
PBSC	21.0	550	3%H_2O–air	300
HE-PBSLCC	1.3	550	3%H_2O–air	600
HE-PBSLCC	1.0	550	20%H_2O–air	400
BCZY	3.9	600	3%H_2O–air	206
BCCY	12.6	600	3%H_2O–air	206
PNC-BCPY	9.5	550	3%H_2O–air	210
BC1.5MN	0.9	550	3%H_2O–air	455
BGPC44	6.1	600	3%H_2O–air	100
BGPC	9.1	600	3%H_2O–air	100
BB-OPS	4.9	600	3%H_2O–air	120
BB-PC	27.2	600	3%H_2O–air	120
LSCF	13	600	10%-30%H_2O–air	500
BCO-LSCF	4.1	600	10%-30%H_2O–air	500
PSCN	7.0	600	3%H_2O–air	100
PBIn0.1	1.6	600	3%H_2O–air	200
PBCCHf0.1	5.0	600	3%H_2O–air	100
BCFNYNi	1.5	550	3%H_2O–air	200
D-SFN	7.3	550	3%H_2O–air	150

Electrolytes: BZCYYb1711: $BaZr_{0.1}Ce_{0.7}Y_{0.1}Yb_{0.1}O_{3-\delta}$; BZY0.15: $BaZr_{0.85}Y_{0.15}O_{3-\delta}$; BZYb82: $BaZr_{0.8}Yb_{0.2}O_{3-\delta}$; BZCY352: $BaZr_{0.3}Ce_{0.5}Y_{0.2}O_{3-\delta}$; BZCY172: $BaZr_{0.1}Ce_{0.7}Y_{0.2}O_{3-\delta}$; BZY91: $BaZr_{0.9}Yb_{0.1}O_{3-\delta}$; BCY82; $BaCe_{0.8}Y_{0.2}O_{3-\delta}$. Air Electrodes: NSTF0.3: $Na_{0.3}Sr_{0.7}Ti_{0.1}Fe_{0.9}O_{3-\delta}$;[258] PBC: $PrBaCo_2O_{5+\delta}$;[175] PCNCFO- PBC: $Pr_{0.2}Ce_{0.2}Ni_{0.2}Co_{0.2}Fe_{0.2}O_x$ coated on $PrBaCo_2O_{5+\delta}$;[175] SCM- BCFZY: $Sm_{0.85}Cu_{0.15}MnO_{3-\delta}$- $BaCo_{0.4}Fe_{0.4}Zr_{0.1}Y_{0.1}O_{3-\delta}$;[259] C/H-BSCF: $Ba_{1.5}Sr_{1.5}Co_{1.6}Fe_{0.4}O_{7-\delta}$;[260] U-BFZ-NM:$BaFe_{0.9}Zr_{0.1}O_{3-\delta}$-$NdMnO_{3-\delta}$;[261] CBSLCC: $Ce_{0.2}Ba_{0.2}Sr_{0.2}La_{0.2}Ca_{0.2}CoO_{3-\delta}$;[224] BCFT10: $Ba(Co_{0.7}Fe_{0.3})_{0.9}Ta_{0.1}O_{3-\delta}$;[262] BSCF: $Ba_{0.5}Sr_{0.5}Co_{0.8}Fe_{0.2}O_{3-\delta}$;[263] BSCFEr0.1: $Ba_{0.5}Sr_{0.5}(Co_{0.8}Fe_{0.2})_{0.9}Er_{0.1}O_{3-\delta}$;[263] BSTC: $BaSc_{0.1}Ta_{0.1}Co_{0.8}O_{3-\delta}$;[264] PNCO64: $Pr_4Ni_{1.8}Co_{1.2}O_{10-\delta}$;[265] N-BCFZYNF: $Ba(Co_{0.4}Fe_{0.4}Zr_{0.1}Y_{0.1})_{0.95}Ni_{0.05}F_{0.1}O_{2.9-\delta}$;[208] PBC-CHf0.1: $PrBa_{0.8}Ca_{0.2}Co_{1.9}Hf_{0.1}O_{5+\delta}$;[266] P2.7NCNO: $Pr_{2.7}Ni_{1.6}Cu_{0.3}Nb_{0.1}O_{7-\delta}$;[267] PBCC: $PrBa_{0.8}Ca_{0.2}Co_2O_{5+\delta}$;[268] PBCCPd: $PrBa_{0.8}Ca_{0.2}Co_{2-x}Pd_xO_{5+\delta}$;[268] PSFN/$Fe_2O_3$: Mixing $Pr_{0.4}Sr_{0.6}Fe_{0.9}Nb_{0.1}O_{3-\delta}$ and Fe_2O_3;[269] D-SFN: $Sr_{2.8}Fe_{1.8}Nb_{0.2}O_{7-\delta}$;[138] PBF-06$Y_2O_3$: 6%$Y_2O_3$ infiltrated $PrBaFe_2O_{5+\delta}$;[178] BLFZ0.95: $Ba_{0.95}La_{0.05}(Fe_{0.8}Zn_{0.2})_{0.95}O_{3-\delta}$;[71b] 2W-PBSCF: 2% $(NH_4)_{10}W_{12}O_{41}{\cdot}5H_2O$ mixed with $PrBa_{0.5}Sr_{0.5}Co_{1.5}Fe_{0.5}O_{5+\delta}$;[270] PCO-LSCF: $PrCoO_{3-\delta}$ coated on $La_{0.6}Sr_{0.4}Co_{0.2}Fe_{0.8}O_{3-\delta}$;[271] PBSC: $PrBa_{0.8}Sr_{0.2}CoO_{6-\delta}$;[223] HE-PBSLCC: High-entropy $Pr_{0.2}Ba_{0.2}Sr_{0.2}La_{0.2}Ca_{0.2}CoO_{3-\delta}$;[223] PBCsC: $PrBa_{0.9}Cs_{0.1}Co_2O_{5+\delta}$;[272] PNCO-64: $Pr_2Ni_{0.6}Co_{0.4}O_{4-\delta}$;[273] BCFN-BZCYY: $Ba_{0.9}Co_{0.7}Fe_{0.2}Nb_{0.1}O_{3-\delta}$ mixing with BZCYYb1711;[274] BSCFC: $Ba_{0.5}Sr_{0.5}Co_{0.8}Fe_{0.2}O_{2.9-\sigma}Cl_{0.1}$;[112] BCCY: $BaCo_{0.7}(Ce_{0.8}Y_{0.2})_{0.3}O_{3-\delta}$;[191] BCZY: $BaCo_{0.7}(Zr_{0.8}Y_{0.2})_{0.3}O_{3-\delta}$;[191] PNC-BCPY: $PrNi_{0.5}Co_{0.5}O_{3-\delta}$ coated on $BaCe_{0.5}Pr_{0.3}Y_{0.2}O_{3-\delta}$;[173] BCFNS: $BaCo_{0.4}Fe_{0.4}Nb_{0.1}Sc_{0.1}O_{3-\delta}$;[275] BSCFN-F0.1: $Ba_{0.6}Sr_{0.4}Co_{0.7}Fe_{0.2}Nb_{0.1}O_{2.9-\delta}F_{0.1}$;[276] LBSCF-BZCY: $La_{0.1}Ba_{0.4}Sr_{0.5}Co_{0.8}Fe_{0.2}O_{3-\delta}$ mixing with BZCY352;[277] BCCFYb: $BaCo_{0.5}Ce_{0.3}Fe_{0.1}Yb_{0.1}O_{3-\delta}$;[278] NBSCFN5: $NdBa_{0.5}Sr_{0.5}Co_{1.5}Fe_{0.45}Ni_{0.05}O_{5+\delta}$;[279] BCT20: $BaCo_{0.8}Ta_{0.2}O_{3-\delta}$;[280] PBCFN: $PrBaCo_{1.6}Fe_{0.2}Nb_{0.2}O_{5+\delta}$;[198] BCYF: $Ba(Ce_{0.8}Y_{0.2})_{0.2}Fe_{0.8}O_{3-\delta}$;[194] BCFZY-Ag: $Ba_{0.95}Ag_{0.05}Co_{0.4}Fe_{0.4}Zr_{0.1}Y_{0.1}O_{3-\delta}$;[202] BCFZYMg: $Ba(Co_{0.4}Fe_{0.4}Zr_{0.1}Y_{0.1})_{0.95}Mg_{0.05}O_{3-\delta}$;[118b] BC1.5MN: $Ba_2Co_{1.5}Mo_{0.25}Nb_{0.25}O_{6-\delta}$;[203] PLNBSCC: $Pr_{1/6}La_{1/6}Nd_{1/6}Ba_{1/6}Sr_{1/6}Ca_{1/6}CoO_{3-\delta}$;[222] PNC73: $PrNi_{0.7}Co_{0.3}O_{3-\delta}$;[281] BGPC44: $Ba_{0.8}Gd_{0.4}Pr_{0.4}Co_2O_{5+\delta}$;[282] BGPC: $Ba_{0.8}Gd_{0.8}Pr_{0.4}Co_2O_{5+\delta}$;[282] BCFZnY: $BaCo_{0.4}Fe_{0.4}Zn_{0.1}Y_{0.1}O_{3-\delta}$;[39] BSCFP0.05: $Ba_{0.5}Sr_{0.5}(Co_{0.8}Fe_{0.2})_{0.95}P_{0.05}O_{3-\delta}$;[283] BZFN-BZCY: $BaZr_{0.1}Fe_{0.75}Ni_{0.15}O_{3-\delta}$ mixing with BZCY172;[284] BB-OPS: one spot mixing $Ba_{0.5}Sr_{0.5}Co_{0.8}Fe_{0.2}O_{3-\delta}$ and $BaZr_{0.1}Ce_{0.7}Y_{0.1}Yb_{0.1}O_{3-\delta}$;[285] BB-PC: physically mixing $Ba_{0.5}Sr_{0.5}Co_{0.8}Fe_{0.2}O_{3-\delta}$ and $BaZr_{0.1}Ce_{0.7}Y_{0.1}Yb_{0.1}O_{3-\delta}$;[285] D-BFZ: $Ba_{0.875}Fe_{0.875}Zr_{0.125}O_{3-\delta}$;[70b] LSCF: $La_{0.6}Sr_{0.4}Co_{0.2}Fe_{0.8}O_{3-\delta}$;[168] BCO-LSCF: $BaCoO_{3-\delta}$ coated on $La_{0.6}Sr_{0.4}Co_{0.2}Fe_{0.8}O_{3-\delta}$;[168] SCFN: $Sr_{0.9}Ce_{0.1}Fe_{0.8}Ni_{0.2}O_{3-\delta}$;[205] BCFZYMn: $Ba(Co_{0.4}Fe_{0.4}Zr_{0.1}Y_{0.1})_{0.95}Mn_{0.05}O_{3-\delta}$;[117] PBCC: $PrBa_{0.8}Ca_{0.2}Co_2O_{5+\delta}$;[197b] LSCF2.7: $LaSr_{2.7}Co_{1.5}Fe_{1.5}O_{10-\delta}$;[286] NiO-BCFZY: NiO infiltrated $BaCo_{0.4}Fe_{0.4}Zr_{0.1}Y_{0.1}O_{3-\delta}$;[174] BSGC5124: $Ba_5SrGd_2Co_4O_{15}$;[287] BSGC-BCPY: mixing $Ba_5SrGd_2Co_4O_{15}$ with $BaCe_{0.5}Pr_{0.3}Y_{0.2}O_{3-\delta}$;[287] GCCCO: $Gd_{0.3}Ca_{2.7}Co_{3.82}Cu_{0.18}O_{9-\delta}$;[288] PBCC95: $(PrBa_{0.8}Ca_{0.2})_{0.95}Co_2O_{6-\delta}$;[289] SSC-SBC: mixing $Sm_{0.5}Sr_{0.5}CoO_{3-\delta}$ with $SmBaCo_2O_{5+\delta}$;[157] SCFZ: $SrCo_{0.8}Fe_{0.15}Zr_{0.05}O_{3-\delta}$;[290] BCCY: self-assembled $BaCo_{0.7}(Ce_{0.8}Y_{0.2})_{0.3}O_{3-\delta}$;[190] BSSNC: $Ba_{0.5}Sr_{0.5}Sc_{0.175}Nb_{0.025}Co_{0.8}O_{3-\delta}$;[291] LBCO: $LaBaCo_2O_{5+\delta}$;[78] BCFZY: $BaCo_{0.4}Fe_{0.4}Zr_{0.1}Y_{0.1}O_{3-\delta}$;[115] BCFZ: $BaCo_{0.4}Fe_{0.4}Zr_{0.2}O_{3-\delta}$;[114] PBC: $PrBaCo_2O_{5+\delta}$;[292] PSCN: $Pr_{0.5}Sr_{0.5}Co_{0.9}Nb_{0.1}O_{3-\delta}$;[293] PBIn0.1: $PrBaCo_{1.9}In_{0.1}O_{5+\delta}$;[294] PBCCHf0.1: $PrBa_{0.8}Ca_{0.2}Co_{1.9}Hf_{0.1}O_{5+\delta}$;[266] BCFZYNi: $Ba(Co_{0.4}Fe_{0.4}Zr_{0.1}Y_{0.1})_{0.95}Ni_{0.05}O_{3-\delta}$.[117]

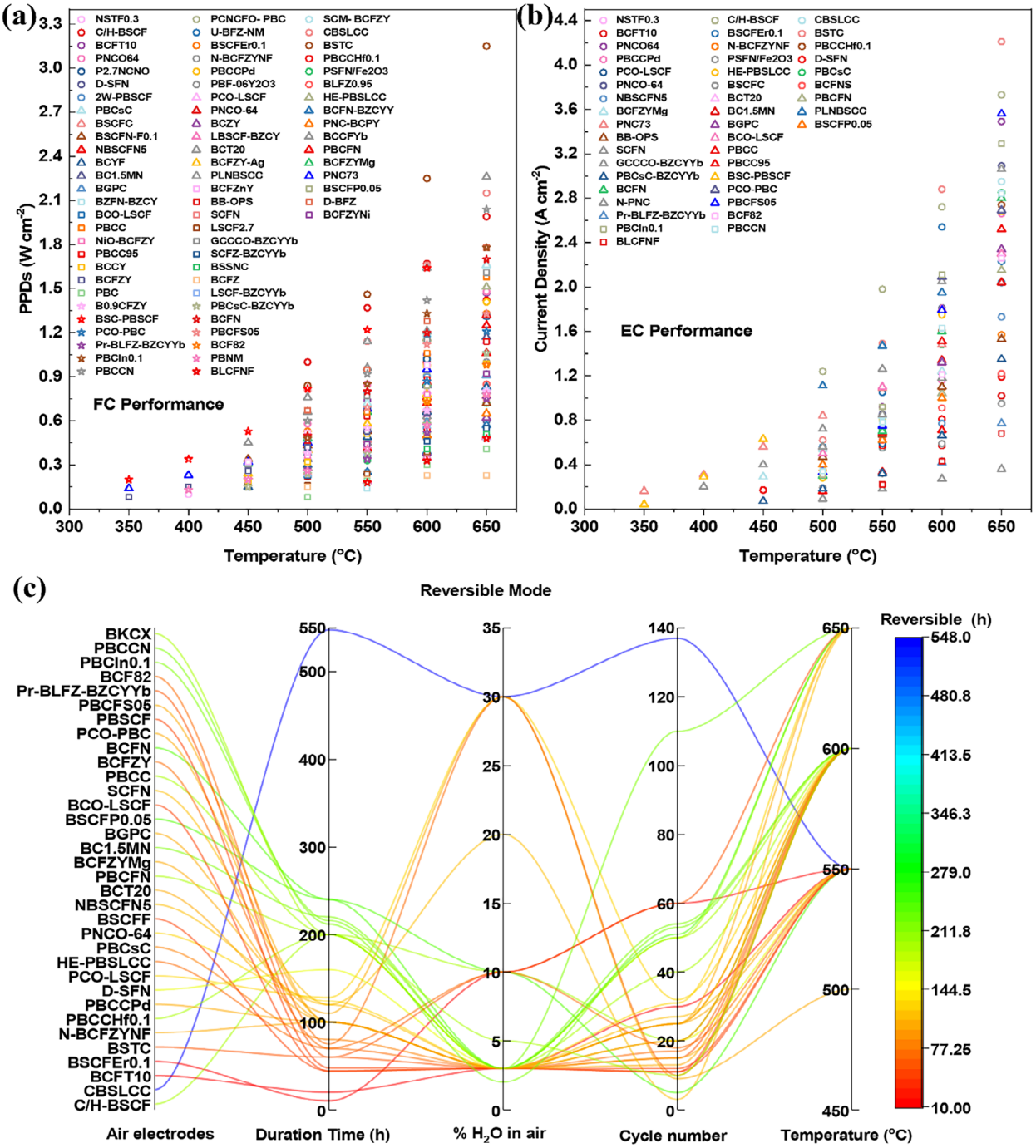

Figure 29. Comparison of electrochemical performance for single cells with advanced air electrodes in a) FC mode and b) EC mode; c) stability conditions of R-PCECs with different air electrodes operating in reversible modes.

significantly reduced electrocatalytic activity of air electrodes at lower temperatures, as observed in previous symmetrical cell analyses. In addition, the increase in ohmic resistance due to the diminished ionic conductivity of the electrolyte at these temperatures further limits the electrochemical output.

To further evaluate the OER catalytic activity of air electrodes, a comprehensive analysis of the electrochemical performance of R-PCECs operating in electrolysis mode was conducted, as illustrated in Figure 29b and **Table 4**. Under an applied voltage of 1.3 V, R-PCECs demonstrated robust water electrolysis performance across a temperature range of 450–650 °C. For instance, at 550 °C, 16 air electrodes achieved electrolysis current densities exceeding 0.8 A cm^{-2}. Notably, the C/HBSCF electrode exhibited an impressive current density of 1.98 A cm^{-2} under 10% steam. In contrast, when the steam pressure increased to 50%, the PNC73 air electrode maintained a current density above 1 A cm^{-2}. These

Table 3. PPD values of advanced air electrodes based on single cells operating in FC mode at 450–650 °C.

Air electrodes	Electrolyte (thickness)	Atmosphere	PPD [W cm^{-2}]					Refs.
			650 °C	600 °C	550 °C	500 °C	450 °C	
NSTF0.3	BZCYYb1711 (22.5 μm)	H_2 / air	0.77	0.63	0.49	0.34	0.19	[258]
PCNCFO- PBC	BZCYYb1711 (10 μm)	3%H_2O–H_2 / air	1.31	0.91	/	/	/	[175]
SCM- BCFZY	BZY0.15 (14 μm)	3%H_2O–H_2 / air	1.06	0.67	/	/	/	[259]
C/H-BSCF	BZCYYb1711 (8 μm)	H_2 / 10%H_2O–air	1.99	1.67	1.37	1.00	/	[260]
U-BFZ-NM	BZCYYb1711 (5.6 μm)	H_2 / air	0.60	0.55	0.36	0.22	/	[261]
CBSLCC	BZCYYb1711 (6 μm)	H_2 / air	2.15	1.66	1.14	0.81	/	[224]
BCFT10	BZCYYb1711 (16 μm)	H_2 / 3%H_2O–air	1.47	1.05	0.74	0.48	/	[262]
BSCFEr0.1	BZCYYb1711 (7 μm)	H_2 / 10%H_2O–air	1.33	0.98	0.70	0.53	/	[263]
BSTC	BZCYYb4411 (6.5 μm)	3%H_2O–H_2 / 3%H_2O–air	3.15	2.25	1.46	0.84	/	[264]
PNCO64	BZCYYb1711 (8 μm)	3%H_2O–H_2 / 3%H_2O–air	1.48	1.18	0.85	0.58	/	[265]
N-BCFZYNF	BZCYYb1711 (10.79 μm)	H_2 / 3%H_2O–air	1.00	0.78	0.55	0.37	/	[208]
PBCCHf0.1	BZCYYb1711 (7.8 μm)	3%H_2O–H_2 / 3%H_2O–air	1.42	1.00	0.67	/	/	[266]
P2.7NCNO	BZCYYb1711 (19 μm)	3%H_2O–H_2 / air	1.31	1.02	0.68	0.37	/	[267]
PBCCPd	BZCYYb1711 (8 μm)	3%H_2O–H_2 / 3%H_2O–air	1.41	0.97	/	/	/	[268]
PSFN/Fe_2O_3	BZCYYb1711 (10 μm)	3%H_2O–H_2 / air	0.72	0.52	0.33	/	/	[269]
D-SFN	BZCYYb1711 (23 μm)	H_2 / air	0.60	0.48	0.36	0.24	0.17	[138]
PBF-06Y_2O_3	BZCYYb1711 (14 μm)	3%H_2O–H_2 / air	0.50	0.35	0.25	/	/	[178]
BLFZ0.95	BZCYYb1711 (10 μm)	3%H_2O–H_2 / air	0.85	0.62	0.40	0.24	/	[71b]
2W-PBSCF	BZCYYb1711 (10 μm)	3%H_2O–H_2 / air	1.32	0.90	0.57	/	/	[270]
PCO-LSCF	BZCYYb4411 (12 μm)	3%H_2O–H_2 / 3%H_2O–air	1.14	0.80	0.53	/	/	[271]
HE-PBSLCC	BZCYYb1711 (10 μm)	3%H_2O–H_2 / air	1.51	1.16	0.72	0.40	/	[223]
PBCsC	BZCYYb1711 (8 μm)	3%H_2O–H_2 / air	1.66	1.19	0.72	0.41	/	[272]
PNCO-64	BZCYYb1711 (10 μm)	3%H_2O–H_2 / air	1.32	0.86	0.58	/	/	[273]
BCFN-BZCYY	BZCYYb1711 (10 μm)	/	0.57	0.39	0.25	/	/	[274]
BSCFC	BZCYYb1711 (16.6 μm)	H_2 / air	0.77	0.67	0.47	0.30	0.22	[112]
BCZY	BZCYYb1711 (11.1 μm)	3%H_2O–H_2 / 3%H_2O–air	0.62	0.38	/	/	/	[191]
PNC-BCPY	BZYb82 (13 μm)	3%H_2O–H_2 / 3%H_2O–air	0.65	0.50	/	/	/	[173]
BSCFN-F0.1	BZCYYb1711 (20 μm)	3%H_2O–H_2 / air	0.72	0.63	0.53	0.43	0.34	[276]
LBSCF-BZCY	BZCY352 (20 μm)	3%H_2O–H_2 / air	0.49	0.35	0.19	/	/	[277]
BCCFYb	BZCYYb1711 (30 μm)	H_2 / air	0.80	0.63	0.45	0.28	/	[278]
NBSCFN5	BZCYYb1711 (15 μm)	3%H_2O–H_2 / air	1.25	0.76	0.41	/	/	[279]
BCT20	BZCYYb4411 (10 μm)	3%H_2O–H_2 / air	2.26	1.64	1.14	0.76	0.45	[280]
PBCFN	BZCYYb1711 (10 μm)	3%H_2O–H_2 / air	1.06	0.72	/	/	/	[198]
BCYF	BZCYYb1711 (15.8 μm)	H_2 / air	0.83	0.66	0.49	0.30	0.15	[194]
BCFZY-Ag	BZCYYb1711 (10 μm)	3%H_2O–H_2 / air	/	0.78	0.58	0.40	0.24	[202]
BCFZYMg	BZCYYb1711 (16 μm)	H_2 / air	/	0.85	0.66	0.48	0.31	[118b]
BC1.5MN	BZCYYb1711 (10 μm)	3%H_2O–H_2 / air	1.17	0.84	0.54	0.34	/	[203]
PLNBSCC	BZCYYb1711 (6.5 μm)	H_2 / air	/	1.21	0.96	0.66	/	[222]
PNC73	BZCYYb4411 (15 μm)	3%H_2O–H_2 / O_2	/	0.95	0.68	0.45	0.32	[281]
BGPC	BZCYYb1711 (10 μm)	3%H_2O–H_2 / air	0.91	0.59	/	/	/	[282]
BCFZnY	BZCYYb1711 (11.8 μm)	H_2 / air	/	0.98	0.77	0.52	0.32	[39]
BSCFP0.05	BZCYYb1711 (16 μm)	H_2 / air	/	0.84	0.64	0.43	/	[283]
BZFN-BZCY	BZCY172 (19 μm)	3%H_2O–H_2 / air	0.48	0.30	0.14	/	/	[284]
BB-OPS	BZCYYb1711 (22 μm)	H_2 / air	1.14	0.88	0.63	0.43	/	[285]
D-BFZ	BZCYYb1711 (4 μm)	H_2 / air	1.78	1.28	0.95	0.67	/	[70b]
BCO-LSCF	BZCYYb1711 (10 μm)	3%H_2O–H_2 / air	1.60	1.16	0.78	0.41	/	[168]
SCFN	BZCYYb1711 (26 μm)	H_2 / air	0.75	0.53	0.35	0.23	/	[205]
BCFZYNi	BZCYYb1711 (14 μm)	H_2 / air	0.92	0.65	0.44	0.26	/	[117]

(*Continued*)

Table 3. (Continued)

Air electrodes	Electrolyte (thickness)	Atmosphere	PPD [W cm^{-2}]					Refs.
			650 °C	600 °C	550 °C	500 °C	450 °C	
PBCC	BZCYYb1711 (10 μm)	3%H_2O–H_2 / air	1.58	1.06	0.66	/	/	[197b]
LSCF2.7	BZCY172 (28 μm)	3%H_2O–H_2 / air	0.52	0.39	0.24	0.16	/	[286]
NiO-BCFZY	BZCYYb1711 (10 μm)	3%H_2O–H_2 / air	/	0.78	0.53	0.36	/	[174]
GCCCO-BZCYYb	BZCYYb1711 (17 μm)	3%H_2O–H_2 / air	1.60	1.16	0.77	0.48	0.28	[288]
PBCC95	BZCYYb4411 (20 μm)	3%H_2O–H_2 / air	/	0.54	0.35	0.22	/	[289]
SCFZ-BZCYYb	BZCYYb1711 (38 μm)	H_2 / air	0.55	0.46	0.35	0.23	/	[290]
BCCY	BZCYYb1711 (16.1 μm)	H_2 / air	0.99	0.74	0.51	0.32	0.19	[190]
BSSNC	BZCY172 (32 μm)	H_2 / air	0.51	0.41	0.34	/	/	[291]
BCFZY	BZCYYb1711 (25 μm)	3%H_2O–H_2 / air	/	0.66	0.53	0.42	0.26	[115]
BCFZ	BZCYYb1711 (15 μm)	H_2 / air	0.23	0.23	0.20	0.15	/	[114]
PBC	BZCY172 (30 μm)	3%H_2O–H_2 / air	0.41	0.30	0.19	0.08	/	[292]
LSCF-BZCYYb	BZCYYb1711 (14 μm)	3%H_2O–H_2 / 3%H_2O–air	0.81	0.57	0.38	0.24	/	[295]
B0.9CFZY	BZCY (40 μm)	3%H_2O–H_2 / air	0.80	0.67	0.55	0.38	/	[70a]
PBCsC-BZCYYb1711	BZCYYb1711 (10 μm)	3%H_2O–H_2 / 3%H_2O–air	1.06	0.58	0.38	0.24	0.15	[296]
BSC-PBSCF	BZCYYb4411 (≈3.5 μm)	3%H_2O–H_2 / air	/	1.64	1.22	0.82	0.53	[297]
BCFN	BZCYYb1711 (≈10 μm)	3%H_2O–H_2 / air	1.7	1.2	0.8	0.5	/	[199]
PCO-PBC	BZCYYb1711 (≈15 μm)	3%H_2O–H_2 / air	1.21	0.87	/	/	/	[170]
PBCFS05	BZCYYb4411 (6-7μm)	3%H_2O–H_2 / air	1.33	1.12	0.69	/	/	[298]
Pr-BLFZ-BZCYYb	BZCYYb1711 (≈5 μm)	3%H_2O–H_2 / air	0.75	0.52	0.34	/	/	[299]
BCF82	BZCYYb1711 (≈10 μm)	3%H_2O–H_2 / air	0.98	0.73	/	/	/	[300]
PBCIn0.1	BZCYYb1711 (≈8 μm)	3%H_2O–H_2 / air	1.78	1.33	0.85	0.48	/	[294]
PBNM	BZCYYb1711 (12 μm)	3%H_2O–H_2 / air	0.78	0.57	0.41	0.26	0.20	[135a]
PBCCN	BZCYYb1711 (≈5 μm)	3%H_2O–H_2 / air	2.04	1.42	0.92	0.60	/	[301]
BLCFNF	BZCY172 (25 μm)	3%H_2O–H_2 / 3%H_2O–air	0.48	0.33	0.18	/	/	[302]

findings underscore the notable OER catalytic activity of advanced air electrodes at 550 °C and higher, even under high water vapor conditions. However, some air electrodes, such as BSCFC, exhibited electrolysis currents below 0.3 A cm^{-2}, likely due to their limited water adsorption and proton transport capacities. Furthermore, as the operating temperature decreases, particularly below 450 °C, the electrolysis performance significantly declines, with current densities dropping below 0.2 A cm^{-2} at 350 °C.

The electrochemical performance of R-PCECs in reversible operation modes, specifically their stability during cyclic FC and EC modes, has also been summarized and analyzed. Unlike stability assessments conducted in standalone FC or EC modes, reversible cycling requires the air electrode to seamlessly transition between ORR and OER processes. This places considerable stress on the electrode material's ability to function as a bifunctional catalyst under high-temperature and humid conditions, with critical factors including microstructural integrity, phase transitions, and changes in surface chemical states. As shown in Figure 29c and **Table 5**, most reported cycle stability tests were conducted for periods of 150 h or less, with few studies exceeding 200 h. In comparison, the stability durations achieved in standalone FC or EC modes are substantially longer. For example, the GCCCO-BZCYYb air electrode demonstrated 932 h in FC mode and 1400 h in EC mode,[288] while BCFZY achieved 1100 h in FC mode,[115] and the PBCC[197b] air electrode reached 1833 h in EC mode. These results indicate that the stability tests in cyclic operation are relatively short. Additionally, most of these tests were performed under vapor pressures below 10%, predominantly around 3%, which limits the understanding of how higher vapor pressures influence the kinetics and degradation mechanisms of air electrodes during reversible operation. Encouragingly, the high-entropy CBSLCC air electrode demonstrated stable cycling for 137 cycles over 548 h under high vapor pressure (30%). Nevertheless, for most air electrodes, increasing the vapor pressure and extending the testing duration remain critical challenges for fully assessing their feasibility under reversible operation conditions.

In summary, enhancing R-PCEC performance and stability at lower operating temperatures (≤450 °C) remains a significant challenge. Improving the catalytic activity of air electrodes will be crucial in overcoming this limitation and achieving superior electrochemical performance under these conditions.

6. Challenges and Prospects

A thorough analysis of the physicochemical properties, modification strategies, and electrochemical performance of various candidate air electrode materials reveals several challenges in the development of high-performance, stable bifunctional catalysts.

Table 4. Current density of advanced air electrodes in single cells operating in EC mode in humidified air at 450–650 °C with an applied voltage of 1.3 V.

Air Electrodes	Electrolyte (thickness)	Atmosphere	Current density@1.3 V (A cm^{-2})					Refs.
			650 °C	600 °C	550 °C	500 °C	450 °C	
NSTF0.3	BZCYYb1711 (22.5 μm)	10%H_2O–air	/	1.22	/	/	/	[258]
C/H-BSCF	BZCYYb1711 (8 μm)	10%H_2O–air	3.73	2.72	1.98	1.24	/	[260]
CBSLCC	BZCYYb1711 (6 μm)	3%H2O–air	2.95	1.76	0.84	/	/	[224]
BCFT10	BZCYYb1711 (16 μm)	3%H_2O–air	1.02	0.57	0.32	/	/	[262]
BSCFEr0.1	BZCYYb1711 (7 μm)	10%H_2O–air	2.23	2.54	1.05	0.56	/	[263]
BSTC	BZCYYb4411 (6.5 μm)	3%H_2O–air	4.21	2.88	1.49	0.62	/	[264]
PNCO64	BZCYYb1711 (8 μm)	3%H_2O–air	3.49	2.08	0.92	0.35	/	[265]
N-BCFZYNF	BZCYYb1711 (10.79 μm)	3%H_2O–air	1.57	1.09	0.68	0.35	/	[208]
PBCCHf0.1	BZCYYb1711 (7.8 μm)	3%H_2O–air	2.74	1.61	0.84	/	/	[266]
PBCCPd	BZCYYb1711 (8 μm)	3%H_2O–air	2.66	1.16	/	/	/	[268]
PSFN/Fe_2O_3	BZCYYb1711 (10 μm)	10%H_2O–air	1.21	0.91	0.55	/	/	[269]
D-SFN	BZCYYb1711 (23 μm)	3%H_2O–air	1.19	0.81	0.57	0.29	0.17	[138]
PCO-LSCF	BZCYYb4411 (12 μm)	30%H_2O–air	2.04	1.22	0.59	/	/	[271]
HE-PBSLCC	BZCYYb1711 (10 μm)	3%H_2O–air	2.68	1.75	0.80	0.28	/	[223]
PBCsC	BZCYYb1711 (8 μm)	3%H_2O–air	2.85	1.48	0.71	0.31	/	[272]
PNCO-64	BZCYYb1711 (10 μm)	3%H_2O–air	3.09	1.81	0.85	/	/	[273]
BSCFC	BZCYYb1711 (16.6 μm)	3%H_2O–air	0.95	0.59	0.32	0.19	/	[112]
BCFNS	BZCYYb1711 (≈50 μm)	3%H_2O–air	1.22	0.91	0.62	0.31	/	[275]
NBSCFN5	BZCYYb1711 (15 μm)	20%H_2O–air	1.73	0.77	0.33	/	/	[279]
BCT20	BZCYYb4411 (10 μm)	3%H_2O–air	2.33	1.60	0.84	/	/	[280]
PBCFN	BZCYYb1711 (10 μm)	3%H_2O–air	2.15	1.04	/	/	/	[198]
BCFZYMg	BZCYYb1711 (16 μm)	10%H_2O–air	/	1.24	0.84	0.54	0.29	[118b]
BC1.5MN	BZCYYb1711 (10 μm)	3%H_2O–air	2.04	1.34	0.68	/	/	[203]
PLNBSCC	BZCYYb1711 (6.5 μm)	10%H_2O–air	/	1.95	1.47	1.11	/	[222]
PNC73	BZCYYb4411 (15 μm)	50%H_2O-O_2	/	1.48	1.09	0.84	0.56	[281]
BGPC	BZCYYb1711 (10 μm)	3%H_2O–air	2.34	1.32	/	/	/	[282]
BSCFP0.05	BZCYYb1711 (16 μm)	10%H_2O–air	/	1.00	0.62	0.40	/	[283]
BB-OPS	BZCYYb1711 (22 μm)	10%H_2O–air	1.53	1.10	0.67	0.47	/	[285]
BCO-LSCF	BZCYYb1711 (10 μm)	3%H_2O–air	2.30	1.80	1.10	0.50	/	[168]
SCFN	BZCYYb1711 (26 μm)	3%H_2O–air	0.36	0.27	0.18	0.09	/	[205]
PBCC	BZCYYb1711 (10 μm)	3%H_2O–air	2.52	1.51	0.69	/	/	[197b]
GCCCO-BZCYYb	BZCYYb1711 (17 μm)	20%H_2O–air	3.06	2.05	1.26	0.72	/	[288]
PBCC95	BZCYYb4411 (20 μm)	3%H_2O–air	/	0.71	0.33	0.16	/	[289]
PBCsC-BZCYYb	BZCYYb1711 (10 μm)	3%H_2O–air	1.35	0.66	0.32	0.18	0.07	[296]
BSC-PBSCF	BZCYYb4411 (≈3.5μm)	40%H_2O-60%N_2	/	/	/	/	0.63	[297]
BCFN	BZCYYb1711 (≈10 μm)	3%H_2O–air	2.8	1.6	0.7	0.3	/	[199]
PCO-PBC	BZCYYb1711 (≈15 μm)	3%H_2O–air	2.69	2.09	/	/	/	[170]
N-PNC	BZCYYb4411 (≈12μm)	10%H_2O–air		1.18	0.85	0.56	0.40	[19d]
PBCFS05	BZCYYb4411 (6-7μm)	3%H_2O–air	3.56	1.79	0.75	0.33	/	[298]
Pr-BLFZ-BZCYYb	BZCYYb1711 (≈5 μm)	10%H_2O–air	0.77	0.42	/	/	/	[299]
BCF82	BZCYYb1711 (≈10 μm)	30%H_2O–air	2.26	1.21	/	/	/	[300]
PBCIn0.1	BZCYYb1711 (≈8 μm)	3%H_2O–air	3.29	2.11	0.92	0.31	/	[294]
PBCCN	BZCYYb1711 (≈5 μm)	3%H_2O–air	2.84	1.63	0.78	0.34	/	[301]
BLCFNF	BZCY172 (25 μm)	3%H_2O–air	0.68	0.43	0.22	/	/	[302]

Table 5. Stability tests of advanced air electrodes in reversible modes.

Air Electrodes	Electrolyte (thickness)	Atmosphere (%H_2O–air)	Duration (h/cycles)	FC	EC	Temperature [°C]	Refs.
C/H-BSCF	BZCYYb1711 (22.5 μm)	10	200/20	0.45 A cm^{-2}	−1.8 A cm^{-2}	600	[260]
CBSLCC	BZCYYb1711 (6 μm)	30	548/137	0.5 A cm^{-2}	−0.5 A cm^{-2}	550	[224]
BCFT10	BZCYYb1711 (16 μm)	3	20/30	0.8/0.7/0.6 V	1.2/1.3/1.4 V	550	[262]
BSCFEr0.1	BZCYYb1711 (7 μm)	10	10/60	0.1/0.3/0.5 A cm^{-2}	−0.3/−0.5/−0.7 A cm^{-2}	550	[263]
BSTC	BZCYYb4411 (6.5 μm)	3	60/15	1.0 A cm^{-2}	−3.0 A cm^{-2}	600	[264]
N-BCFZYNF	BZCYYb1711 (10.8 μm)	3	100/15	0.38 A cm^{-2}	−0.5 A cm^{-2}	550	[208]
PBCCHf0.1	BZCYYb1711 (7.8 μm)	3	200/40	0.5 A cm^{-2}	−0.5 A cm^{-2}	600	[266]
PBCCPd	BZCYYb1711 (8 μm)	3	100/25	0.5 A cm^{-2}	−0.5 A cm^{-2}	600	[268]
D-SFN	BZCYYb1711 (23 μm)	3	160/20	0.8 V	1.3 V	550	[138]
PCO-LSCF	BZCYYb4411 (12 μm)	30	128/32	0.7 V	1.3 V	600	[271]
HE-PBSLCC	BZCYYb1711 (10 μm)	3	70/17	0.5 A cm^{-2}	−0.5 A cm^{-2}	600	[223]
PBCsC	BZCYYb1711 (8 μm)	3	80/20	0.5 A cm^{-2}	−0.5 A cm^{-2}	600	[272]
PNCO-64	BZCYYb1711 (10 μm)	3	124/31	0.5 A cm^{-2}	−0.5 A cm^{-2}	650	[273]
BSCFF	BZCYYb1711 (16.6 μm)	3	44/11	0.3 A cm^{-2}	−0.3 A cm^{-2}	550	[112]
NBSCFN5	BZCYYb1711 (15 μm)	20	120/3	0.2 A cm^{-2}	−0.2 A cm^{-2}	650	[279]
BCT20	BZCYYb4411 (10 μm)	3	100/25	0.7 V	1.3 V	550	[280]
PBCFN	BZCYYb1711 (10 μm)	3	200/50	0.5 A cm^{-2}	−0.5 A cm^{-2}	650	[198]
BCFZYMg	BZCYYb1711 (16 μm)	30	110/9	0.3 A cm^{-2}	−0.3 A cm^{-2}	500	[118b]
BC1.5MN	BZCYYb1711 (10 μm)	3	≈220/110	0.5 A cm^{-2}	−0.5 A cm^{-2}	650	[203]
BGPC	BZCYYb1711 (10 μm)	3	100/25	0.5 A cm^{-2}	−0.5 A cm^{-2}	600	[282]
BSCFP0.05	BZCYYb1711 (16 μm)	10	240/5	0.2 A cm^{-2}	−0.6 A cm^{-2}	550	[283]
BCO-LSCF	BZCYYb1711 (10 μm)	3	44/11	0.5 A cm^{-2}	−0.5 A cm^{-2}	600	[168]
SCFN	BZCYYb1711 (26 μm)	3	120/27	0.8V	1.3 V	550	[205]
PBCC	BZCYYb1711 (10 μm)	3	≈200/50	0.5 A cm^{-2}	−0.5 A cm^{-2}	600	[197b]
BCFZY	BZCYYb1711 (≈13 μm)	10	70/18	0.4 A cm^{-2}	1.4 A cm^{-2}	550	[7]
BCFN	BZCYYb1711 (≈10 μm)	3	240/51	0.5 A cm^{-2}	−0.5 A cm^{-2}	650	[199]
PCO-PBC	BZCYYb1711 (≈15 μm)	3	100/25	0.5 A cm^{-2}	−0.5 A cm^{-2}	650	[170]
PBSCF	BZCYYb4411 (≈15 μm)	3	48/12	0.7 V	1.3 V	550	[122]
PBCFS05	BZCYYb4411 (6-7 μm)	3	100/13	0.7 V	1.3 V	600	[298]
Pr-BLFZ-BZCYYb	BZCYYb1711 (≈5 μm)	10	60/60	0.3 A cm^{-2}	−0.3 A cm^{-2}	650	[299]
BCF82	BZCYYb1711 (≈10 μm)	30	75/10	0.8 V	1.3 V	600	[300]
PBCIn0.1	BZCYYb1711 (≈8 μm)	3	216/54	0.5 A cm^{-2}	−0.3 5 cm^{-2}	600	[294]
PBCCN	BZCYYb1711 (≈5 μm)	2	212/53	0.5 A cm^{-2}	−0.3 5 cm^{-2}	600	[301]
BKCX	BZCYYb1711 (11 μm)	5	200/10	0.2 A cm^{-2}	−0.2 A cm^{-2}	600	[303]

Air electrodes: PBCsC-BZCYYb: infiltrating $PrBa_{0.875}Cs_{0.125}Co_2O_{5+\delta}$ into BZCYYb1711 backbone;[296] BSC-PBSCF: $Ba_{0.62}Sr_{0.38}CoO_{3-\delta}$–$Pr_{1.44}Ba_{0.11}Sr_{0.45}Co_{1.32}Fe_{0.68}O_{6-\delta}$;[297] BCFN: $Ba_{0.9}Co_{0.7}Fe_{0.2}Nb_{0.1}O_{3-\delta}$;[199] PCO-PBC: $Pr_{0.1}Ce_{0.9}O_{2+\delta}$ coasted on $PrBaCo_2O_{5+\delta}$;[170] N-PNC: nano-fiber $PrNi_{0.5}Co_{0.5}O_{3-\delta}$;[19d] PBCFS05: $Pr_{0.5}Ba_{0.5}Co_{0.7}Fe_{0.95}Sn_{0.05}O_{3-\delta}$;[298] Pr-BLFZ-BZCYYb: PrOx-coated $Ba_{0.95}La_{0.05}Fe_{0.8}Zn_{0.2}O_{3-\delta}$-$BaZr_{0.1}Ce_{0.7}Y_{0.1}Yb_{0.1}O_{3-\delta}$;[299] BCF82: $Ba_{0.8}Ca_{0.2}FeO_{3-\delta}$;[300] PBNM: $Pr_2BaNiMnO_{7-\delta}$;[135a] PBCCN: $PrBa_{0.9}Cs_{0.1}Co_{1.9}Nb_{0.1}O_{6-\delta}$;[301] BLCFNF: $Ba_{0.8}La_{0.1}Co_{0.2}Fe_{0.7}Nb_{0.1}F_{0.1}O_{2.9-\delta}$;[302] BKCX:$Ba_{0.95}K_{0.05}Co_{0.2}Zn_{0.2}Ga_{0.2}Zr_{0.2}Y_{0.2}O_{3-\delta}$.[303]

From an electrochemical kinetics perspective, it is critical to design air electrodes with triple conductivity (electronic, oxygen ion, and proton) to increase the number of active sites for catalytic reactions. However, achieving high ionic conductivity, particularly proton conductivity related to water absorption and proton transfer, remains challenging. Additionally, the simultaneous transport of protons and oxygen ions introduces competing reaction mechanisms, which limits the simultaneous enhancement of both transport processes. In terms of structural stability, air electrode materials must balance water absorption capacity and resistance to excessive water uptake. High water vapor pressures, which are beneficial for improving electrolysis efficiency and hydrogen production rates in R-PCECs, can degrade structural stability. In addition, most current research on air electrode stability has limited tests for only a few hundred hours, which is far from being sufficient for practical applications. For instance, the United States Department of Energy set a 2019 target requiring fuel cells to demonstrate an operational lifespan of at least 40,000 h, with a degradation rate not exceeding 0.2% per 1000 h.[304]

Furthermore, the adoption of iron-based air electrodes, which possess lower thermal expansion coefficients and are more cost-effective compared to cobalt-based electrodes, can enhance the

stability of the electrode-electrolyte interface while simultaneously reducing overall material costs. However, this shift often leads to changes in catalytic activity and ionic conductivity, complicating material optimization. From a modification perspective, no single strategy has yet proven capable of simultaneously optimizing both catalytic performance and stability in air electrodes. A multi-dimensional evaluation of modification techniques is needed. Regarding practical applications, most air electrode materials exhibit satisfactory electrochemical performance between 500 °C and 650 °C. However, few studies report on their performance at lower temperatures, such as 400 °C and below, likely due to significantly reduced catalytic activity at these lower temperatures. The limited research on the electrochemical performance and physicochemical properties of air electrodes at lower temperatures complicates efforts to reduce the operating temperature of R-PCECs.

Despite these challenges, the development of air electrode materials has made significant progress over the past several decades, and their future potential is promising. Theoretical models and experimental methods have provided valuable insights into the reaction mechanisms and identified the strengths and weaknesses of various electrode materials. Advanced modification strategies based on mechanistic understanding have substantially improved catalytic activity in air electrodes. Moreover, artificial intelligence (AI) serves as a versatile technology that can be applied across a wide range of materials science disciplines, including modeling, simulation, characterization, synthesis, and optimization of materials. AI techniques can primarily be classified into two categories: learning approaches and optimization strategies. Learning approaches, such as ML, have the capability to derive insights from data, enabling predictions or decisions based on the patterns identified within the data. In terms of optimization techniques, methodologies such as Genetic Algorithms (GA) and Bayesian optimization (BO) are utilized to identify the best solutions or configurations for specific objectives. These methods are increasingly employed in the design of material microstructures, optimization of material compositions, and the generation of material structures. However, it is important to note that there is currently no dedicated database specifically for AI in air electrode materials. Therefore, establishing such a database is essential, utilizing appropriate material descriptors that reflect the distinctive attributes of air electrodes, including reaction kinetics, conductivity ($H^+/O^{2-}/e^-$), surface and bulk properties, and compatibility with electrolytes. The precision of the data within this database is fundamental to ensuring the reliability of AI learning and optimization models. The accurate definition of descriptors and the successful creation of this database depend heavily on a substantial collection of precise experimental results, particularly in understanding how varying chemical compositions and fabrication methods affect the performance of diverse air electrodes, highlighting the necessity for accuracy and reproducibility.

Moreover, DFT calculations offer valuable insights into the physicochemical properties of air electrode materials, enabling a deeper understanding and targeted optimization of their intrinsic characteristics. In addition, since the detailed reaction mechanisms in air electrodes as well as the charge carrier conduction mechanisms are still unclear, multiphysics modeling that considers these processes and is validated by experimental measurements can provide insights for identifying and facilitating rate-determining steps in these processes. Moreover, future advancements may involve meso-scale models to elucidate the effects of microstructure of the air electrode on the reaction and transport processes. These models can assess the impact of material composition on electrode microstructure and how this, in turn, influences air electrode performance. By delving into these connections, a comprehensive understanding of the interplay among material composition, microstructure, and electrode performance can be attained through numerical simulations. Likewise, leveraging ML techniques can facilitate the optimization of electrode microstructure to enhance overall performance.

In the future, the integration of advanced modification strategies, coupled with the synergy between theoretical modeling and experimental validation, is expected to significantly advance the rational design and performance enhancement of air electrode materials.

7. Summary

Overall, this review provides a detailed and systematic examination of the mechanisms governing air electrode reactions, ion transport pathways, and the key factors influencing the physicochemical properties of these materials. It also evaluates a wide range of air electrode oxides, their modification strategies — highlighting both their merits and limitations — and the status of their electrochemical performance. By integrating insights from both theoretical studies and practical applications, this review offers a thorough analysis of recent advancements, ongoing challenges, and future directions for the development of air electrodes in R-PCEC technology.

Substantial progress has been made in elucidating the fundamental mechanisms of air electrode materials, leading to the development of increasingly efficient and stable bifunctional air electrodes. These advances are propelling the performance of R-PCECs, facilitating their commercialization as clean and efficient energy conversion and storage systems, and enabling the production of high-value chemicals. However, the path to developing optimal air electrode materials remains fraught with significant challenges. These include difficulties in validating ion transport behavior (theoretically and experimentally), accurately measuring triple conductivity, and the lack of high-temperature in-situ observations of electrode degradation. Additionally, the stability of air electrode materials — both in terms of interfacial and intrinsic stability — remains a critical issue, alongside the relatively poor catalytic activity observed at lower temperatures and the limitations of current modification approaches. Overcoming these hurdles will require further in-depth research, presenting numerous important and compelling avenues for future studies aimed at accelerating the development of air electrodes for R-PCECs.

Acknowledgements

M.N. thanks the grant (Project Number: 15306723 and SRFS2324-5S02) from the Research Grants Council, University Grants Committee, Hong Kong SAR. T.L. thanks the project of the National Natural Science Foundation of China (22209138).

Conflict of Interest

The authors declare no conflict of interest.

Keywords

air electrodes, oxygen evolution reaction, oxygen reduction reaction, reversible protonic ceramic electrochemical cells, triple conductivity

Received: November 28, 2024
Revised: March 20, 2025
Published online:

[1] C. J. Axon, R. C. Darton, *Sustain. Prod. Consump.* **2021**, *27*, 1195.
[2] A. G. Olabi, M. A. Abdelkareem, *Renewable Sustainable Energy Rev.* **2022**, *158*, 112111.
[3] a) Y.-M. Wei, K. Chen, J.-N. Kang, W. Chen, X.-Y. Wang, X. Zhang, *Engineering* **2022**, *14*, 52; b) A. Dannenberg, M. Lumkowsky, E. K. Carlton, D. G. Victor, *Proc. Natl. Acad. Sci. USA* **2023**, *120*, 2305075120; c) J. Bistline, G. Blanford, M. Brown, D. Burtraw, M. Domeshek, J. Farbes, A. Fawcett, A. Hamilton, J. Jenkins, R. Jones, B. King, H. Kolus, J. Larsen, A. Levin, M. Mahajan, C. Marcy, E. Mayfield, J. McFarland, H. McJeon, R. Orvis, N. Patankar, K. Rennert, C. Roney, N. Roy, G. Schivley, D. Steinberg, N. Victor, S. Wenzel, J. Weyant, R. Wiser, et al., *Science* **2023**, *380*, 1324.
[4] J. M. Chen, *Innovation* **2021**, *2*, 100127.
[5] M. Lamagna, B. Nastasi, D. Groppi, C. Rozain, M. Manfren, D. A. Garcia, *Energy Convers. Manage.* **2021**, *235*, 113993.
[6] Y. Tian, W. Wang, Y. Liu, A. Naden, M. Xu, S. Wu, B. Chi, J. Pu, J. S. Irvine, *ACS Catal.* **2021**, *11*, 3704.
[7] C. Duan, R. Kee, H. Zhu, N. Sullivan, L. Zhu, L. Bian, D. Jennings, R. O'Hayre, *Nat. Energy* **2019**, *4*, 230.
[8] D. Kim, K. T. Bae, K. J. Kim, H. Im, S. Jang, S. Oh, S. Lee, T. Shin, K. Lee, *ACS Energy Lett.* **2022**, *7*, 2393.
[9] a) F. Liu, D. Ding, C. Duan, *Adv. Sci.* **2023**, *10*, 2206478; b) Z. Li, J. Yu, C. Wang, I. T. Bello, N. Yu, X. Chen, K. Zheng, M. Han, M. Ni, *Appl. Energy* **2024**, *365*, 123236; c) C. Duan, *Nat. Catal.* **2021**, *4*, 264.
[10] H. Wang, M. Zhou, P. Choudhury, H. Luo, *Appl. Mater. Today* **2019**, *16*, 56.
[11] a) F. He, T. Wu, R. Peng, C. Xia, *J. Power Sources* **2009**, *194*, 263; b) M. Wang, C. Su, Z. Zhu, H. Wang, L. Ge, *Composites, Part B* **2022**, *238*, 109881; c) M. Papac, V. Stevanović, A. Zakutayev, R. O'Hayre, *Nat. Mater.* **2021**, *20*, 301.
[12] L. Lu, Y. Liu, H. Zhang, Y. Xu, H. Chen, *J. Mater. Chem. A* **2023**, *11*, 23613.
[13] a) M. B. Hanif, S. Rauf, Z. ul Abadeen, K. Khan, Z. Tayyab, S. Qayyum, M. Mosiałek, Z. Shao, C.-X. Li, M. J. M. Motola, *Matter* **2023**, *6*, 1782; b) S. Li, J. S. Irvine, *Solid State Ionics* **2021**, *361*, 115571.
[14] N. Wang, S. Hinokuma, T. Ina, H. Toriumi, M. Katayama, Y. Inada, C. Zhu, H. Habazaki, Y. Aoki, *Chem. Mater.* **2019**, *31*, 8383.
[15] T. Ueki, M. Watanabe, *Macromolecules* **2008**, *41*, 3739.
[16] Y. Jing, N. R. Aluru, *J. Power Sources* **2020**, *445*, 227327.
[17] K.-D. Kreuer, A. Rabenau, W. Weppner, *Angew. Chem., Int. Ed.* **1982**, *21*, 208.
[18] J. Kim, S. Sengodan, S. Kim, O. Kwon, Y. Bu, G. Kim, *Renewable Sustainable Energy Rev.* **2019**, *109*, 606.
[19] a) Z. Wang, W. Yang, Z. Zhu, R. Peng, X. Wu, C. Xia, Y. Lu, *J. Mater. Chem. A* **2014**, *2*, 16707; b) A. B. Muñoz-García, M. Pavone, *Chem. Mater.* **2016**, *28*, 490; c) C. Lan, H. Li, S. Zhao, *J. Comput. Electron.* **2020**, *19*, 905; d) H. Ding, W. Wu, C. Jiang, Y. Ding, W. Bian, B. Hu, P. Singh, C. J. Orme, L. Wang, Y. Zhang, D. Ding, *Nat. Commun.* **2020**, *11*, 1907; e) X. Xu, H. Wang, J. Ma, W. Liu, X. Wang, M. Fronzi, L. Bi, *J. Mater. Chem. A* **2019**, *7*, 18792.
[20] a) M. Yashima, T. Tsujiguchi, Y. Sakuda, Y. Yasui, Y. Zhou, K. Fujii, S. Torii, T. Kamiyama, S. J. Skinner, *Nat. Commun.* **2021**, *12*, 556; b) J. Schuett, T. K. Schultze, S. Grieshammer, *Chem. Mater.* **2020**, *32*, 4442.
[21] K. Matsuzaki, K. Saito, Y. Ikeda, Y. Nambu, M. Yashima, *J. Am. Chem. Soc.* **2024**, *146*, 18544.
[22] Q. Ji, L. Bi, J. Zhang, H. Cao, X. S. Zhao, *Energy Environ. Sci.* **2020**, *13*, 1408.
[23] a) M. S. D. Read, M. Saiful Islam, G. W. Watson, F. King, F. E. Hancock, *J. Mater. Chem.* **2000**, *10*, 2298; b) H. Zhu, P. Zhang, S. Dai, *ACS Catal.* **2015**, *5*, 6370; c) J. Zhu, A. Thomas, *Appl. Catal., B* **2009**, *92*, 225.
[24] D. N. Mueller, M. L. Machala, H. Bluhm, W. C. Chueh, *Nat. Commun.* **2015**, *6*, 6097.
[25] a) K. A. Stoerzinger, W. S. Choi, H. Jeen, H. N. Lee, Y. Shao-Horn, *J. Phys. Chem. Lett.* **2015**, *6*, 487; b) B.-Q. Li, C. Tang, H.-F. Wang, X.-L. Zhu, Q. Zhang, *Sci. Adv.* **2016**, *2*, 1600495; c) K. A. Stoerzinger, W. Lü, C. Li, Ariando, T. V., Y. Shao-Horn, *J. Phys. Chem. Lett.* **2015**, *6*, 1435.
[26] a) B. Hua, M. Li, Y.-F. Sun, Y.-Q. Zhang, N. Yan, J. Chen, T. Thundat, J. Li, J.-L. Luo, *Nano Energy* **2017**, *32*, 247; b) J. P. Brenet, *J. Power Sources* **1979**, *4*, 183.
[27] D. B. Meadowcroft, *Nature* **1970**, *226*, 847.
[28] a) X.-Z. Yuan, X. Li, W. Qu, D. G. Ivey, H. Wang, *ECS Trans.* **2011**, *35*, 11; b) Y. Xue, H. Miao, S. Sun, Q. Wang, S. Li, Z. Liu, *J. Power Sources* **2017**, *342*, 192.
[29] Y. Takeda, R. Kanno, T. Kondo, O. Yamamoto, H. Taguchi, M. Shimada, M. Koizumi, *J. Appl. Electrochem.* **1982**, *12*, 275.
[30] a) Y. Shin, K.-Y. Doh, S. H. Kim, J. H. Lee, H. Bae, S.-J. Song, D. Lee, *J. Mater. Chem. A* **2020**, *8*, 4784; b) X. Ding, Z. Gao, D. Ding, X. Zhao, H. Hou, S. Zhang, G. Yuan, *Appl. Catal., B* **2019**, *243*, 546; c) D. Huan, L. Zhang, X. Li, Y. Xie, N. Shi, S. Xue, C. Xia, R. Peng, Y. Lu, *ChemSusChem* **2020**, *13*, 4994.
[31] W. Zhou, J. Sunarso, *J. Phys. Chem. Lett.* **2013**, *4*, 2982.
[32] J. Du, T. Zhang, F. Cheng, W. Chu, Z. Wu, J. Chen, *Inorg. Chem.* **2014**, *53*, 9106.
[33] a) J. W. Han, B. Yildiz, *Energy Environ. Sci.* **2012**, *5*, 8598; b) Y. Chen, Y. Choi, S. Yoo, Y. Ding, R. Yan, K. Pei, C. Qu, L. Zhang, I. Chang, B. Zhao, Y. Zhang, H. Chen, Y. Chen, C. Yang, B. deGlee, R. Murphy, J. Liu, M. Liu, *Joule* **2018**, *2*, 938.
[34] H. Jalili, J. W. Han, Y. Kuru, Z. Cai, B. Yildiz, *J. Phys. Chem. Lett.* **2011**, *2*, 801.
[35] a) J.-I. Jung, S. Park, M.-G. Kim, J. Cho, *Adv. Energy Mater.* **2015**, *5*, 1501560; b) N.-L. Wu, W.-R. Liu, S.-J. Su, *Electrochim. Acta* **2003**, *48*, 1567; c) K. A. Stoerzinger, W. T. Hong, X. R. Wang, R. R. Rao, S. Bengaluru Subramanyam, C. Li, Ariando, T. V., Q. Liu, E. J. Crumlin, K. K. Varanasi, Y. Shao-Horn, *Chem. Mater.* **2017**, *29*, 9990.
[36] A. S. Nowick, Y. Du, K. C. Liang, *Solid State Ionics* **1999**, *125*, 303.
[37] N. Wang, S. Hinokuma, T. Ina, C. Zhu, H. Habazaki, Y. Aoki, *J. Mater. Chem. A* **2020**, *8*, 11043.
[38] R. Ren, Z. Wang, X. Meng, X. Wang, C. Xu, J. Qiao, W. Sun, K. Sun, *ACS Appl. Energy Mater.* **2020**, *3*, 4914.
[39] X. Wang, W. Li, C. Zhou, M. Xu, Z. Hu, C.-W. Pao, W. Zhou, Z. Shao, *ACS Appl. Mater. Interfaces* **2023**, *15*, 1339.
[40] P. Zhong, K. Toyoura, L. Jiang, L. Chen, S. A. Ismail, N. Hatada, T. Norby, D. Han, *Adv. Energy Mater.* **2022**, *12*, 2200392.
[41] Y. Huan, S. Chen, R. Zeng, T. Wei, D. Dong, X. Hu, Y. Huang, *Adv. Energy Mater.* **2019**, *9*, 1901573.
[42] a) E. N. Naumovich, V. V. Kharton, *J. Mol. Struct: Theochem.* **2010**, *946*, 57; b) J. Sunarso, S. Baumann, J. M. Serra, W. A. Meulenberg, S. Liu, Y. S. Lin, J. C. Diniz da Costa, *J. Membr. Sci.* **2008**, *320*, 13.

[43] a) A. Grimaud, O. Diaz-Morales, B. Han, W. T. Hong, Y.-L. Lee, L. Giordano, K. A. Stoerzinger, M. T. M. Koper, Y. Shao-Horn, *Nat. Chem.* **2017**, *9*, 457; b) J. S. Yoo, X. Rong, Y. Liu, A. Kolpak, *ACS Catal.* **2018**, *8*, 4628; c) K. Xiao, Y. Wang, P. Wu, L. Hou, Z.-Q. Liu, *Angew. Chem., Int. Ed.* **2023**, *62*, 202301408.
[44] B. Yin, Y. Li, N. Sun, X. Ji, Y. Huan, D. Dong, X. Hu, T. Wei, *Electrochim. Acta* **2021**, *370*, 137747.
[45] a) Y. Pan, X. Xu, Y. Zhong, L. Ge, Y. Chen, J.-P. M. Veder, D. Guan, R. O'Hayre, M. Li, G. Wang, H. Wang, W. Zhou, Z. Shao, *Nat. Commun.* **2002**, *11*, 2020. b) X. Xu, Y. Pan, Y. Zhong, C. Shi, D. Guan, L. Ge, Z. Hu, Y.-Y. Chin, H.-J. Lin, C.-T. Chen, H. Wang, S. P. Jiang, Z. Shao, *Adv. Sci.* **2022**, *9*, 2200530; c) N. Zhang, Y. Chai, *Energy Environ. Sci.* **2021**, *14*, 4647.
[46] a) X. Zhang, C. Pei, X. Chang, S. Chen, R. Liu, Z.-J. Zhao, R. Mu, J. Gong, *J. Am. Chem. Soc.* **2020**, *142*, 11540; b) Z. Wang, Y. Wang, Y. Xiao, Y. Zhang, X. Wang, F. Wang, T. He, *Small* **2024**, *20*, 2312148.
[47] K. D. Kreuer, *Annu. Rev. Mater. Res.* **2003**, *33*, 333.
[48] Y. Yamazaki, A. Kuwabara, J. Hyodo, Y. Okuyama, C. A. J. Fisher, S. M. Haile, *Chem. Mater.* **2020**, *32*, 7292.
[49] Z. Li, M. Li, Z. Zhu, *Electrochem. Energy Rev.* **2022**, *5*, 263.
[50] a) A. Chroneos, R. V. Vovk, I. L. Goulatis, L. I. Goulatis, *J. Alloys Compd.* **2010**, *494*, 190; b) A. B. Muñoz-García, A. M. Ritzmann, M. Pavone, J. A. Keith, E. A. Carter, *Acc. Chem. Res.* **2014**, *47*, 3340; c) A. Chroneos, B. Yildiz, A. Tarancón, D. Parfitt, J. A. Kilner, *Energy Environ. Sci.* **2011**, *4*, 2774.
[51] D. Chen, X. Jiao, R. Xu, *Mater. Res. Bull.* **1999**, *34*, 685.
[52] X. Geng, G. Hang, A. J. Fernández-Carrión, X. Ming, S. Deng, L. He, X. Kuang, X. Yang, *Inorg. Chem. Front.* **2024**, *11*, 5014.
[53] N. Tarasova, I. Animitsa, *Materials* **2022**, *15*, 114.
[54] C. J. Bartel, C. Sutton, B. R. Goldsmith, R. Ouyang, C. B. Musgrave, L. M. Ghiringhelli, M. Scheffler, *Sci. Adv.* **2019**, *5*, aav0693.
[55] a) H. Ullmann, N. Trofimenko, *J. Alloys Compd.* **2001**, *316*, 153; b) W. Li, J. Sunarso, Y. Yang, Y. Chen, C. Ge, W. Wang, Y. Guo, R. Ran, W. Zhou, *Energy Rev.* **2024**, *3*, 100085.
[56] a) D. Lybye, F. W. Poulsen, M. Mogensen, *Solid State Ionics* **2000**, *128*, 91; b) M. Yashima, *Solid State Ionics* **2008**, *179*, 797; c) J. Yang, Y. Lv, X. Xu, X. Song, H. Wei, M. Tian, J. Xu, *J. Mater. Chem. A* **2022**, *10*, 16697.
[57] S. Fop, K. S. McCombie, E. J. Wildman, J. M. S. Skakle, J. T. S. Irvine, P. A. Connor, C. Savaniu, C. Ritter, A. C. McLaughlin, *Nat. Mater.* **2020**, *19*, 752.
[58] N. Wang, C. Tang, L. Du, R. Zhu, L. Xing, Z. Song, B. Yuan, L. Zhao, Y. Aoki, S. Ye, *Adv. Energy Mater.* **2022**, *12*, 2201882.
[59] a) R. L. Cook, A. F. Sammells, *Solid State Ionics* **1991**, *45*, 311; b) A. F. Sammells, R. L. Cook, J. H. White, J. J. Osborne, R. C. MacDuff, *Solid State Ionics* **1992**, *52*, 111.
[60] a) H. Nishino, H. Yamamura, T. Arai, K. Kakinuma, K. Nomura, *J. Ceram. Soc. Jpn.* **2004**, *112*, 541; b) H. Yamamura, K. Matsui, K. Kakinuma, T. Mori, *Solid State Ionics* **1999**, *123*, 279.
[61] R. Gao, A. C. P. Jain, S. Pandya, Y. Dong, Y. Yuan, H. Zhou, L. R. Dedon, V. Thoréton, S. Saremi, R. Xu, A. Luo, T. Chen, V. Gopalan, E. Ertekin, J. Kilner, T. Ishihara, N. H. Perry, D. R. Trinkle, L. W. Martin, *Adv. Mater.* **2020**, *32*, 1905178.
[62] Y. Lu, H. Zhao, X. Chang, X. Du, K. Li, Y. Ma, S. Yi, Z. Du, K. Zheng, K. Świerczek, *J. Mater. Chem. A* **2016**, *4*, 10454.
[63] S. Hu, S. Gu, C. Yang, J. Cheng, J. Xu, J. Pu, B. Chi, *J. Power Sources* **2024**, *602*, 234389.
[64] a) A. M. Ritzmann, A. B. Muñoz-García, M. Pavone, J. A. Keith, E. A. Carter, *Chem. Mater.* **2013**, *25*, 3011; b) N. A. Szaro, S. C. Ammal, F. Chen, A. Heyden, *J. Power Sources* **2021**, *515*, 230602.
[65] H. Hayashi, H. Inaba, M. Matsuyama, N. G. Lan, M. Dokiya, H. Tagawa, *Solid State Ionics* **1999**, *122*, 1.
[66] E. Robens, R. Rauschen, J. Kaub, J. P. Parras, D. Kemp, C. L. Freeman, R. A. De Souza, *J. Mater. Chem. A* **2022**, *10*, 2388.
[67] Y.-R. Sun, X. Zhang, L.-G. Wang, Z.-K. Liu, N. Kang, N. Zhou, W.-L. You, J. Li, X.-F. Yu, *Chem. Eng. J.* **2021**, *421*, 129698.
[68] X. Xu, H. Wang, M. Fronzi, X. Wang, L. Bi, E. Traversa, *J. Mater. Chem. A* **2019**, *7*, 20624.
[69] Y. Yamazaki, R. Hernandez-Sanchez, S. M. Haile, *J. Mater. Chem.* **2010**, *20*, 8158.
[70] a) R. Ren, Z. Wang, C. Xu, W. Sun, J. Qiao, D. W. Rooney, K. Sun, *J. Mater. Chem. A* **2019**, *7*, 18365; b) Z. Wang, Y. Wang, J. Wang, Y. Song, M. J. Robson, A. Seong, M. Yang, Z. Zhang, A. Belotti, J. Liu, G. Kim, J. Lim, Z. Shao, F. Ciucci, *Nat. Catal.* **2022**, *5*, 777.
[71] a) H. Li, J. Li, X. Wang, C. Xie, Y. Wang, X. Ding, *ACS Appl. Energy Mater.* **2023**, *6*, 8966; b) Q. Ye, H. Ye, Z. Ma, H. Lin, B. Zhao, G. Yang, F. Dong, M. Ni, Z. Lin, S. Zhang, *Small* **2024**, *20*, 2307900.
[72] a) C. R. Kreller, B. P. Uberuaga, *Curr. Opin. Solid State Mater. Sci.* **2021**, *25*, 100899; b) A. Simonov, A. L. Goodwin, *Nat. Rev. Chem.* **2020**, *4*, 657.
[73] D. Parfitt, A. Chroneos, A. Tarancón, J. A. Kilner, *J. Mater. Chem.* **2011**, *21*, 2183.
[74] a) A. A. Taskin, A. N. Lavrov, Y. Ando, *Appl. Phys. Lett.* **2005**, *86*; b) A. A. Taskin, A. N. Lavrov, Y. Ando, *Prog. Solid State Chem.* **2007**, *35*, 481; c) D. Muñoz-Gil, D. Ávila-Brande, E. Urones-Garrote, S. García-Martín, *Dalton Trans.* **2015**, *44*, 10867.
[75] H. Shiiba, C. L. Bishop, M. J. D. Rushton, M. Nakayama, M. Nogami, J. A. Kilner, R. W. Grimes, *J. Mater. Chem. A* **2013**, *1*, 10345.
[76] H. Sun, S. Song, X. Xu, J. Dai, J. Yu, W. Zhou, Z. Shao, W. Jung, *Adv. Energy Mater.* **2021**, *11*, 2101937.
[77] A. I. Baranov, B. V. Merinov, A. V. Tregubchenko, V. P. Khiznichenko, L. A. Shuvalov, N. M. Schagina, *Solid State Ionics* **1989**, *36*, 279.
[78] C. Bernuy-Lopez, L. Rioja-Monllor, T. Nakamura, S. Ricote, R. O'Hayre, K. Amezawa, M.-A. Einarsrud, T. Grande, *Materials* **2018**, *11*, 196.
[79] D. Gryaznov, R. Merkle, E. A. Kotomin, J. Maier, *J. Mater. Chem. A* **2016**, *4*, 13093.
[80] a) R. Zohourian, R. Merkle, G. Raimondi, J. Maier, *Adv. Funct. Mater.* **2018**, *28*, 1801241; b) R. Zohourian, R. Merkle, J. Maier, *Solid State Ionics* **2017**, *299*, 64.
[81] a) S. G. Kang, D. S. Sholl, *J. Am. Ceram. Soc.* **2017**, *100*, 2997; b) B. Liu, Z. Li, X. Yang, D. Yan, J. Li, L. Jia, *J. Mater. Chem. A* **2022**, *10*, 17425; c) P. Qiu, B. Liu, L. Wu, H. Qi, B. Tu, J. Li, L. Jia, *J. Adv. Ceram.* **2022**, *11*, 1988.
[82] Y. Xiao, D. Bao, Z. Wang, Y. Wang, T. He, *Int. J. Hydrogen Energy* **2024**, *57*, 880.
[83] J. A. Dawson, J. A. Miller, I. Tanaka, *Chem. Mater.* **2015**, *27*, 901.
[84] C. Nicollet, H. L. Tuller, *Chem. Mater.* **2022**, *34*, 991.
[85] C. Nicollet, C. Toparli, G. F. Harrington, T. Defferriere, B. Yildiz, H. L. Tuller, *Nat. Catal.* **2020**, *3*, 913.
[86] a) D. Huan, N. Shi, L. Zhang, W. Tan, Y. Xie, W. Wang, C. Xia, R. Peng, Y. Lu, *ACS Appl. Mater. Interfaces* **2018**, *10*, 1761; b) Á. Triviño-Peláez, D. Pérez-Coll, J. Mosa, C. Ritter, U. Amador, G. C. Mather, *J. Power Sources* **2021**, *493*, 229691; c) E. Fabbri, L. Bi, D. Pergolesi, E. Traversa, *Adv. Mater.* **2012**, *24*, 195.
[87] R. Merkle, M. F. Hoedl, G. Raimondi, R. Zohourian, J. Maier, *Annu. Rev. Mater. Res.* **2021**, *51*, 461.
[88] T. S. Bjørheim, M. F. Hoedl, R. Merkle, E. A. Kotomin, J. Maier, *J. Phys. Chem. C* **2020**, *124*, 1277.
[89] a) J. Mizusaki, S. Yamauchi, K. Fueki, A. Ishikawa, *Solid State Ionics* **1984**, *12*, 119; b) M. H. R. Lankhorst, H. J. M. Bouwmeester, H. Verweij, *J. Solid State Chem.* **1997**, *133*, 555; c) J. Mizusaki, Y. Mima, S. Yamauchi, K. Fueki, H. Tagawa, *J. Solid State Chem.* **1989**, *80*, 102; d) R. Zohourian, R. Merkle, J. Maier, *ECS Trans.* **2017**, *77*, 133.
[90] a) D. Kim, S. Miyoshi, T. Tsuchiya, S. Yamaguchi, *Solid State Ionics* **2014**, *262*, 875; b) L. R. Tarutina, G. K. Vdovin, J. G. Lyagaeva, D. A. Medvedev, *J. Alloys Compd.* **2020**, *831*, 154895; c) A. Marthinsen, G. Wahnström, *Chem. Mater.* **2020**, *32*, 5558.

[91] a) J. Suntivich, H. A. Gasteiger, N. Yabuuchi, H. Nakanishi, J. B. Goodenough, Y. Shao-Horn, *Nat. Chem.* **2011**, *3*, 546; b) H. Jeen, W. S. Choi, M. D. Biegalski, C. M. Folkman, I. C. Tung, D. D. Fong, J. W. Freeland, D. Shin, H. Ohta, M. F. Chisholm, H. N. Lee, *Nat. Mater.* **2013**, *12*, 1057; c) Q. Wang, Y. Gu, W. Zhu, L. Han, F. Pan, C. Song, *Adv. Funct. Mater.* **2021**, *31*, 2106765; d) L. Zhang, W. Sun, C. Xu, R. Ren, X. Yang, J. Qiao, Z. Wang, K. Sun, *J. Mater. Chem. A* **2020**, *8*, 14091.

[92] a) R. A. De Souza, *Adv. Funct. Mater.* **2015**, *25*, 6326; b) D. Vivona, K. Gordiz, R. Meyer, S. Raman, Y. Shao-Horn, *J. Mater. Chem. A* **2024**, *12*, 22737.

[93] a) M. Pavone, A. M. Ritzmann, E. A. Carter, *Energy Environ. Sci.* **2011**, *4*, 4933; b) A. M. Deml, V. Stevanović, C. L. Muhich, C. B. Musgrave, R. O'Hayre, *Energy Environ. Sci.* **2014**, *7*, 1996; c) Y.-S. Zheng, M. Zhang, Q. Li, Y.-A. Zhu, Z.-J. Sui, D. Chen, X.-G. Zhou, *J. Phys. Chem. C* **2019**, *123*, 275; d) R. B. Wexler, G. S. Gautam, E. B. Stechel, E. A. Carter, *J. Am. Chem. Soc.* **2021**, *143*, 13212.

[94] a) Y.-L. Lee, J. Kleis, J. Rossmeisl, Y. Shao-Horn, D. Morgan, *Energy Environ. Sci.* **2011**, *4*, 3966; b) A. M. Deml, A. M. Holder, R. P. O'Hayre, C. B. Musgrave, V. Stevanović, *J. Phys. Chem. Lett.* **2015**, *6*, 1948.

[95] T. T. Mayeshiba, D. D. Morgan, *Solid State Ionics* **2016**, *296*, 71.

[96] V. V. Kharton, A. P. Viskup, D. M. Bochkov, E. N. Naumovich, O. P. Reut, *Solid State Ionics* **1998**, *110*, 61.

[97] G. Coffey, J. Hardy, O. Marina, L. Pederson, P. Rieke, E. Thomsen, *Solid State Ionics* **2004**, *175*, 73.

[98] a) J. C. Boivin, G. Mairesse, *Chem. Mater.* **1998**, *10*, 2870; b) T. Ishihara, H. Furutani, H. Arikawa, M. Honda, T. Akbay, Y. Takita, *J. Electrochem. Soc.* **1999**, *146*, 1643.

[99] G. Raimondi, R. Merkle, J. Maier, *Solid State Ionics* **2023**, *391*, 116143.

[100] Y. Zhang, G. Yang, G. Chen, R. Ran, W. Zhou, Z. Shao, *ACS Appl. Mater. Interfaces* **2016**, *8*, 3003.

[101] Z. Zhang, D. Chen, F. Dong, X. Xu, Y. Hao, Z. Shao, *J. Membr. Sci.* **2016**, *519*, 11.

[102] Y. Huan, M. Ma, Y. Su, D. Dong, X. Hu, T. Wei, *J. Materiomics* **2023**, *9*, 867.

[103] A. Niemczyk, R. Merkle, J. Maier, K. Świerczek, *J. Solid State Chem.* **2022**, *306*, 122731.

[104] Z. Sherafat, M. H. Paydar, I. Antunes, N. Nasani, A. D. Brandão, D. P. Fagg, *Electrochim. Acta* **2015**, *165*, 443.

[105] C. Sun, J. A. Alonso, J. Bian, *Adv. Energy Mater.* **2021**, *11*, 2000459.

[106] J.-H. Kim, A. Manthiram, *J. Mater. Chem. A* **2015**, *3*, 24195.

[107] a) X. Xu, Y. Pan, Y. Zhong, R. Ran, Z. Shao, *Mater. Horiz* **2020**, *7*, 2519; b) W. Zhang, X. Zhang, Y. Song, G. Wang, *Next Sustainability* **2024**, *3*, 100028.

[108] G. Amow, I. J. Davidson, S. J. Skinner, *Solid State Ionics* **2006**, *177*, 1205.

[109] a) D. Han, Y. Okumura, Y. Nose, T. Uda, *Solid State Ionics* **2010**, *181*, 1601; b) D. Hashimoto, D. Han, T. Uda, *Solid State Ionics* **2014**, *262*, 687.

[110] a) D. Poetzsch, R. Merkle, J. Maier, *Faraday Discuss.* **2015**, *182*, 129; b) D. Poetzsch, R. Merkle, J. Maier, *Phys. Chem. Chem. Phys.* **2014**, *16*, 16446.

[111] Y. Xie, N. Shi, D. Huan, W. Tan, J. Zhu, X. Zheng, H. Pan, R. Peng, C. Xia, *ChemSusChem* **2018**, *11*, 3423.

[112] X. Chen, N. Yu, I. T. Bello, D. Guan, Z. Li, T. Liu, T. Liu, Z. Shao, M. Ni, *Energy Stor. Mater.* **2023**, *63*, 103056.

[113] J. Tong, W. Yang, B. Zhu, R. Cai, *J. Membr. Sci.* **2002**, *203*, 175.

[114] M. Shang, J. Tong, R. O'Hayre, *RSC Adv.* **2013**, *3*, 15769.

[115] C. Duan, J. Tong, M. Shang, S. Nikodemski, M. Sanders, S. Ricote, A. Almansoori, R. O'Hayre, *Science* **2015**, *349*, 1321.

[116] J. H. Duffy, H. W. Abernathy, K. S. Brinkman, *J. Mater. Chem. A* **2023**, *11*, 8929.

[117] M. Liang, F. He, C. Zhou, Y. Chen, R. Ran, G. Yang, W. Zhou, Z. Shao, *Chem. Eng. J.* **2021**, *420*, 127717.

[118] a) Y. Xu, F. Hu, Y. Guo, J. Zhang, Y. Huang, W. Zhou, J. Sun, B. He, L. Zhao, *Sep. Purif. Technol.* **2022**, *297*, 121482; b) M. Liang, Y. Song, D. Liu, L. Xu, M. Xu, G. Yang, W. Wang, W. Zhou, R. Ran, Z. Shao, *Appl. Catal. B-Environ.* **2022**, *318*, 121868.

[119] S. Choi, S. Yoo, J. Kim, S. Park, A. Jun, S. Sengodan, J. Kim, J. Shin, H. Y. Jeong, Y. Choi, G. Kim, M. Liu, *Sci. Rep.* **2013**, *3*, 2426.

[120] A. Grimaud, F. Mauvy, J. M. Bassat, S. Fourcade, L. Rocheron, M. Marrony, J. C. Grenier, *J. Electrochem. Soc.* **2012**, *159*, B683.

[121] J. Kim, S. Sengodan, G. Kwon, D. Ding, J. Shin, M. Liu, G. Kim, *ChemSusChem* **2014**, *7*, 2811.

[122] S. Choi, T. C. Davenport, S. M. Haile, *Energy Environ. Sci.* **2019**, *12*, 206.

[123] S. Choi, C. J. Kucharczyk, Y. Liang, X. Zhang, I. Takeuchi, H.-I. Ji, S. M. Haile, *Nat. Energy* **2018**, *3*, 202.

[124] S. Im, M. A. Berk, S. Yang, B.-K. Kim, K. J. Yoon, J.-W. Son, J.-H. Lee, H.-I. Ji, *J. Mater. Chem. A* **2022**, *10*, 16127.

[125] A. Seong, J. Kim, D. Jeong, S. Sengodan, M. Liu, S. Choi, G. Kim, *Adv. Sci.* **2021**, *8*, 2004099.

[126] a) L. Jiang, T. Wei, R. Zeng, W.-X. Zhang, Y.-H. Huang, *J. Power Sources* **2013**, *232*, 279; b) H. Bai, Y. Zhang, J. Chu, Q. Zhou, H. Lan, J. Zhou, *ACS Appl. Mater. Interfaces* **2023**, *15*, 38581.

[127] a) M. Choi, S. J. Kim, W. Lee, *Ceram. Int.* **2021**, *47*, 7790; b) B. Koo, K. Kim, J. K. Kim, H. Kwon, J. W. Han, W. Jung, *Joule* **2018**, *2*, 1476.

[128] a) M. Yashima, M. Enoki, T. Wakita, R. Ali, Y. Matsushita, F. Izumi, T. Ishihara, *J. Am. Chem. Soc.* **2008**, *130*, 2762; b) A. Chroneos, D. Parfitt, J. A. Kilner, R. W. Grimes, *J. Mater. Chem.* **2010**, *20*, 266; c) D. M. Halat, R. Dervişoğlu, G. Kim, M. T. Dunstan, F. Blanc, D. S. Middlemiss, C. P. Grey, *J. Am. Chem. Soc.* **2016**, *138*, 11958; d) X. Li, N. A. Benedek, *Chem. Mater.* **2015**, *27*, 2647.

[129] A. Grimaud, F. Mauvy, J. Marc Bassat, S. Fourcade, M. Marrony, J. C. Grenier, *J. Mater. Chem.* **2012**, *22*, 16017.

[130] H. An, D. Shin, H.-I. Ji, *J. Korean Ceram. Soc* **2018**, *55*, 358.

[131] S. Yang, Y. Wen, J. Zhang, Y. Lu, X. Ye, Z. Wen, *Electrochim. Acta* **2018**, *267*, 269.

[132] L. Miao, J. Hou, Z. Gong, Z. Jin, W. Liu, *Int. J. Hydrogen Energy* **2019**, *44*, 7531.

[133] a) B. V. Beznosikov, K. S. Aleksandrov, *Crystallogr. Rep.* **2000**, *45*, 792; b) G. Yang, W. Jung, S.-J. Ahn, D. Lee, *Appl. Sci.* **2019**, *9*, 1030.

[134] L. Zhang, F. Yao, J. Meng, W. Zhang, H. Wang, X. Liu, J. Meng, H. Zhang, *J. Mater. Chem. A* **2019**, *7*, 18558.

[135] a) Q. Wang, J. Hou, Y. Fan, X. Xi, J. Li, Y. Lu, G. Huo, L. Shao, X. Fu, J. Luo, *J. Mater. Chem. A* **2020**, *8*, 7704; b) G. Amow, S. Skinner, *J. Solid State Electrochem.* **2006**, *10*, 538.

[136] M. Matvejeff, M. Lehtimäki, A. Hirasa, Y. H. Huang, H. Yamauchi, M. Karppinen, *Chem. Mater.* **2005**, *17*, 2775.

[137] Z. Wang, W. Yang, S. P. Shafi, L. Bi, Z. Wang, R. Peng, C. Xia, W. Liu, Y. Lu, *J. Mater. Chem. A* **2015**, *3*, 8405.

[138] N. Yu, I. T. Bello, X. Chen, T. Liu, Z. Li, Y. Song, M. Ni, *Nano-Micro Lett.* **2024**, *16*, 177.

[139] a) Q. Zeng, X. Zhang, W. Wang, D. Zhang, Y. Jiang, X. Zhou, B. Lin, *Catalysts* **2020**, *10*, 235; b) Q. Yang, H. Wu, K. Song, B. A. Beshiwork, X. Luo, D. Tian, S. Zhu, X. Lu, Y. Ding, Y. Chen, B. Lin, *Ceram. Int.* **2022**, *48*, 31418; c) L. Almar, H. Störmer, M. Meffert, J. Szász, F. Wankmüller, D. Gerthsen, E. Ivers-Tiffée, *ACS Appl. Energy Mater.* **2018**, *1*, 1316; d) L. Fang, F. Liu, D. Diercks, P. Kumar, F. Zhao, D. Ding, C. Duan, *J. Mater. Chem. A* **2023**, *11*, 21251; e) Y. Tian, J. Li, Y. Liu, J. Yang, B. Liu, L. Jia, J. Jiang, B. Chi, J. Pu, J. Li, *Int. J. Hydrogen Energy* **2018**, *43*, 12603; f) X. Kuai, G. Yang, Y. Chen, H. Sun, J. Dai, Y. Song, R. Ran, W. Wang, W. Zhou, Z. Shao, *Adv. Energy Mater.* **2019**, *9*, 1902384.

[140] T. Wu, R. Peng, C. Xia, *Solid State Ionics* **2008**, *179*, 1505.

[141] H. Ding, B. Lin, X. Liu, G. Meng, *Electrochem. Commun.* **2008**, *10*, 1388.
[142] H. Dai, E. H. Da'as, S. P. Shafi, H. Wang, L. Bi, *J. Eur. Ceram. Soc.* **2018**, *38*, 2903.
[143] L. Yang, C. Zuo, S. Wang, Z. Cheng, M. Liu, *Adv. Mater.* **2008**, *20*, 3280.
[144] J. Cui, J. Wang, X. Zhang, G. Li, K. Wu, Y. Cheng, J. Zhou, *J. Power Sources* **2019**, *413*, 148.
[145] E. Fabbri, S. Licoccia, E. Traversa, E. D. Wachsman, *Fuel Cells* **2009**, *9*, 128.
[146] C.-Y. Yoo, D. S. Yun, S.-Y. Park, J. Park, J. H. Joo, H. Park, M. Kwak, J. H. Yu, *Electrocatalysis* **2016**, *7*, 280.
[147] L. Yang, Z. Liu, S. Wang, Y. Choi, C. Zuo, M. Liu, *J. Power Sources* **2010**, *195*, 471.
[148] K. Watanabe, Y. Yamaguchi, K. Nomura, H. Sumi, M. Mori, Y. Mizutani, H. Shimada, *Ceram. Int.* **2023**, *49*, 21085.
[149] W. Zhou, R. Ran, Z. Shao, *J. Power Sources* **2009**, *192*, 231.
[150] G. Taillades, P. Pers, V. Mao, M. Taillades, *Int. J. Hydrogen Energy* **2016**, *41*, 12330.
[151] J. Seo, H.-W. Kim, J. H. Yu, H. J. Park, *J. Korean Ceram. Soc.* **2022**, *59*, 217.
[152] B. Liu, J. Yang, D. Yan, L. Jia, B. Chi, J. Pu, J. Li, *Int. J. Hydrogen Energy* **2020**, *45*, 31009.
[153] J. Chen, J. Li, L. Jia, I. Moussa, B. Chi, J. Pu, J. Li, *J. Power Sources* **2019**, *428*, 13.
[154] M. Li, M. Ni, F. Su, C. Xia, *J. Power Sources* **2014**, *260*, 197.
[155] W. Li, B. Guan, L. Ma, S. Hu, N. Zhang, X. Liu, *J. Mater. Chem. A* **2018**, *6*, 18057.
[156] A. P. Tarutin, J. G. Lyagaeva, A. S. Farlenkov, A. I. Vylkov, D. M. Medvedev, *Ceram. Int.* **2019**, *45*, 16105.
[157] Y. Bu, S. Joo, Y. Zhang, Y. Wang, D. Meng, X. Ge, G. Kim, *J. Power Sources* **2020**, *451*, 227812.
[158] H. Zhou, X. Yi, Y. Hui, L. Wang, W. Chen, Y. Qin, M. Wang, J. Ma, X. Chu, Y. Wang, X. Hong, Z. Chen, X. Meng, H. Wang, Q. Zhu, L. Song, A. Zheng, F.-S. Xiao, *Science* **2021**, *372*, 76.
[159] X. Li, Z. Chen, D. Huan, B. Qiu, K. Zhu, Z. Qi, H. Liu, C. Xia, R. Peng, Y. Lu, *ACS Mater. Lett.* **2023**, *5*, 2896.
[160] D. Ding, X. Li, S. Y. Lai, K. Gerdes, M. Liu, *Energy Environ. Sci.* **2014**, *7*, 552.
[161] a) Q. Wang, S. Ricote, M. Chen, *Electrochim. Acta* **2023**, *446*, 142101; b) P. Connor, X. Yue, C. Savaniu, R. Price, G. Triantafyllou, M. Cassidy, G. Kerherve, D. Payne, R. Maher, L. Cohen, R. Tomov, B. A. Glowacki, R. Kumar, J. S. Irvine, *Adv. Energy Mater.* **2018**, *8*, 1800120.
[162] N. Bausá, J. M. Serra, *RSC Adv.* **2019**, *9*, 20677.
[163] a) K. Pei, Y. Zhou, Y. Ding, K. Xu, H. Zhang, W. Yuan, K. Sasaki, Y. Choi, M. Liu, Y. Chen, *J. Power Sources* **2021**, *514*, 230573; b) K. Pei, Y. Zhou, K. Xu, Z. He, Y. Chen, W. Zhang, S. Yoo, B. Zhao, W. Yuan, M. Liu, Y. Chen, *Nano Energy* **2020**, *72*, 104704.
[164] J. Jing, Z. Lei, C. Wang, Z. Zheng, H. Wang, P. Zhang, Z. Yang, S. Peng, *ACS Sustainable Chem. Eng.* **2023**, *11*, 10303.
[165] G. Li, H. Jin, Y. Cui, L. Gui, B. He, L. Zhao, *J. Power Sources* **2017**, *341*, 192.
[166] Q. Wang, S. Ricote, P. V. Hendriksen, Y. Wang, J. Wang, M. Chen, *ECS Trans.* **2021**, *102*, 3.
[167] Q. Wang, X. Tong, S. Ricote, R. Sažinas, P. V. Hendriksen, M. Chen, *Adv. Powder Mater.* **2022**, *1*, 100003.
[168] Y. Zhou, W. Zhang, N. Kane, Z. Luo, K. Pei, K. Sasaki, Y. Choi, Y. Chen, D. Ding, M. Liu, *Adv. Funct. Mater.* **2021**, *31*, 2105386.
[169] Y. Niu, Y. Zhou, W. Zhang, Y. Zhang, C. Evans, Z. Luo, N. Kane, Y. Ding, Y. Chen, X. Guo, W. Lv, M. Liu, *Adv. Energy Mater.* **2022**, *12*, 2103783.
[170] K. Pei, S. Luo, F. He, J. Arbiol, Y. Xu, F. Zhu, Y. Wang, Y. Chen, *Appl. Catal., B* **2023**, *330*, 122601.
[171] Y.-M. Kim, X. Chen, S. P. Jiang, J. Bae, *Electrochem. Solid-State Lett.* **2011**, *14*, B41.
[172] H. Zhang, K. Xu, F. He, Y. Zhou, K. Sasaki, B. Zhao, Y. Choi, M. Liu, Y. Chen, *Adv. Energy Mater.* **2022**, *12*, 2200761.
[173] W. Zhang, H. Muroyama, Y. Mikami, T. Matsui, K. Eguchi, *J. Energy Chem.* **2023**, *87*, 450.
[174] H. Lee, H. Jung, C. Kim, S. Kim, I. Jang, H. Yoon, U. Paik, T. Song, *ACS Appl. Energy Mater.* **2021**, *4*, 11564.
[175] H. Gao, F. He, F. Zhu, J. Xia, Z. Du, Y. Huang, L. Zhu, Y. Chen, *Adv. Funct. Mater.* **2024**, *34*, 2401747.
[176] S. Guo, Y. Li, D. Han, *J. Electrochem. Soc.* **2023**, *170*, 034506.
[177] a) L. Zhang, T. Hong, Y. Li, C. Xia, *Int. J. Hydrogen Energy* **2017**, *42*, 17242; b) Y. Yang, M. Li, Y. Ren, Y. Li, C. Xia, *Int. J. Hydrogen Energy* **2018**, *43*, 3797; c) T. Hong, K. S. Brinkman, C. Xia, *ChemElectroChem* **2016**, *3*, 805.
[178] B. Qiu, K. Zhu, Y. Yang, L. Ye, L. Zhang, C. Xia, R. Peng, Y. Lu, *J. Mater. Chem. A* **2024**, *12*, 21373.
[179] P. Qiu, X. Yang, T. Zhu, S. Sun, L. Jia, J. Li, *Int. J. Hydrogen Energy* **2020**, *45*, 23160.
[180] Y. Gao, M. Zhang, M. Fu, W. Hu, H. Tong, Z. Tao, *Energy Reviews* **2023**, *2*, 100038.
[181] a) N. Ai, K. Chen, *Int. J. Hydrog. Energy* **2017**, *42*, 7246; b) Z. Zhang, J. Wang, Y. Chen, S. Tan, Z. Shao, D. Chen, *J. Power Sources* **2018**, *385*, 76; c) J. Li, B. Liu, L. Jia, B. Chi, J. Pu, J. Li, S. Wang, *Int. J. Hydrog. Energy* **2019**, *44*, 26489.
[182] W. Zhang, Y. H. Hu, *Catal. Today* **2023**, *409*, 71.
[183] C. Geng, H. Wu, Y. Yang, B. Wei, T. Hong, J. Cheng, *ACS Sustainable Chem. Eng.* **2021**, *9*, 11070.
[184] Y. Lu, M. A. K. Yousaf Shah, B. S. Almutairi, N. Mushtaq, M. Yousaf, N. Akbar, N. Arshad, M. S. Irshad, Y. Dong, *J. Alloys Compd.* **2023**, *960*, 170861.
[185] J. Hou, J. Gong, J.-L. Luo, *Chem. Eng. J.* **2023**, *459*, 141459.
[186] a) W. Lee, J. W. Han, Y. Chen, Z. Cai, B. Yildiz, *J. Am. Chem. Soc.* **2013**, *135*, 7909; b) Y. Chen, H. Téllez, M. Burriel, F. Yang, N. Tsvetkov, Z. Cai, D. W. McComb, J. A. Kilner, B. Yildiz, *Chem. Mater.* **2015**, *27*, 5436.
[187] T. J. Quill, G. LeCroy, D. M. Halat, R. Sheelamanthula, A. Marks, L. S. Grundy, I. McCulloch, J. A. Reimer, N. P. Balsara, A. Giovannitti, A. Salleo, C. J. Takacs, *Nat. Mater.* **2023**, *22*, 362.
[188] Y. Song, Y. Song, Y. Wang, Y. Tian, J. Li, M. Xu, Z. Shao, F. Ciucci, *Adv. Funct. Mater.* **2024**, *34*, 2405851.
[189] J. H. Kim, K. Jang, D.-K. Lim, S. Ahn, D. Oh, H. Kim, J. Seo, P.-P. Choi, W. Jung, *J. Mater. Chem. A* **2022**, *10*, 2496.
[190] Y. Song, Y. Chen, W. Wang, C. Zhou, Y. Zhong, G. Yang, W. Zhou, M. Liu, Z. Shao, *Joule* **2019**, *3*, 2842.
[191] W. Zhang, H. Muroyama, Y. Mikami, Q. Liu, X. Liu, T. Matsui, K. Eguchi, *Chem. Eng. J.* **2023**, *461*, 142056.
[192] H. Tong, M. Fu, Y. Yang, F. Chen, Z. Tao, *Adv. Funct. Mater.* **2022**, *32*, 2209695.
[193] C. Berger, E. Bucher, R. Merkle, C. Nader, J. Lammer, W. Grogger, J. Maier, W. Sitte, *J. Mater. Chem. A* **2022**, *10*, 2474.
[194] D. Zou, Y. Yi, Y. Song, D. Guan, M. Xu, R. Ran, W. Wang, W. Zhou, Z. Shao, *J. Mater. Chem. A* **2022**, *10*, 5381.
[195] I. T. Bello, N. Yu, Y. Song, J. Wang, T.-S. Chan, S. Zhao, Z. Li, Y. Dai, J. Yu, M. Ni, *Small* **2022**, *18*, 2203207.
[196] a) N. Yu, T. Liu, X. Chen, M. Miao, M. Ni, Y. Wang, *Sep. Purif. Technol.* **2022**, *291*, 120890; b) B.-W. Zhang, M.-N. Zhu, M. Gao, J. Chen, X. Xi, J. Shen, R.-F. Feng, N. Semagina, N. Duan, H. Zeng, J. Luo, *Angew. Chem., Int. Ed.* **2023**, *62*, 202305552; c) N. Yu, G. Jiang, T. Liu, X. Chen, M. Miao, Y. Zhang, Y. Wang, *Sustainable Energy Fuels* **2021**, *5*, 401; d) M. Xu, Y. Jeon, A. Naden, H. Kim, G. Kerherve, D. J. Payne, Y.-g. Shul, J. T. S. Irvine, *Nat. Commun.* **2024**, *15*, 4007.
[197] a) J. H. Kim, S. Yoo, R. Murphy, Y. Chen, Y. Ding, K. Pei, B. Zhao, G. Kim, Y. Choi, M. Liu, *Energy Environ. Sci.* **2021**, *14*, 1506; b) Y. Zhou,

E. Liu, Y. Chen, Y. Liu, L. Zhang, W. Zhang, Z. Luo, N. Kane, B. Zhao, L. Soule, Y. Niu, Y. Ding, H. Ding, D. Ding, M. Liu, *ACS Energy Lett.* **2021**, *6*, 1511.

[198] K. Xu, H. Zhang, Y. Xu, F. He, Y. Zhou, Y. Pan, J. Ma, B. Zhao, W. Yuan, Y. Chen, M. Liu, *Adv. Funct. Mater.* **2022**, *32*, 2110998.

[199] K. Pei, Y. Zhou, K. Xu, H. Zhang, Y. Ding, B. Zhao, W. Yuan, K. Sasaki, Y. Choi, Y. Chen, M. Liu, *Nat. Commun.* **2022**, *13*, 2207.

[200] E. Vøllestad, R. Strandbakke, M. Tarach, D. Catalán-Martínez, M.-L. Fontaine, D. Beeaff, D. R. Clark, J. M. Serra, T. Norby, *Nat. Mater.* **2019**, *18*, 752.

[201] K. Park, M. Saqib, H. Lee, D. Shin, M. Jo, K. M. Park, M. Hamayun, S. H. Kim, S. Kim, K.-S. Lee, R. O'Hayre, M. Choi, S.-J. Song, J.-Y. Park, *Energy Environ. Sci.* **2024**, *17*, 1175.

[202] J. H. Kim, J. Hong, D.-K. Lim, S. Ahn, J. Kim, J. K. Kim, D. Oh, S. Jeon, S.-J. Song, W. Jung, *Energy Environ. Sci.* **2022**, *15*, 1097.

[203] F. He, S. Liu, T. Wu, M. Yang, W. Li, G. Yang, F. Zhu, H. Zhang, K. Pei, Y. Chen, W. Zhou, Z. Shao, *Adv. Funct. Mater.* **2022**, *32*, 2206756.

[204] K. Zhu, L. Zhang, N. Shi, B. Qiu, X. Hu, D. Huan, C. Xia, R. Peng, Y. Lu, *ACS Nano* **2024**, *18*, 5141.

[205] Y. Song, J. Liu, Y. Wang, D. Guan, A. Seong, M. Liang, M. J. Robson, X. Xiong, Z. Zhang, G. Kim, Z. Shao, F. Ciucci, *Adv. Energy Mater.* **2021**, *11*, 2101899.

[206] a) M. Liang, Y. Wang, Y. Song, D. Guan, J. Wu, P. Chen, A. Maradesa, M. Xu, G. Yang, W. Zhou, W. Wang, R. Ran, F. Ciucci, Z. Shao, *Appl. Catal., B* **2023**, *331*, 122682; b) M. Liang, Y. Zhu, Y. Song, D. Guan, Z. Luo, G. Yang, S. P. Jiang, W. Zhou, R. Ran, Z. Shao, *Adv. Mater.* **2022**, *34*, 2106379.

[207] a) O. Kwon, S. Sengodan, K. Kim, G. Kim, H. Y. Jeong, J. Shin, Y.-W. Ju, J. W. Han, G. Kim, *Nat. Commun.* **2017**, *8*, 15967; b) S. Joo, A. Seong, O. Kwon, K. Kim, J. H. Lee, R. J. Gorte, J. M. Vohs, J. W. Han, G. Kim, *Sci. Adv.* **2020**, *6*, abb1573. c) S. Joo, O. Kwon, K. Kim, S. Kim, H. Kim, J. Shin, H. Y. Jeong, S. Sengodan, J. W. Han, G. Kim, *Nat. Commun.* **2019**, *10*, 697.

[208] X. Chen, N. Yu, Y. Song, T. Liu, H. Xu, D. Guan, Z. Li, W.-H. Huang, Z. Shao, F. Ciucci, M. Ni, *Adv. Mater.* **2024**, *36*, 2403998.

[209] P. Yao, J. Zhang, Q. Qiu, Y. Zhao, F. Yu, Y. Li, *J. Power Sources* **2024**, *606*, 234591.

[210] a) H. Xiang, Y. Xing, F.-z. Dai, H. Wang, L. Su, L. Miao, G. Zhang, Y. Wang, X. Qi, L. Yao, H. Wang, B. Zhao, J. Li, Y. Zhou, *J. Adv. Ceram.* **2021**, *10*, 385; b) Y. Wang, J. Liu, Y. Song, J. Yu, Y. Tian, M. J. Robson, J. Wang, Z. Zhang, X. Lin, G. Zhou, Z. Wang, L. Shen, H. Zhao, S. Grasso, F. Ciucci, *Small Methods* **2023**, *7*, 2201138; c) D. Zhang, Y. Wang, Y. Peng, Y. Luo, T. Liu, W. He, F. Chen, M. Ding, *Adv. Powder Mater.* **2023**, *2*, 100129.

[211] a) B. Cantor, I. T. H. Chang, P. Knight, A. J. B. Vincent, *Mater. Sci. Eng., A* **2004**, *375–377*, 213; b) J. W. Yeh, S. K. Chen, S. J. Lin, J. Y. Gan, T. S. Chin, T. T. Shun, C. H. Tsau, S. Y. Chang, *Adv. Eng. Mater.* **2004**, *6*, 299.

[212] a) Y. Wang, M. J. Robson, A. Manzotti, F. Ciucci, *Joule* **2023**, *7*, 848; b) S. Jiang, T. Hu, J. Gild, N. Zhou, J. Nie, M. Qin, T. Harrington, K. Vecchio, J. Luo, *Scripta Mater* **2018**, *142*, 116; c) O. F. Dippo, K. S. Vecchio, *Scripta Mater* **2021**, *201*, 113974.

[213] P. A. Krawczyk, M. Jurczyszyn, J. Pawlak, W. Salamon, P. Baran, A. Kmita, Ł. Gondek, M. Sikora, C. Kapusta, T. Strączek, J. Wyrwa, A. Żywczak, *ACS Appl. Electron. Mater.* **2020**, *2*, 3211.

[214] W. Yang, Z. Han, G. Zheng, *Scripta Mater.* **2021**, *203*, 114096.

[215] C. M. Rost, E. Sachet, T. Borman, A. Moballegh, E. C. Dickey, D. Hou, J. L. Jones, S. Curtarolo, J.-P. Maria, *Nat. Commun.* **2015**, *6*, 8485.

[216] a) G. M. Tomboc, X. Zhang, S. Choi, D. Kim, L. Y. S. Lee, K. Lee, *Adv. Funct. Mater.* **2022**, *32*, 2270242; b) Z.-Y. Liu, Y. Liu, Y. Xu, H. Zhang, Z. Shao, Z. Wang, H. Chen, *Green Energy Environ.* **2023**, *8*, 1341; c) M.-H. Tsai, J.-W. Yeh, *Mater. Res. Lett.* **2014**, *2*, 107; d) Y. Jiao, J. Dai, Z. Fan, J. Cheng, G. Zheng, L. Grema, J. Zhong, H.-F. Li, D. Wang, *Mater. Today* **2024**, *77*, 92.

[217] a) Y. Zheng, M. Zou, W. Zhang, D. Yi, J. Lan, C.-W. Nan, Y.-H. Lin, *J. Adv. Ceram.* **2021**, *10*, 377; b) F. Baiutti, F. Chiabrera, M. Acosta, D. Diercks, D. Parfitt, J. Santiso, X. Wang, A. Cavallaro, A. Morata, H. Wang, A. Chroneos, J. MacManus-Driscoll, A. Tarancon, *Nat. Commun.* **2021**, *12*, 2660; c) R. Zhang, C. Wang, P. Zou, R. Lin, L. Ma, L. Yin, T. Li, W. Xu, H. Jia, Q. Li, S. Sainio, K. Kisslinger, S. E. Trask, S. N. Ehrlich, Y. Yang, A. M. Kiss, M. Ge, B. J. Polzin, S. J. Lee, W. Xu, Y. Ren, H. L. Xin, *Nature* **2022**, *610*, 67; d) Y. Sun, S. Dai, *Sci. Adv.* **2021**, *7*, abg1600.

[218] Y. Xu, X. Xu, L. Bi, *J. Adv. Ceram.* **2022**, *11*, 794.

[219] J. Sun, R. Ren, H. Yue, W. Cui, G. Wang, C. Xu, J. Qiao, W. Sun, K. Sun, Z. Wang, *Chin. Chem. Lett.* **2023**, *34*, 107776.

[220] C. Yang, J. Li, S. Hu, J. Pu, B. Chi, *Ceram. Int.* **2023**, *49*, 38331.

[221] J. Gong, J. Hou, *J. Mater. Sci. Technol.* **2024**, *186*, 158.

[222] Z. Liu, Z. Tang, Y. Song, G. Yang, W. Qian, M. Yang, Y. Zhu, R. Ran, W. Wang, W. Zhou, Z. Shao, *Nano-Micro Lett.* **2022**, *14*, 217.

[223] F. He, Y. Zhou, T. Hu, Y. Xu, M. Hou, F. Zhu, D. Liu, H. Zhang, K. Xu, M. Liu, Y. Chen, *Adv. Mater.* **2023**, *35*, 2209469.

[224] F. He, M. Hou, D. Liu, Y. Ding, K. Sasaki, Y. Choi, S. Guo, D. Han, Y. Liu, M. Liu, Y. Chen, *Energy Environ. Sci.* **2024**, *17*, 3898.

[225] a) I. Cho, J. Yun, B. Seong, J. Kim, S. H. Choi, H.-I. Ji, S. Choi, *J. Energy Chem.* **2024**, *88*, 1; b) D. Hu, J. Kim, H. Niu, L. M. Daniels, T. D. Manning, R. Chen, B. Liu, R. Feetham, J. B. Claridge, M. J. Rosseinsky, *J. Mater. Chem. A* **2022**, *10*, 2559.

[226] a) G. Zhou, Y. Li, Y. Luo, X. Wang, Y. Ding, *J. Alloys Compd.* **2024**, *971*, 172668; b) R. Guo, T. He, *ACS Mater. Lett.* **2022**, *4*, 1646. c) M. Wang, Y. Hua, Y. Gu, Y. Yin, L. Bi, *Ceram. Int.* **2024**, *50*, 4204.

[227] a) H. Li, J. Lai, Z. Li, L. Wang, *Adv. Funct. Mater.* **2021**, *31*, 2106715; b) J. Hao, Z. Zhuang, K. Cao, G. Gao, C. Wang, F. Lai, S. Lu, P. Ma, W. Dong, T. Liu, M. Du, H. Zhu, *Nat. Commun.* **2022**, *13*, 2662.

[228] a) W.-L. Hsu, C.-W. Tsai, A.-C. Yeh, J.-W. Yeh, *Nat. Rev. Chem.* **2024**, *8*, 471; b) S. S. Aamlid, M. Oudah, J. Rottler, A. M. Hallas, *J. Am. Chem. Soc.* **2023**, *145*, 5991.

[229] a) Y. Ma, Y. Ma, Q. Wang, S. Schweidler, M. Botros, T. Fu, H. Hahn, T. Brezesinski, B. Breitung, *Energy Environ. Sci.* **2021**, *14*, 2883; b) E. P. George, D. Raabe, R. O. Ritchie, *Nat. Rev. Mater.* **2019**, *4*, 515; c) S. Akrami, P. Edalati, M. Fuji, K. Edalati, *Mat Sci Eng R* **2021**, *146*, 100644; d) M. Gazda, T. Miruszewski, D. Jaworski, A. Mielewczyk-Gryń, W. Skubida, S. Wachowski, P. Winiarz, K. Dzierzgowski, M. Łapiński, I. Szpunar, E. Dzik, *ACS Mater. Lett.* **2020**, *2*, 1315.

[230] A. Amiri, R. Shahbazian-Yassar, *J. Mater. Chem. A* **2021**, *9*, 782.

[231] a) X. Chen, J. Wang, N. Yu, Y. Wang, D. Zhang, M. Ni, F. Chen, T. Liu, M. Ding, *J. Membr. Sci.* **2023**, *677*, 121637; b) X. Chen, N. Yu, I. T. Bello, D. Zhang, J. Zhou, Y. Wang, M. Ni, T. Liu, *Sep. Purif. Technol.* **2023**, *325*, 124713; c) A. Seong, J. Kim, J. Kim, S. Kim, S. Sengodan, J. Shin, G. Kim, *J. Electrochem. Soc.* **2018**, *165*, F1098.

[232] D. Zhang, J. Zhou, Y. Luo, Y. Wang, X. Zhang, X. Chen, T. Liu, M. Ding, *J. Power Sources* **2023**, *587*, 233705.

[233] S. Lee, S. Park, S. Wee, H. w. Baek, D. Shin, *Solid State Ionics* **2018**, *320*, 347.

[234] S. Park, S. Lee, H. Baek, D. Shin, *J. Electroceram.* **2020**, *45*, 1.

[235] a) R. K. Sharma, N. I. Khamidy, L. Rapenne, F. Charlot, H. Moussaoui, J. Laurencin, E. Djurado, *J. Power Sources* **2019**, *419*, 171; b) R. K. Sharma, E. Djurado, *J. Mater. Chem. A* **2018**, *6*, 10787.

[236] K. Develos-Bagarinao, T. Ishiyama, H. Kishimoto, H. Shimada, K. Yamaji, *Nat. Commun.* **2021**, *12*, 3979.

[237] K. Bae, D. Y. Jang, H. J. Choi, D. Kim, J. Hong, B.-K. Kim, J.-H. Lee, J.-W. Son, J. H. Shim, *Nat. Commun.* **2017**, *8*, 14553.

[238] K. Bae, H.-S. Noh, D. Y. Jang, J. Hong, H. Kim, K. J. Yoon, J.-H. Lee, B.-K. Kim, J. H. Shim, J.-W. Son, *J. Mater. Chem. A* **2016**, *4*, 6395.

[239] a) J. S. Park, H. J. Choi, G. D. Han, J. Koo, E. H. Kang, D. H. Kim, K. Bae, J. H. Shim, *J. Power Sources* **2021**, *482*, 229043; b) J. H. Shim, S.

Kang, S.-W. Cha, W. Lee, Y. B. Kim, J. S. Park, T. M. Gür, F. B. Prinz, C.-C. Chao, J. An, *J. Mater. Chem. A* **2013**, *1*, 12695.
[240] H. S. Park, H. J. Jeong, K.-h. Kim, W. Chang, Y. S. Kim, Y. S. Choi, J. H. Shim, *Appl. Surf. Sci.* **2023**, *612*, 155812.
[241] H. Tian, Z. Luo, Y. Song, Y. Zhou, M. Gong, W. Li, Z. Shao, M. Liu, X. Liu, *Int. Mater. Rev.* **2023**, *68*, 272.
[242] W. Wu, H. Ding, Y. Zhang, Y. Ding, P. Katiyar, P. K. Majumdar, T. He, D. Ding, *Adv. Sci.* **2018**, *5*, 1800360.
[243] W. Bian, W. Wu, Y. Gao, J. Gomez, H. Ding, W. Tang, M. Zhou, D. Ding, *Adv. Funct. Mater.* **2021**, *31*, 2102907.
[244] J. Cui, Y. Zhang, Z. Liu, Z. Hu, H.-P. Wang, P.-Y. Cho, C.-Y. Kuo, Y.-Y. Chin, C.-T. Chen, J. Zhu, J. Zhou, G. Kim, J.-Q. Wang, L. Zhang, *Small Struct.* **2024**, *5*, 2300439.
[245] M. Choi, D. Kim, T. K. Lee, J. Lee, H. S. Yoo, W. Lee, *Adv. Energy Mater.* **2024**, *15*, 2400124.
[246] W. Bian, W. Wu, B. Wang, W. Tang, M. Zhou, C. Jin, H. Ding, W. Fan, Y. Dong, J. Li, D. Ding, *Nature* **2022**, *604*, 479.
[247] C. Lee, S. S. Shin, J. Kim, J. Choi, M. Choi, H. H. Shin, *ACS Appl. Mater. Interfaces* **2022**, *14*, 32124.
[248] a) W. Wu, C. Wang, W. Bian, B. Hua, J. Y. Gomez, C. J. Orme, W. Tang, F. F. Stewart, D. Ding, *Adv. Sci.* **2023**, *10*, 2304074; b) C. Chen, Y. Zuo, W. Ye, X. Li, Z. Deng, S. P. Ong, *Adv. Energy Mater.* **2020**, *10*, 1903242; c) B. Weng, Z. Song, R. Zhu, Q. Yan, Q. Sun, C. G. Grice, Y. Yan, W.-J. Yin, *Nat. Commun.* **2020**, *11*, 3513; d) A. Chen, X. Zhang, Z. Zhou, *InfoMat* **2020**, *2*, 553.
[249] a) R. Jacobs, J. Liu, H. Abernathy, D. Morgan, *Adv. Mater.* **2024**, *14*, 2303684; b) H. Xin, *Nat. Energy* **2022**, *7*, 790.
[250] S. Zhai, H. Xie, P. Cui, D. Guan, J. Wang, S. Zhao, B. Chen, Y. Song, Z. Shao, M. Ni, *Nat. Energy* **2022**, *7*, 866.
[251] a) B. Yuan, N. Wang, C. Tang, L. Meng, L. Du, Q. Su, Y. Aoki, S. Ye, *Nano Energy* **2024**, *122*, 109306; b) C. Zhou, J. Sunarso, Y. Song, J. Dai, J. Zhang, B. Gu, W. Zhou, Z. Shao, *J. Mater. Chem. A* **2019**, *7*, 13265; c) J. Song, S. Zhu, D. Ning, H. J. M. Bouwmeester, *J. Mater. Chem. A* **2021**, *9*, 974.
[252] P. Priya, N. R. Aluru, *Npj Comput. Mater.* **2021**, *7*, 90.
[253] N. Wang, B. Yuan, C. Tang, L. Du, R. Zhu, Y. Aoki, W. Wang, L. Xing, S. Ye, *Adv. Mater.* **2022**, *34*, 2203446.
[254] Z. Li, H. Zhang, H. Xu, J. Xuan, *Renewable Sustainable Energy Rev.* **2021**, *141*, 110863.
[255] K. Toyoura, W. Meng, D. Han, T. Uda, *J. Mater. Chem. A* **2018**, *6*, 22721.
[256] F. M. Draber, C. Ader, J. P. Arnold, S. Eisele, S. Grieshammer, S. Yamaguchi, M. Martin, *Nat. Mater.* **2020**, *19*, 338.
[257] X. Hu, Y. Zhou, Z. Luo, H. Li, N. Shi, Z. Liu, W. Zhang, W. Wang, Y. Ding, M. Liu, *Energy Environ. Sci.* **2024**, *17*, 9335.
[258] C. Zhou, X. Wang, D. Liu, M. Fei, J. Dai, D. Guan, Z. Hu, L. Zhang, Y. Wang, W. Wang, R. O'Hayre, S. P. Jiang, W. Zhou, M. Liu, Z. Shao, *Energy Environ. Mater.* **2024**, *7*, 12660.
[259] Z. Yu, L. Ge, Q. Ni, Y. Zheng, H. Chen, X. Zhou, Y. Mi, B. Shi, X. Yu, B. Wu, L. Bi, Y. Zhu, *Adv. Funct. Mater.* **2024**, *34*, 2309698.
[260] Z. Liu, Y. Bai, H. Sun, D. Guan, W. Li, W.-H. Huang, C.-W. Pao, Z. Hu, G. Yang, Y. Zhu, R. Ran, W. Zhou, Z. Shao, *Nat. Commun.* **2024**, *15*, 472.
[261] A. Tahir, A. Belotti, Y. Song, Y. Wang, A. Maradesa, J. Li, Y. Tian, F. Ciucci, *ACS Appl. Mater. Interfaces* **2024**, *16*, 44645.
[262] Y. Feng, Y. Shen, F. Wang, C. Tian, Q. Hu, Q. Duan, J. Li, D. Bao, *Rare Met.* **2024**, *43*, 3055.
[263] Z. Liu, Y. Lin, H. Nie, D. Liu, Y. Li, X. Zhao, T. Li, G. Yang, Y. Sun, Y. Zhu, W. Wang, R. Ran, W. Zhou, Z. Shao, *Adv. Funct. Mater.* **2024**, *34*, 2311140.
[264] D. Kim, I. Jeong, S. Ahn, S. Oh, H. Im, H. Bae, S. Song, C. Lee, W. Jung, K. Lee, *Adv. Energy Mater.* **2024**, *14*, 2304059.
[265] J. Xia, M. Zhou, H. Gao, F. He, Z. Du, Y. Chen, *Adv. Funct. Mater.* **2024**, *34*, 2403493.
[266] K. Xu, H. Zhang, Y. Xu, D. Liu, F. Zhu, F. He, Y. Liu, H. Wang, Y. Chen, *Adv. Powder Mater.* **2024**, *3*, 100187.
[267] J. Gong, L. Xu, W. Zhu, L. Xie, X. Chen, X. Liu, *ACS Sustainable Chem. Eng.* **2024**, *12*, 3757.
[268] Z. Du, F. He, H. Gao, Y. Xu, F. Zhu, K. Xu, J. Xia, H. Zhang, Y. Huang, Y. Liu, Y. Chen, *Energy Storage Mater.* **2024**, *68*, 103345.
[269] Z. Wang, Y. Xiao, Y. Zhang, Y. Wang, X. Wang, F. Wang, T. He, *Chem. Eng. J.* **2024**, *490*, 151911.
[270] S. Zhao, W. Ma, W. Wang, Y. Huang, J. Wang, S. Wang, Z. Shu, B. He, L. Zhao, *Adv. Mater.* **2024**, *36*, 2405052.
[271] L. Wu, J. Sun, H. Qi, B. Tu, C. Xiong, F. Chen, P. Qiu, *J. Mater. Chem. A* **2024**, *12*, 25979.
[272] Y. Xu, K. Xu, F. Zhu, F. He, H. Zhang, C. Fang, Y. Liu, Y. Zhou, Y. Choi, Y. Chen, *ACS Energy Lett.* **2023**, *8*, 4145.
[273] J. Xia, F. Zhu, F. He, K. Xu, Y. Choi, Y. Chen, *Adv. Energy Mater.* **2023**, *13*, 2302964.
[274] L. Chen, J. Jing, P. Lun, P. Zhang, Z. Zheng, H. Wang, Z. Yang, *Int. J. Hydrogen Energy* **2023**, *48*, 39981.
[275] C. Lu, R. Ren, Z. Zhu, G. Pan, G. Wang, C. Xu, J. Qiao, W. Sun, Q. Huang, H. Liang, Z. Wang, K. Sun, *Chem. Eng. J.* **2023**, *472*, 144878.
[276] Y. Liu, S. Jiang, H. Qiu, W. Wang, E. Miller, C. Su, *Catalysts* **2023**, *13*, 793.
[277] Y. Xie, N. Shi, X. Hu, K. Zhu, R. Peng, C. Xia, M. Chen, *J. Electrochem. Soc.* **2023**, *170*, 024513.
[278] I. T. Bello, Y. Song, N. Yu, Z. Li, S. Zhao, A. Maradesa, T. Liu, Z. Shao, M. Ni, *J. Power Sources* **2023**, *560*, 232722.
[279] G.-M. Park, K. Park, M. Jo, M. Asif, Y. Bae, S.-H. Kim, A. K. Azad, S.-J. Song, J.-Y. Park, *J. Alloys Compd.* **2023**, *968*, 171987.
[280] J. H. Kim, D. Kim, S. Ahn, K. J. Kim, S. Jeon, D.-K. Lim, J. K. Kim, U. Kim, H.-N. Im, B. Koo, K. T. Lee, W. Jung, *Energy Environ. Sci.* **2023**, *16*, 3803.
[281] W. Tang, H. Ding, W. Bian, C. Y. Regalado Vera, J. Y. Gomez, Y. Dong, J. Li, W. Wu, W. Fan, M. Zhou, C. Gore, B. M. Blackburn, H. Luo, D. Ding, *Small* **2022**, *18*, 2201953.
[282] F. Zhu, F. He, D. Liu, H. Zhang, Y. Xu, K. Xu, Y. Chen, *Energy Storage Mater.* **2022**, *53*, 754.
[283] Z. Liu, D. Cheng, Y. Zhu, M. Liang, M. Yang, G. Yang, R. Ran, W. Wang, W. Zhou, Z. Shao, *Chem. Eng. J.* **2022**, *450*, 137787.
[284] J. Wang, Z. Li, H. Zang, Y. Sun, Y. Zhao, Z. Wang, Z. Zhu, Z. Wei, Q. Zheng, *Int. J. Hydrogen Energy* **2022**, *47*, 9395.
[285] Z. Liu, Y. Chen, G. Yang, M. Yang, R. Ji, Y. Song, R. Ran, W. Zhou, Z. Shao, *Appl. Catal., B* **2022**, *319*, 121929.
[286] H. Shi, C. Su, X. Xu, Y. Pan, G. Yang, R. Ran, Z. Shao, *Small* **2021**, *17*, 2101872.
[287] T. Matsui, N. Kunimoto, K. Manriki, K. Miyazaki, N. Kamiuchi, H. Muroyama, K. Eguchi, *J. Mater. Chem. A* **2021**, *9*, 15199.
[288] M. Saqib, I.-G. Choi, H. Bae, K. Park, J.-S. Shin, Y.-D. Kim, J.-I. Lee, M. Jo, Y.-C. Kim, K.-S. Lee, S.-J. Song, E. D. Wachsman, J.-Y. Park, *Energy Environ. Sci.* **2021**, *14*, 2472.
[289] W. Tang, H. Ding, W. Bian, W. Wu, W. Li, X. Liu, J. Y. Gomez, C. Y. Regalado Vera, M. Zhou, D. Ding, *J. Mater. Chem. A* **2020**, *8*, 14600.
[290] X. Lv, H. Chen, W. Zhou, S.-D. Li, Z. Shao, *J. Mater. Chem. A* **2020**, *8*, 11292.
[291] Y. Zhang, A. Zhu, Y. Guo, C. Wang, M. Ni, H. Yu, C. Zhang, Z. Shao, *Appl. Energy* **2019**, *238*, 344.
[292] Y. Lin, R. Ran, C. Zhang, R. Cai, Z. Shao, *J. Phys. Chem. A* **2010**, *114*, 3764.
[293] C. Fang, Y. Huang, K. Xu, Y. Xu, F. Zhu, Z. Du, H. Gao, Y. Chen, *J. Power Sources* **2024**, *614*, 234984.
[294] Z. Du, K. Xu, F. Zhu, Y. Xu, F. He, H. Gao, W. Gong, Y. Choi, Y. Chen, *Adv. Funct. Mater.* **2024**, *34*, 2409188.
[295] H. Shimada, Y. Yamaguchi, H. Sumi, Y. Mizutani, *Ceram. Int.* **2021**, *47*, 16358.

[296] N. Shi, K. Zhu, Y. Xie, D. Huan, J. Hyodo, Y. Yamazaki, *Small* **2024**, *20*, 2400501.
[297] F. Liu, H. Deng, D. Diercks, P. Kumar, M. H. A. Jabbar, C. Gumeci, Y. Furuya, N. Dale, T. Oku, M. Usuda, P. Kazempoor, L. Fang, D. Chen, B. Liu, C. Duan, *Nat. Energy* **2023**, *8*, 1145.
[298] M. Fu, W. Hu, H. Tong, X. Ling, L. Tan, F. Chen, Z. Tao, *J. Adv. Ceram.* **2024**, *13*, 63.
[299] J. Jing, Z. Lei, Y. Xue, Z. Zheng, H. Wang, P. Zhang, B. Ge, Z. Yang, *Energy Storage Mater.* **2024**, *72*, 103694.
[300] G. Zhang, T. Chen, Y. Yao, C. Wang, X. Bao, G. Zheng, Z. Huang, X. Zhang, K. Liu, L. Xu, Y. Zhou, S. Wang, *Appl. Catal., B* **2024**, *355*, 124176.
[301] Y. Xu, K. Xu, H. Zhang, F. Zhu, F. He, Y. Liu, Y. Chen, *Sci. Bull.* **2024**, *69*, 3682.
[302] P. Li, Q. Yang, Y. Niu, J. Du, F. Yan, X. Tong, L. Wang, T. Gan, *Ceram. Int.* **2024**, *50*, 40561.
[303] C. Yang, J. Li, C. Yang, Y. Li, A. Hu, J. Pu, B. Chi, *ACS Mater. Lett.* **2024**, *6*, 3540.
[304] J. Cao, Y. Ji, Z. Shao, *Energy Environ. Sci.* **2022**, *15*, 2200.

Xi Chen is a third-year Ph.D. candidate at The Hong Kong Polytechnic University in 2024, with Bachelor's and Master's degrees from Wuhan University. Since 2017, during his undergraduate studies, he has focused on solid oxide fuel cell technology. His research spans oxygen-ion and proton-conducting fuel and electrolysis cells, mixed ionic-electronic conducting materials, and semiconductors.

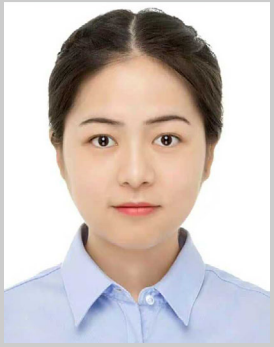

Na Yu obtained her Ph.D. degree from The Hong Kong Polytechnic University in 2025 under the supervision of Professor Meng NI. She earned both her Bachelor's and Master's degrees from Wuhan University. During her master's and Ph.D. studies, her research focused on oxygen-ion and proton-conducting fuel and electrolysis cells.

Meng Ni is the Associate Dean of the Faculty of Construction and Environment and Chair Professor of the Department of Building and Real Estate at The Hong Kong Polytechnic University. He received his Ph.D. from The University of Hong Kong in 2007. He is also a Humboldt Research Fellow and a Senior Research Fellow of the Hong Kong Research Grants Council (RGC). His research focuses on fuel cells, hydrogen energy, rechargeable metal-air batteries, and electrochemical systems for low-grade waste heat utilization.